UNIVERSITÀ DEGLI STUDI ROMA TRE
Dipartimento di Fisica "Edoardo Amaldi"
Dottorato di ricerca in fisica - XIX ciclo

Systematic study of the response and calibration of the Monitored Drift Tubes of the ATLAS Muon Spectrometer

Silvestro Di Luise

Coordinatore
prof. Orlando Ragnisco

Tutore
prof. Filippo Ceradini

Dicembre 2006

Contents

Paste decades of research in both theoretical and experimental high energy physics have lead to the so called Standard Model (SM) of particle physics which represents the today knowledge of nature's building blocks and forces on a sub-atomic scale. However there are still questions to be answered in the SM frame, such as the existence of the Higgs boson, a foundamental step in the explanation of the origin of the particle masses. Moreover experimental confirmations of the most appealing theoretical extensions of the SM, such as "Super Symmetry" need more performing experimental facilities to be investigated.

The next generation of hadron collider experiments at CERN has the potential to make precision tests of the model and to search for signatures of physics beyond the Standard Model in fact with the start of the Large Hadron Collider (LHC) operation, sheduled for the 2007, which will provide proton-proton collions at 14 TeV an unprecedented quantity of new physics phenomena will become experimentally accessible.

The ATLAS detector is conceived to be sensisitve to an as large as possible variety of final states signatures. High momentum muons are among the most promising and reliable signatures in the high energy collision events at the LHC. This led to the design of a high resolution muon spectrometer with stand-alone triggering and momentum measurement capability over a wide area of the kinematic phase space. Momentum determination is based on the magnetic deflection of muons trajectory in an air-core toroidal magnet field. The track reconstruction is performed in three measurement stations mainly made of high pressure drift tubes (MDT).

Discovery physics, as well as high-statistics precision measurements, will require extraction of clean signals with the ATLAS detector. This demands precise and stable in-situ calibration of the different subdetectors.

The purpose of the work presented here is the study of the performance of the drift tubes of the ATLAS muon spectrometer.

In particular, the analysis is focused on the development and optimization of the calibration tecnique, the study of the systematics involved and of the impact on the spatial resolution. That is the subject of the chapters four, five and six.

It follows (chapter seven) an analysis aimed the check for any evidence of degradation in the MDT preformance as a consequence of the extended exposure of the detector to the large particle flux during the accelerator operation.

The first two chapters are dedicated to the description of the research program, the main characteristics of the experimental apparatus and the physical motivatons which have driven both the accelerator and the detector design with emphasis in the ATLAS Muon Spectrometer. The third chapter reviews the principles of operation of the drift tubes motivating the choice of the operating parameters of the ATLAS MDTs and the problematics related to the signal extraction. An overview of the experimental setups, the software tools and the analysis tecniques used can be found in chapter four.

Chapter 1

Physics program at the LHC and the exprimental apparatus

1.1 Introduction

The Standard Model is the theory which better describes elementary particle interactions. Within the SM, particles are divided in spin 1/2 matter fields (leptons and quarks) and spin 1 gauge bosons which mediate particle interactions.

	Fermions			Bosons	
Leptons (l)	$\begin{pmatrix} \nu_e \\ e \end{pmatrix}$	$\begin{pmatrix} \nu_\mu \\ \mu \end{pmatrix}$	$\begin{pmatrix} \nu_\tau \\ \tau \end{pmatrix}$	$\begin{pmatrix} \gamma \\ Z, W^\pm \end{pmatrix}$	$SU_T(2) \times U_Y(1)$
Quarks (q)	$\begin{pmatrix} u \\ d \end{pmatrix}$	$\begin{pmatrix} c \\ s \end{pmatrix}$	$\begin{pmatrix} t \\ b \end{pmatrix}$	$\begin{pmatrix} g_{cc'} \end{pmatrix}$	$SU_C(3)$

The Standard Model is a renormalizable gauge theory based on the symmetry

$$SU_T(2) \otimes U_Y(1) \otimes SU_C(3)$$

where T is the weak isospin, Y is the hypercharge and C is the color. The unified theory of electromagnetic and weak interactions relies on the symmetry $SU_T(2) \otimes U_Y(1)$ and processes are described in terms of γ, Z^0 and $W^\pm$ bosons exchange. Quantum Chromodynamics (QCD) is a non abelian gauge theory based on a $SU_C(3)$ color symmetry which describes hadronic interactions. The gauge bosons of the color field are 8 *colored* gluons.

To reproduce observations on weak decays and to allow CP violation within the Standard Model, the quarks which participate in weak interaction have to be mixed introducing a mixing matrix (Cabibbo, Kobayashi, Maskawa CKM) [1][2] defined by

$$\begin{pmatrix} d' \\ s' \\ b' \end{pmatrix} = V_{CKM} \begin{pmatrix} d \\ s \\ b \end{pmatrix} = \begin{pmatrix} V_{ud} & V_{us} & V_{ub} \\ V_{cd} & V_{cs} & V_{cb} \\ V_{td} & V_{ts} & V_{tb} \end{pmatrix} \begin{pmatrix} d \\ s \\ b \end{pmatrix} \tag{1.1}$$

and described in terms of 3 parameters and one complex phase for a total of four free parameters.

In the Standard Model particles are massless because mass terms in the lagrangian are not invariant; to generate the observed particle mass spectra, the breaking of the electroweak symmetry is required. This can be done by the Higgs mechanism [3] which makes use of one isodoublet field: three Goldstone bosons among the four degrees of freedom are absorbed to build up the longitudinal components of the massive $W^{\pm}$ and Z bosons; the last degree of freedom corresponds to a physical scalar particle, the Higgs boson. The present knowledge on the Higgs particle mass is shown in figure 1.1 [4]. Although there is yet no direct evidence of the Higgs boson, a global Standard Model fit to the electroweak data yields information about the Higgs boson mass m_H: m_H=88^{+60}_{-37} GeV corresponding to a 95% CL upper limit of m_H<206 GeV. The 95% CL lower limit of 114 GeV from the direct searches at LEP2 [5] is also shown. Despite of its numerous successes in explaining the present data, the standard model will not be tested completely before the Higgs boson has been experimentally observed and studied. This particle has to be searched in a mass range from the present experimental limit up to the limit of 1 TeV imposed by the stability of the theory.

The experimental behaviour of the coupling constants suggests a possible unification (*Grand Unification Theory*, with all forces described by a single coupling constant) at an energy scale Λ_{GUT} of the order 10^{14}-10^{16} GeV. Trying to extend the Standard Model up to Λ_{GUT} presents two major problems. The first is the so called *naturalness*

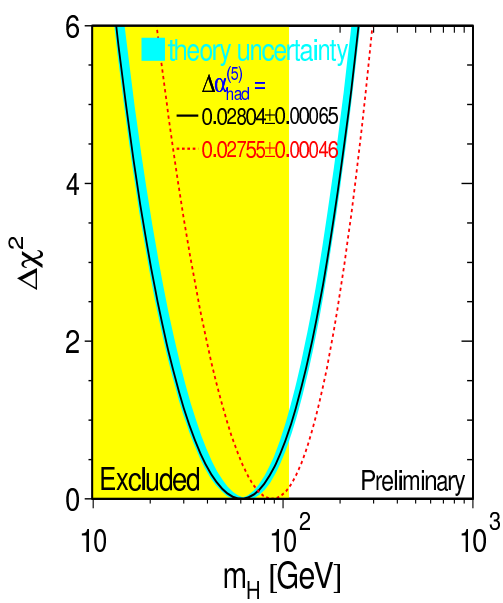

Figure 1.1: The χ^2 of the fit to electroweak data as a function of the Higgs mass [4].

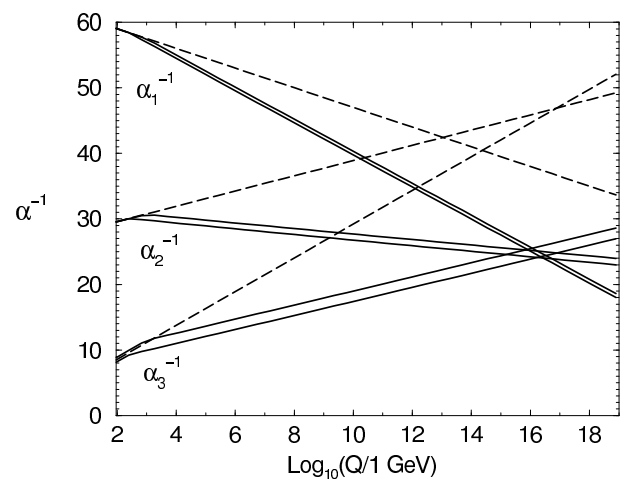

Figure 1.2: Evolutions of the inverse gauge coupling $\alpha_i^{-1}(Q^2)$ in the Standard Model (dashed lines) and in the MSSM (solid line) [6].

problem: the Higgs mass diverges quadratically with Λ (cancellations at all orders would be required). The second is that GUT predictions for the coupling constants are incompatible with the Standard Model. To overcome these problems, different theories have been proposed as an extension of the Standard Model. The most promising is $SuperSymmetry$ which is based on the assumption that a particle, boson or fermion, has a partner (*sparticle*) with inverted statistics. In this assumption two problems are solved at once: supersymmetric particle loops cancel exactely the quadratic divergences and contribute to the running of the gauge coupling constants correcting the discrepancies with GUT theories (figure 1.2). The Minimial Supersymmetric extension of the Standard Model ($MSSM$) [6] is based on the same symmetry as the SM and contains the minimum number of particles. $MSSM$ requires two isodoublets of Higgs fields to cancel anomalies and to give mass to fermions and introduces 5 bosons (par.h 1.4).

1.2 Physics program at the LHC

The Large Hadron Collider (LHC) [12] is a proton proton collider under construction at CERN in the existing LEP tunnel. It has been designed for a center of mass energy

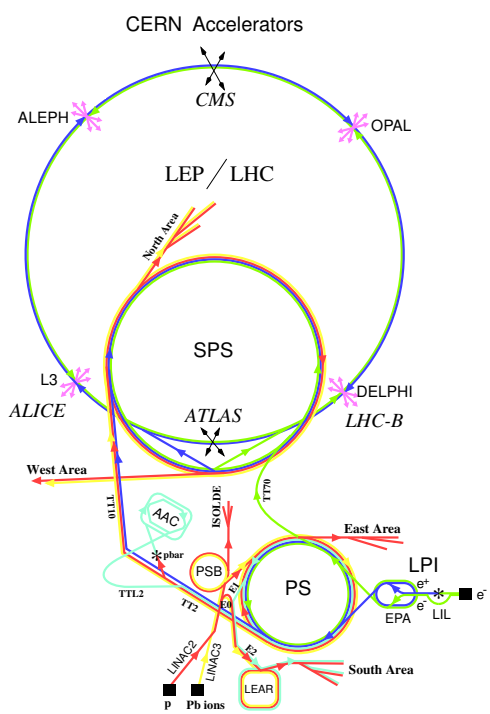

LEP: Large Electron Positron collider
SPS: Super Proton Synchrotron
AAC: Antiproton Accumulator Complex
ISOLDE: Isotope Separator OnLine DEvice
PSB: Proton Synchrotron Booster
PS: Proton Synchrotron
LPI: Lep Pre-Injector
EPA: Electron Positron Accumulator
LIL: Lep Injector Linac
LINAC: LINear ACcelerator
LEAR: Low Energy Antiproton Ring

LHC nominal parameters	
Beam energy	7 TeV
Magnetic field of the dipoles	8.33 T
Bunch spacing	24.95 ns
Number of bunches	2808
Radius of the bunch at the interaction point	16μm
Bunch length	7.7 cm
Number of particle in a bunch	$1.1 \cdot 10^{11}$
Luminosity	10^{34} cm^{-2}s^{-1}
Crossing angle	300 μrad
Circulating current	0.56 A
Energy lost per round	7 keV
Total radiated power for a beam	3.8 kW

Table 1.1: LHC nominal parameters

of 14 TeV and for a luminosity of $10^{34}\text{cm}^{-2}\text{s}^{-1}$. The two proton beams will circulate in two different beam lines contained in the same cryogenic and mechanical structure. To accelerate the protons to the injection energy of 450 GeV, the Super Proto Synchrotron (SPS) and its pre-accelerators are used (figure 1.2). The 1232 magnets foreseen along the beam line are 14.6 m long and will have a magnetic field of 8.33 T. The beams will collide with an angle of 300 μrad to avoid multiple collisions between the bunches near the interaction vertex. As the bunches will be 7.7 cm long and will have a radius of 16 μm at the crossing point, the spread of the position of the interaction vertex is expected to be 5.6 cm (r.m.s) along the beam line.

The Large Hadron Collider will offers a large range of physics opportunities.

The most important issue is the quest for the origin of the spontaneous symmetry breaking mechanism in the electroweak sector of the Standard Model (SM). A possible manifestation of the spontaneous symmetry breaking mechanism is the existence of a Higgs boson or of a family of Higgs particles in the case of the minimal supersymmetric extension of the Standard Model.

The search of supersymmetric particles as of any other signal of new physics (for example, new heavy gauge bosons up to 5-6 TeV) is another relevant part of the physics program.

Already at initial lower luminosity the LHC will be a high rate b and t quark factory. The cross section for $b\bar{b}$ pairs production is expected to be 0.5 mb, about 1% of the total cross section. This means about $5{\cdot}10^{12}$ events per year at a luminosity of $10^{33}\text{cm}^{-2}\text{s}^{-1}$. A wide program of B-physics studies can thus be performed including a precise measurement of CP violation and the determination of the parameters of the CKM matrix. The 10^7 $t\bar{t}$ pairs delivered per year with a luminosity of $10^{33}\text{cm}^{-2}\text{s}^{-1}$ will allow a precise top quark mass measurement in different channels and the search for rare decays.

Proton-(anti)proton cross sections for several processes are shown in figure 1.3 as a function of the center of mass energy [7]. At the LHC energy, non diffractive *p-p* inelastic cross section is assumed to be 70 mb. This means an average of 20 collisions for bunch crossing at the design luminosity.

The largest fraction of these collisions are non interesting inelastic collisions (the so called *minimum bias* events) characterized by a small average transverse momentum of the produced particles ($< p_T >= 500$ MeV). On the other hand, processes of interest have a smaller cross section; for example the cross section for Higgs production is about 10 pb. This gives a hint on the importance for the experiments that will operate at the LHC of an adequate detector granularity to avoid *pile-up* and of a very high background rejection capability of the trigger system.

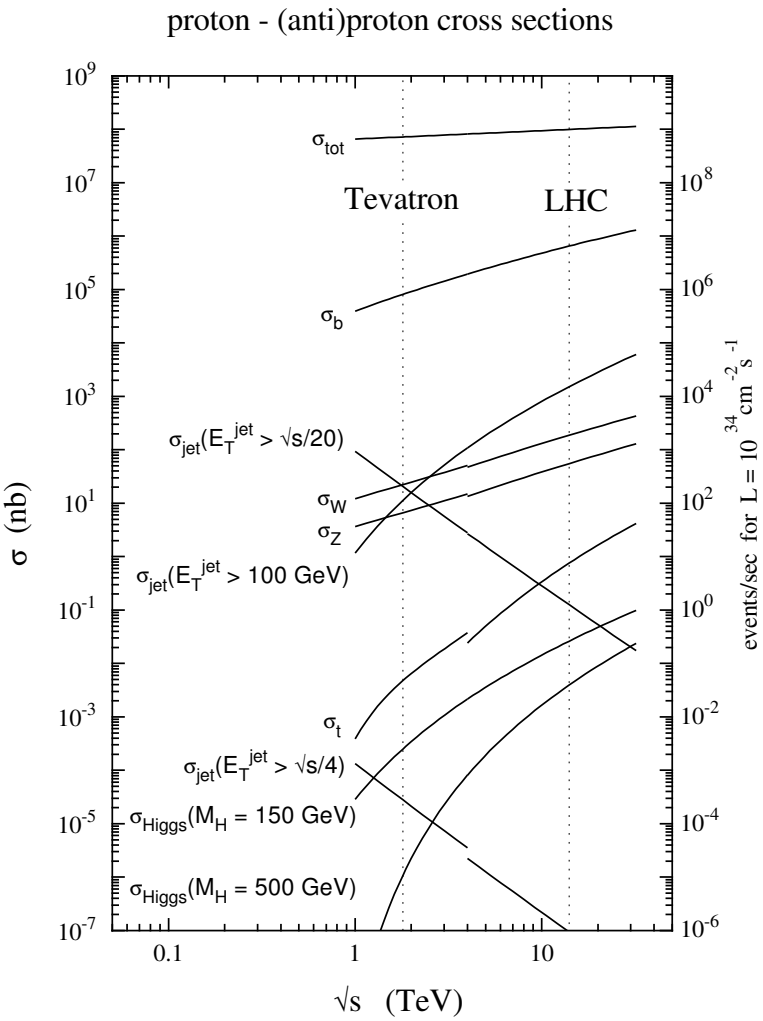

Figure 1.3: Proton-(anti)proton cross sections for several processes as a function of the center of mass energy [7].

1.3 Higgs boson search

In figure 1.4 the expected cross-sections for each individual process for SM Higgs boson production at the LHC are shown as a function of the Higgs mass M_H [8]. The Higgs boson is produced mainly via gluon-gluon fusion with a cross section larger than 10 pb for M_H up to 400 GeV. The second dominant production process for M_H>100 GeV is the vector boson fusion (VBF). The associated production of SM Higgs with other heavy particles (W, Z, $t\bar{t}$ pairs) is relevant for M_H<200 GeV.

The Higgs branching ratios and total width are shown in figure 1.5 and 1.6 as a function of the Higgs mass [9]. The decays useful for Higgs detection in different M_H ranges are those with large branching ratio and detection efficiency and low background contamination. The mass range goes from the lower limit of 114 GeV set by LEP2 [5] and the upper limit of 1 TeV required for the stability of the theory.

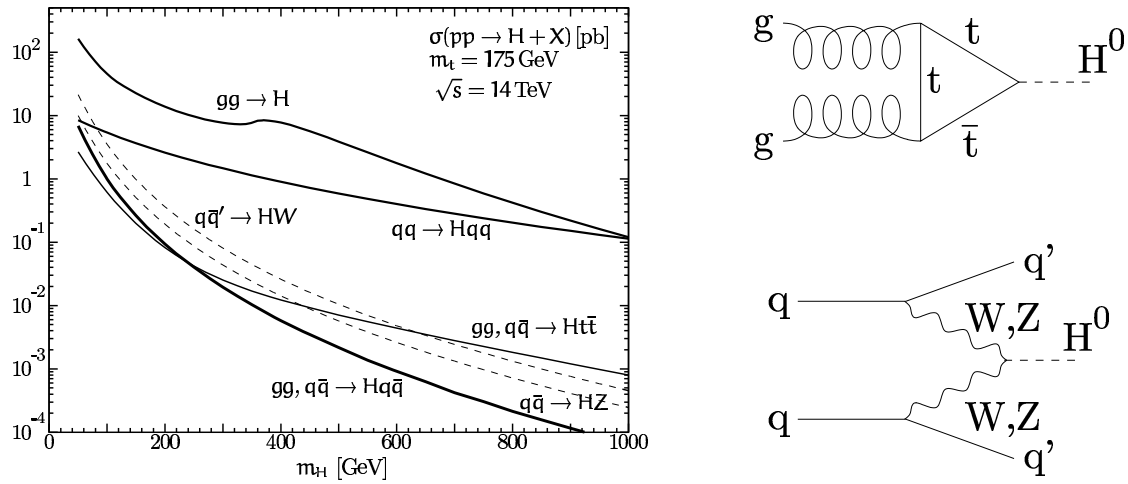

Figure 1.4: Higgs boson production cross-section at the LHC for the various process as a function of the Higgs mass M_H. The diagram of the two dominating processes (gluon-gluon fusion and vector boson fusion) are shown on the right.

The strategy adopted for the Higgs searches depends on M_H [17]:

- Low mass region (M_H<130 GeV). $H \to b\bar{b}$ has a branching ratio close to 1 but the signal to background ratio due to QCD background is smaller than 10^{-5}. This decay mode may be used in the associated production of the Higgs with a W, a Z or a $t\bar{t}$ pair; in these cases the high p_T leptons from gauge bosons or top decay can be used to select the events.

  The $H \to \gamma\gamma$ channel has a small branching ratio (about 10^{-3}) but the expected signal to background ratio of 10^{-2} makes this channel interesting.

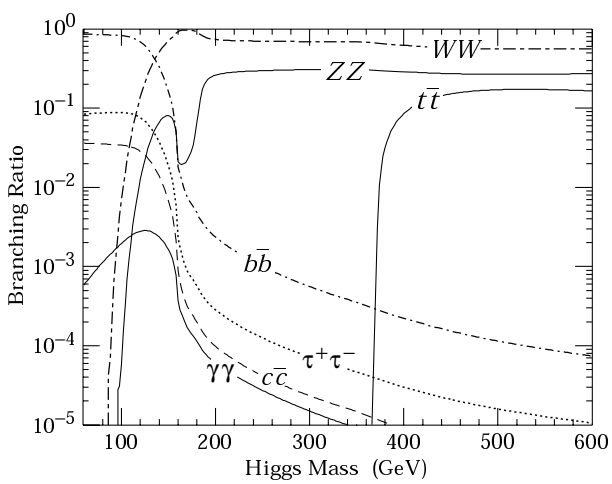

Figure 1.5: Higgs branching ratios as a function of M_H.

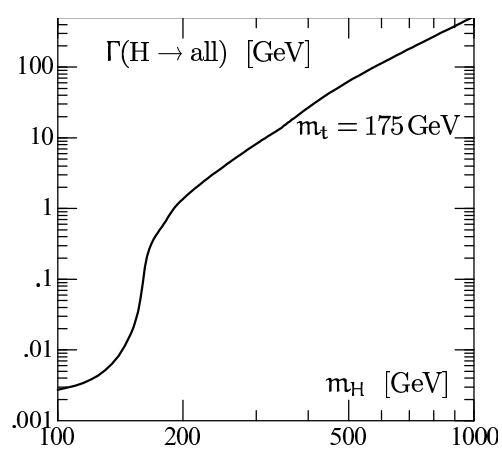

Figure 1.6: Total Higgs width Γ_H as a function of M_H.

- Intermediate mass region (130 GeV$<M_H<2M_Z$). The most powerful channels are $H\rightarrow ZZ^{(*)}\rightarrow 4l$ and $H\rightarrow WW^{(*)}\rightarrow l\nu l\nu$. The leptons are required to reduce the background.

- High mass region ($M_H>2M_Z$). The discovery should be easy in the channel $H\rightarrow ZZ\rightarrow 4l$. The sources of background for this process are mainly two:
  $t\bar{t}\rightarrow Wb+W\bar{b}\rightarrow l\nu+l\nu\bar{c}+l\nu+l\nu c$ and $Zb\bar{b}\rightarrow lll\nu cl\nu\bar{c}$
  but the signal can be detected requiring an high invariant mass for two lepton pairs.

  For very large masses ($M_H>500$ GeV) the production cross section decreases and the channels $H\rightarrow ZZ\rightarrow ll\nu\nu$ and $H\rightarrow WW\rightarrow l\nu 2jets$ have to be used to increase the statistics.

The statistical significance (defined as $N_S/\sqrt{N_B}$, where N_S and N_B are the number of signal and background events) is shown in figure 1.7 as a function of the Higgs mass for the different decay modes.

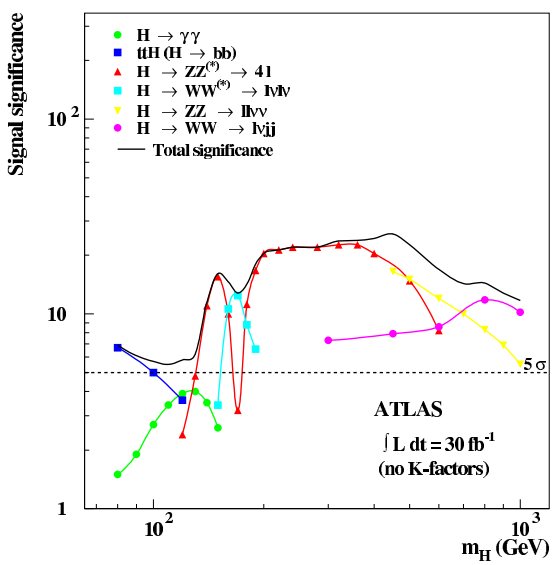

Figure 1.7: Statistical significance for the discovery of a SM Higgs boson in different channels [17].

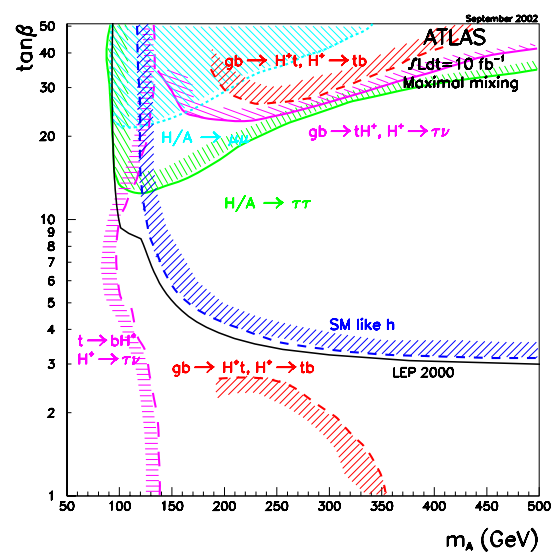

Figure 1.8: 5σ contours in the $M_A/tan\beta$ plane for the MSSM Higgs [11].

1.4 Supersymmetric particles and Higgs boson in the MSSM

If supersymmetric particles exist, they will be produced and detected at the LHC in a mass range up to 2 TeV. They will in turn decay to the lightest supersymmetric

particle (LSP) which is stable and hardly interacting with matter. The search for supersymmetric particles thus sets stringent limits on missing energy measurement.

The simplest supersymmetric extension of the Standard Model requires two doublets with vacuum expectation value v_1 and v_2 to implement the mechanism of spontaneous symmetry breaking.

The physical particle spectrum contains two neutral scalar bosons (h and H), two charged Higgs bosons ($H^{\pm}$) and one pseudoscalar (A). The mass of the lightest boson (h) depends on the ratio v_2/v_1=$tan\beta$, on the top mass and on the masses of the other supersymmetric particles. At large $tan\beta$ and with m_{top}=174 GeV, m_h<130 GeV and this limit reduces for lower $tan\beta$. If a single Higgs particle will be found with a mass larger than 130 GeV, supersymmetric theories will be ruled out.

The plane of the two free parameters M_A and $tan\beta$, in the range 0<M_A<500 GeV and 0<$tan\beta$<50, can be explored with some specific decay channels like $A/H \rightarrow \tau\tau$ and with SM Higgs like channels as $h/H \rightarrow \gamma\gamma$ (figure 1.8). The most promising results to be the channel $A/H \rightarrow \tau\tau$. It is required a very good τ identification capability and a good resolution in missing energy measurement. The selection of these events is based on the detection of the lepton coming from a τ; the other τ can decay into hadrons (higher branching ratio) or into leptons. To reduce the background from $pp \rightarrow b\bar{b}X$ followed by $b \rightarrow jet$ and $\bar{b} \rightarrow \mu$, an isolated high p_T lepton, a jet with E_T^j>40 GeV and missing energy (E_T^{miss}>20 GeV) are required.

1.5 ATLAS: an outlook of the experiment

The ATLAS (A Toroidal LHC ApparatuS) [13] collaboration proposed a general purpose experiment designed to exploit the full discovery potential of the LHC outlined in the previous sections. The main goals that have driven the design of the detector are:

- A calorimeter system that can identify and measure electrons and photons, measure energy and direction of particles and jets and that is hermetic for missing energy measurements.

- An inner tracking system for lepton momentum measurement, for b-quark tagging and for enhanced electron-photon identification.

- A muon system for muon identification and momentum measurement for very high energy muons.

- A selective trigger to confront the high background environment.

- A large geometrical acceptance.

- Radiation resistance to allow operation for more than ten years of data taking.

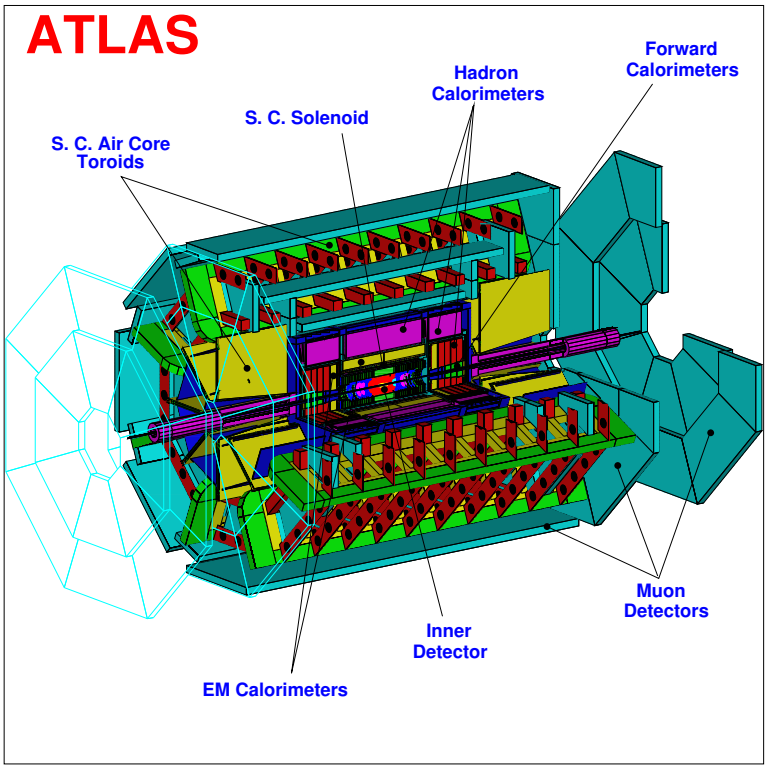

Figure 1.9: Three-dimensional view of the ATLAS detector. The subdetectors and the magnet system are shown.

In figure 1.9 a three-dimensional view of the ATLAS detector is shown. Starting from the beam line, the detector is made of an inner tracker contained in a superconducting solenoid that generates a field of 2 Tesla, of an electromagnetic and hadronic calorimeter and of the muon spectrometer that consists in layers of muon chambers in a toroidal air-core magnet. A global reference system is defined with the beam line as z axis and the y axis pointing in the up direction. In the x-y plane, the R coordinate is the distance from the beam line and ϕ is the azimuthal angle ($0<\phi<2\pi$). The polar angle θ in the R-z plane is in the range $0<\theta<\pi$; the pseudorapidity η is defined as $\eta=-\ln(\tan(\theta/2))$.

In the following can be found a brief decsription of the Inner Detector and of thge Calorimeter system.

The Muon Spectrometer will be the subject of the next chapter.

Inner detector

The inner detector [14] has been designed to match the following requirements:

- Tracking capability up to $|\eta|<2.5$.
- Transverse momentum resolution $\frac{\Delta p_T}{p_T}<30\%$ at $p_T=500$ GeV and $|\eta|<2$

- High efficiency (95%) for isolated tracks with p_T>5 GeV

An overview of the inner detector is given in figure 1.10. Its outer radius is R=115 cm and it is about 7 m long. It is divided in three zones; in the central ($|z|$<80 cm, *barrel*) detectors are placed in rings centered on the beam line while in the forward regions (*end caps*) they are arranged in wheel orthogonal to the beam line.

- Semiconductor Tracker (SCT). It is made of silicon detector segmented in pixels (2 layers in the barrel region and 8 wheels in the end caps) or in strips (4 layers in the barrel). Single point resolution is 13 μm.

- Transition Radiation Tracker (TRT). It is made of drift straw tubes filled with a Xenon gas mixture with a single point resolution of 170 μm; polypropylene radiators are provided to generate transition radiation which gives additional electron identification ability.

Each track with $|\eta|$<2.5 is reconstructed with 6 precise points in the SCT and at least 36 points in the TRT.

Calorimeters

The ATLAS calorimeter [15][16] has been designed to meet the different demands of the LHC physics program while operating in a very high luminosity environment. This system must be capable of reconstructing the energy of electrons, photons and jets as well as measuring missing transverse energy.

The calorimeter is shown in figure 1.11. A barrel cryostat around the inner detector cavity contains the barrel electromagnetic calorimeter and the solenoidal coil which supplies a uniform field in the inner tracking volume. This coil is placed in front of the electromagnetic calorimeter. Two end cap cryostats enclose the electromagnetic and hadronic end cap calorimeters as well as the integrated forward calorimeter. The

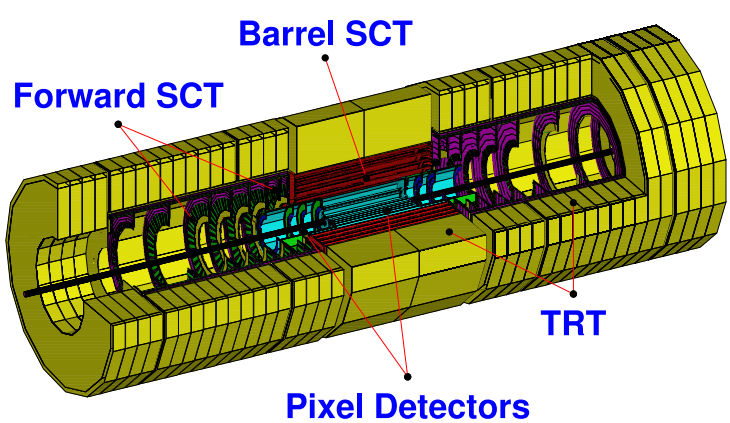

Figure 1.10: Layout of the inner detector

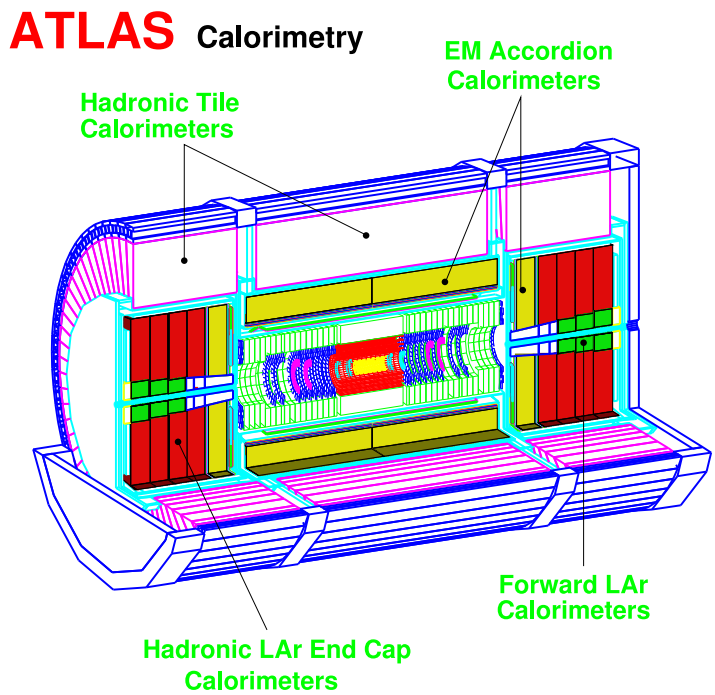

Figure 1.11: Three dimensional view of the calorimeter system

barrel and extended barrel hadronic calorimeters are contained in an outer support cylinder, acting also as main solenoid flux return. The outer radius of the calorimeters is 4.23 m. The electromagnetic calorimeter uses lead absorbers in liquid Argon; it is implemented in an *'accordion'* geometry. Angular resolution is expected to be 40 μrad/$\sqrt{E(GeV)}$ while energy resolution will be $\frac{\sigma_E}{E}$=10%/$\sqrt{E(GeV)}$ $\oplus$1%. The hadronic calorimeter in the barrel region uses iron absorbers with scintillator plates staggered in planes perpendicular to the beam axis. At larger rapidities, where higher radiation resistance is required, the adronic calorimeter is based on the use of liquid Argon. The expected combined energy resolution is $\frac{\sigma_E}{E}$=50%/$\sqrt{E(GeV)}$ $\oplus$3% in the barrel and $\frac{\sigma_E}{E}$=100%/$\sqrt{E(GeV)}$ $\oplus$10% in the end caps.

At η=0, the total thickness of the calorimeters is about 11 interaction lengths.

Chapter 2

The ATLAS Muon Spectrometer

An overview of the requirements that have driven the design of the ATLAS muon spectrometer [18] is presented in the first part of the chapter. It follows a description of the apparatus and of the trigger system.

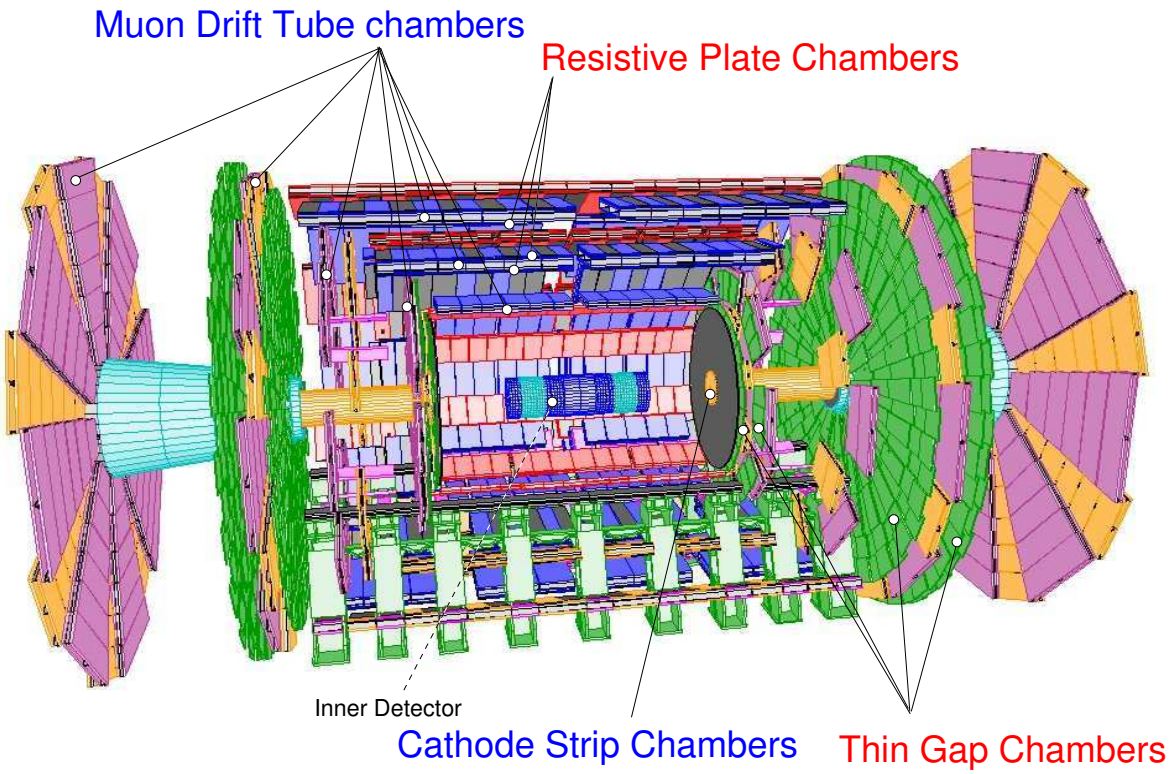

Figure 2.1: The muon spectrometer of the ATLAS detector. Muon Drift Tubes (MDT) and Cathode Strip Chambers (CSC) are *precision chambers* while Resistive Plate Chamber (RPC) and Thin Gap Chambers (TGC) are *trigger chambers* (see text for details).

The muon spectrometer (fig. 2.1) covers the largest fraction of the ATLAS volume with its dimensions of 22 m in external diameter and 44 m in length.

Charged particles trajectories are deflected by the means of a toroidal magnetic field of 0.6 T on average. The particle position is measured at different points. Knowing the field map, the muon momentum can be derived from the *sagitta* of the track fitted to the points. Two different kind of detectors are present: the *precision chambers*, to measure the coordinate in the bending plane and the *trigger chambers* used as trigger device and to measure the coordinate along the magnetic field line (the "second coordinate").

2.1 Physics Motivations

The desired performance of the spectrometer are defined by the main physical processes present in the ATLAS research program [17]. For example:

1. The Standard Model decay

   $$H \to ZZ^* \to \mu\mu ll$$

   is dominant for Higgs masses from 120 GeV/c^2 to 180 GeV/c^2. In this range the natural mass width is of about 1 GeV/c^2. Considering also the high background associated to this process it was found that the mass resolution should be of the order of 1% to achieve a significant signal sensitivity.

   This implies a transverse momentum[1] resolution $dp_t/p_t \leq 2\%$, according to the latest estimations.

   In this channel muons are produced with momenta between 5 GeV/c and 50 GeV/c.

   Similar requirements are valid for the MSSM decay

   $$H^0, A \to \mu^+\mu^-$$

   which is dominant in the mass range from 100 GeV/c^2 and 200 GeV/c^2 and for $\tan\beta > 20$.

   Moreover, a high detection efficiency in a large psudorapidity range is particularly important, in fact, due to the muons momentum, a good hermiticity in the forward region is required.

2. Possible extensions of the Standard Model can be pursued searching for $Z' \to \mu^+\mu^-$ and all muonic decays of heavy supersymmetric particles. In this kind of processes, the decaying particle can have a mass as high as 5 TeV/c^2 and produce muons with momentum in the TeV/c range. A resolution dp_t/p_t of

[1] The momentum component orthogonal to the magnetic field line.

about 10% is considered a good value for an unambiguous determination of the muon (curvature) sign.

3. For beauty particle studies good performance are needed in the reconstruction of muons from the B decay chain whose typical momentum is lower than 30 GeV/c.

2.2 Performance requirements and technical motivations

The main requirements that have to be met to maximize the overall detector performance and their impact on the spectrometer design are outlined here.

- The transverse momentum p_t of a charged particle moving in a uniform magnetic field $\vec{B}$ is related to the *sagitta* S of the trajectory, defined in the figure 2.2, by

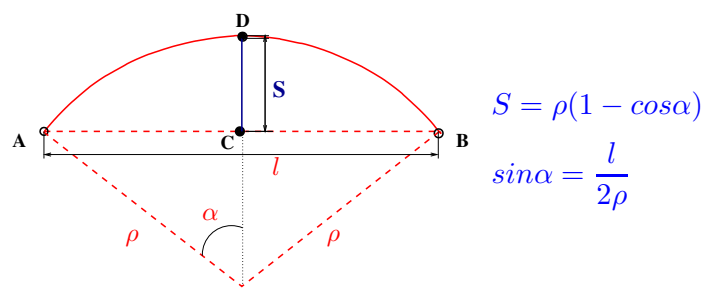

Figure 2.2: The sagitta S of the circular trajectory with curvature radius ρ through the points A,D and B is the shortest distance $\overline{CD}$ from the real trajectory and the undeflected path $\overline{AB}$.

the equation

$$S = \frac{0.3Bl^2}{8p_t} \tag{2.1}$$

where the length l is measured in meter, B in Tesla and p_t is the momentum perpendicular to $\vec{B}$ measured in GeV/c([2]). The error on the sagitta, σ_S, can be assumed proportional to the single point resolution[3]. Therefore from the 2.2:

$$\frac{dp_t}{p_t} = \frac{\sigma_S}{S} \propto \frac{\sigma(r)}{S} = \sigma(r)\,\frac{p_t}{0.3Bl^2}. \tag{2.3}$$

[2]From fig. 2.2: $\alpha \sim l/2\rho$ for $l << \rho$. Since the curvature radius $\rho = \frac{p_t}{0.3B}$ follows

$$S = \rho(1 - cos\alpha) \simeq \rho(1 - (1 - (\frac{1}{2}\alpha^2)\,) = \frac{\rho\alpha^2}{2} \simeq \frac{0.3Bl^2}{8p_t}. \tag{2.2}$$

[3]Assuming the positions r_A, r_D and r_C of the points in fig. 2.2 have been measured with (the same) resolution $\sigma(r)$, the sagitta can be calculated as $S = r_D - \frac{1}{2}(r_A + r_B)$ and the associated resolution $\sigma_S^2 = \sigma(r)^2 + 2 \cdot \frac{1}{4}\sigma(r)^2 = \frac{3}{2}\sigma(r)^2$.

Hence the momentum resolution degrades linearly with increasing p_t but improves for high B field and larger radial size (lever arm) of the tracking volume.

The measurement points used for the track reconstruction (on the bending plane), the "super points", are usually chosen as the center of the muon chamber traversed by the particle (fig. 2.8). The super points coordinates are thus determined using the information available from the single drift tubes (par. 2.4.1).

The point resolution $\sigma(r)$ in the 2.3 sums up the contributes due to the intrinsic tube resolution the multiple scattering and the alignment precision.

The apparatus must allow for a resolution dp_t/p_t of few percent in the low momentum region (see e.g. point 1 of the previous section) where the resolution is dominated by energy loss (up to 20 GeV/c) and multiple scattering. This was a decisive argument for choosing an air core magnet system with the lowest possible amount of matter.

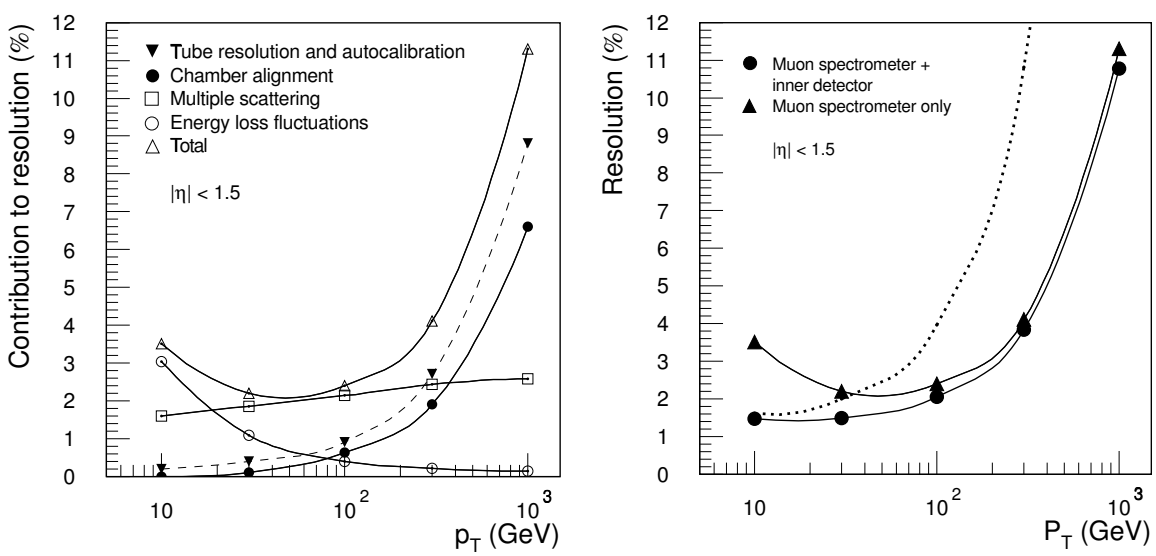

Figure 2.3: *Left.* Contribution to the standalone transverse muon momentum resolution assuming a single tube resolution of 80 μm. Above 300 GeV/c the dominant contribution comes from the single tube resolution, followed by the chamber alignment. *Right.* Muon momentum resolution combining the measurements of both the spectrometer and the inner detector. The dotted line corresponds to the inner detector standalone tracking. For momenta above 100 GeV/c the muon spectrometer standalone performance almost equals the combined one.

As demonstrated in fig. 2.3 a resolution between 2% and 3.5% is achievable in the

momentum range from 10 GeV/c to 2000 GeV/c. Using also the measurement points provided by the inner detector the 2% value is possible from 3 GeV/c to 100 GeV/c.

Since the inner detector (standalone) resolution is better for momenta lower than 20 - 30 GeV/c, in the B-physics studies (see for example point 3 of the previous section) the muon chambers are used mainly at trigger level (described further). The implication for the muon system is that pattern recognition should work even for the softest muons reaching the spectrometer which have a momentum of about 3 GeV/c.

The goal of a resolution $dp_t/p_t \approx 10\%$ for $p_t = 1\,TeV/c$, as reported in the point 2 of the previous section, can be achieved only through the combination of the bending power and of the precision of the detector in the sagitta measurement (eq. 2.3). Therefore such requirement strongly influenced the definition of the main detector characteristics.

The term Bl^2 in 2.3 suggests that a large tracking cavity and an intense magnetic field are needed. To generate a magnetic field of few Telsa over the large spectrometer volume a current of the order of 10 kA must be provided. Such currents can be cosidered only in the context of superconductiong magnets. The number of lines crossed by a muon track in toroids is constant and the bending power increases at higher pseudorapidities (see 2.3) hence a toroidal magnetic field has the property that the transverse momentum resolution is constant over a wide range of pseudorapidity. A drawback of this configuration is that the bending does not take place in the plane transverse to the beam axis therefore the precise knolwdge of the primary interaction point (20 μm wide at LHC) cannot be exploited.

With $B = 0.6\ T$ and $l = 4.5\ m$, from 2.2 results a sagitta of 500 μm for a momentum of 1 TeV/c. This means the sagitta must be determined with a precision $\sigma_S = S \cdot dp_t/p_t$ of about 50 μm (eq. 2.3) . For high momentum muons muliple scattering is negligible and the resolution is dominated by the intrinsic tube resolution and the alignment precision as shown in fig. 2.3. It can be demonstrated that a tube resolution of about 80 μm is necessary. As a consequence the accuracy of the relative positioning of the chambers and the mechanical precision of the chamber assembly has to match the spatial resolution of the drift tubes. This ask for a dedicated alignment system and specific chamber construction demands. A description of the spectrometer is given in the next section.

- A reconstruction of the track in the non-bending plane projection ("second coordinate" plane) with a point resolution of about 10 mm is required for a safe track reconstruction and reliable momentum determination.

- In general all the physics measurements benefit from a high rapidity coverage and good hermiticity. An example is given in point 2 of the previous section; high hermiticity is also imnportant to avoid fake missing energy detection which may suggests the presence of neutrinos or stable super-symmetric particle.

  The ATLAS spectromer covers the range $|\eta| < 2.7$. Two chamber technologies are used: the Monitored Drfit Tubes in the central rapidity region while for $|\eta| > 2$ Cathode Strip Chamber with higher granularity and rate capability are used since they have to operate in a higher background rate and particle density.

- Trigger selectivity: transverse momentum thresholds of 10 - 20 GeV/c are adequate for high-mass states, which will be in the focus of LHC physics at nominal luminosity. Lower thresholds of $p_t \sim 5\ GeV/c$ are required for CP violation and beauty physics.

- Trigger coverage: adequate trigger efficiencies can be obtained with a pseudorapidity coverage smaller than that of the precision chambers. The actual requirements are mostly determined by processes at the opposite ends of the LHC mass scale: the need for good acceptance for rare high mass Higgs particles, and the need for very high statistics to study small rate asymmetries due to CP violation in the B sector. A trigger coverage corresponding to $|\eta| < 2.4$ is found to be sufficient.

- Bunch-crossing identification: the LHC bunch-crossing interval of 25 ns sets the scale for the required time resolution of the first-level trigger system (par 2.4, 2.5).

- The ATLAS experiment is forseen to meet the whole physics program after at least 10 years of operation. The necessity to operate for many years in a high background and particle flux without performance degradation implies severe constraints on the detector condition of operation. Therefore a gas which does not suffer from aging effect is mandatory. Moreover a fine segmentation helps to reduce occupancy to a good track reconstruction capability. The background operation condition are described in the next chapter.

2.3 The magnetic system

The ATLAS magnetic system consists of a central solenoid and three toroid magnets. The central solenoid produces a field of 2 T in the Inner Detector region.

Each of the three toroids, one in the barrel and two in the endcap region, is made out of 8 coils assembled radially around the beam axis (fig. 2.4). The barrel toroid extends over a lenght of 25 m with an inner diameter of 9.4 m and outer dimeter of 20 m. The two endcap toroids, inserted at the two ends of the barrel, have a length

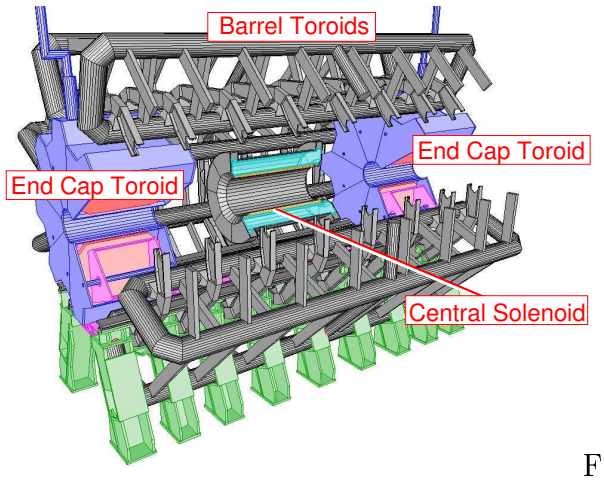

Figure 2.4: The ATLAS magnetic system.

of 5 m; inner and outer diameter are respectively 1.6 m and 10.7 m. The barrel coils are contained in individual cryostats while in the endcaps they are assembled in a single large cryostat. The results is a field configuration (fig. 2.5) where the field lines surround the detector azimuthally. The average value is 0.6 T. The bending power $\int \vec{B} \cdot \vec{dl}$ at $\phi = 0$ varies from 2 Tm for $|\eta| = 0$ to 9 Tm for $|\eta| = 2.7$ (fig. 2.5).

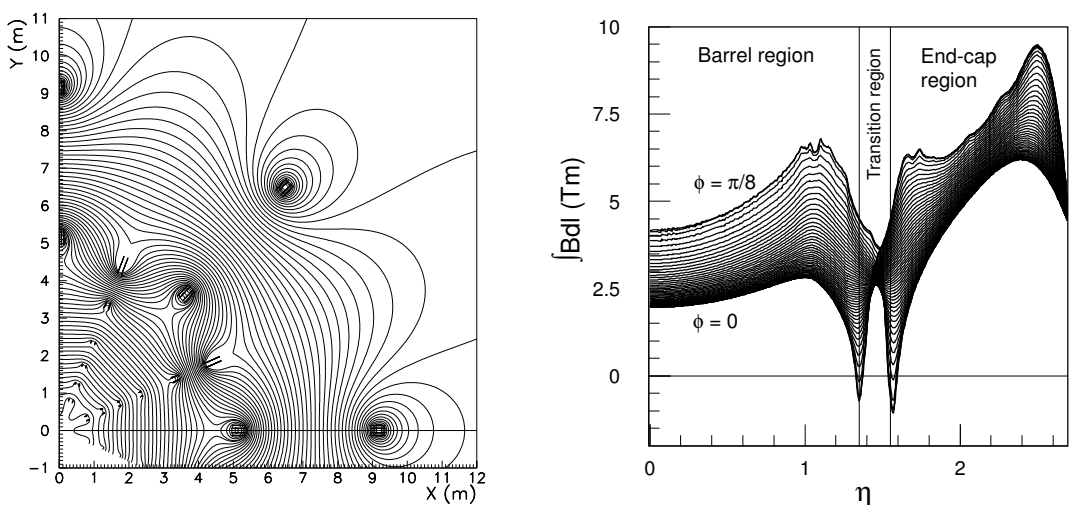

(a) Magnetic field map for a fixed η in the transition region. The field lines are shown in a plane perpendicular to the beam axis. The interval separating consecutive lines is 0.1 Tm. The scales are in m

(b) Toroid bending power $\int \vec{B}\vec{dl}$ of the azimuthal field component integrated between the first and the last muon chamber as a function of pseudorapidity for different values of ϕ.

Figure 2.5: Characteristics of the toroidal magnetic field.

2.4 Apparatus description

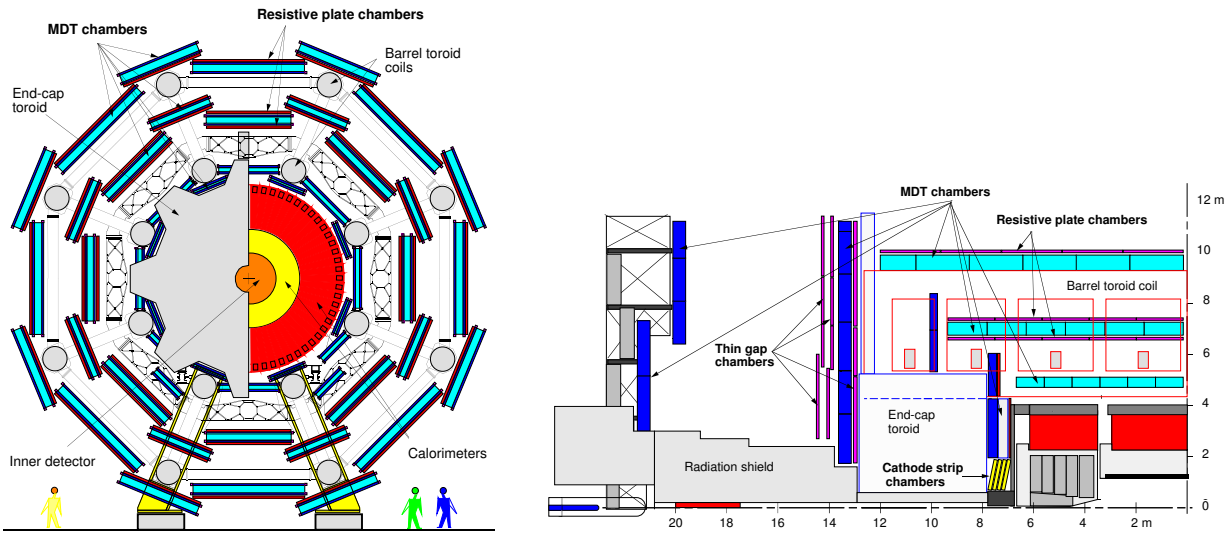

Figure 2.6: *Left*. Transverse view of the ATLAS Muon Spectrometer. *Right*. Side view of one quadrant of the spectromter.

The ATLAS Muon Spectrometer is made up of three main modules: the barrel region and two endcap regions (fig. 2.1, 2.6).

In the barrel ($|\eta| < 1$) chambers are arranged in three cylinders, usually referred as stations, concentric with the beam axis. The inner station (BI:Barrel Inner) is located at distance of about 5 m while the middle (BM) and the outer stations (BO) are positioned at radii of about 7.5 m and 10 m respectively (fig. 2.1, 2.6). Usually a chamber is labelled with a three letter code according to the its position, fig. 2.7. If the chamber spans the region between two toroid coils, it's of type L (Large), then it can be labelled as BIL, BML or BOL. Instead if it is in the line with a toroid coil it's a type S (Small) chamber: BIS, BMS or BOS[4].

In this η-region the inner and the outer stations are outside the toroid coils hence the particles position are measured near the inner and outer field boundaries, and inside the field volume. An example is shown in fig. 2.8.

The end-cap chambers cover the pseudo-rapidity range $1 < |\eta| < 2.7$ and are arranged in four disks at distances of 7 m, 10 m, 14 m and $21 - 23$ m from the interaction point (fig. 2.1, 2.6). In this η-region the chambers are arranged to determine the momentum with the best possible resolution from a point-angle measurement.

[4]Other labels are used to identify "special" chambers: for example in the bottom part of the spectrometer some chambers, the BOFs, have an irregular shape to leave room to the spectrometer supports.

The whole spectrometer consists of two type of chambers and four different technologies:

- **Precision Chambers**. For the precision measurement of muon tracks in the principal bending direction of the magnetic field, Monitored Drift Tube (MDT) chambers are used except in the innermost ring of the end-cap inner-station ($2 < |\eta| < 2.7$).

  In the innermost ring of the end-cap inner-station (fig. 2.6) Cathode Strip Chambers (CSC) are employed to cope with the higher particles flux. The CSC are

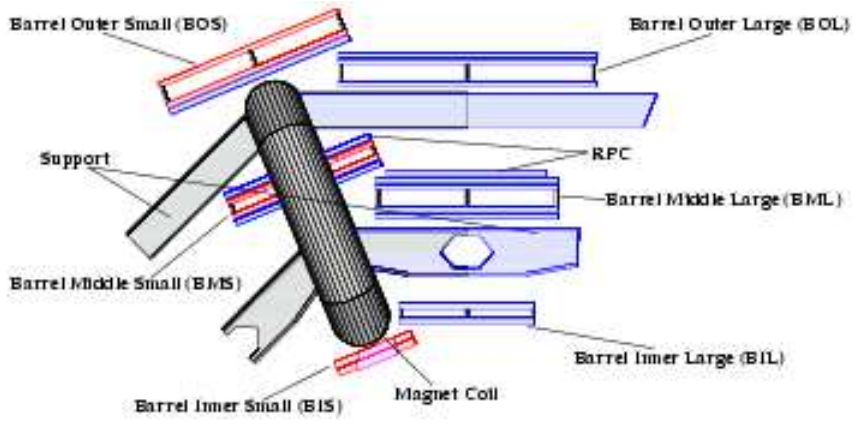

Figure 2.7: Definition of the chambers identifcation label in the barrel sector.

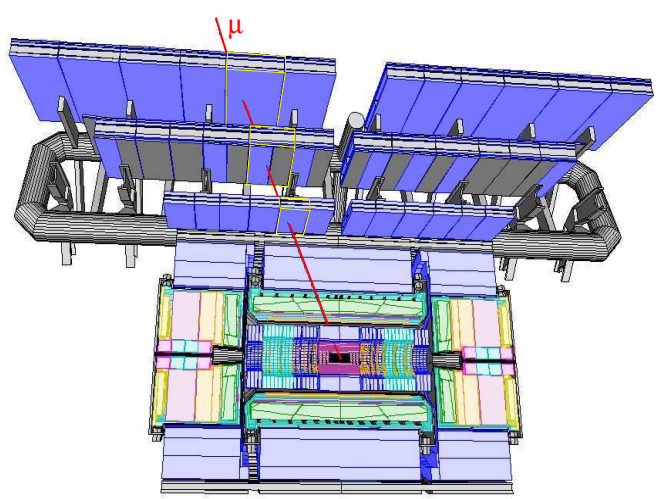

Figure 2.8: Event display of a muon travesing the inner detector, the calorimeters and three barrel stations.

multi-wire proportional chambers with cathode strip readout and with a symmetric cell in which the anode-cathode spacing is equal to the anode-wire pitch. A spatial resolution of 60 μm has been measured. A transverse coordinate is obtained from the strips parallel to the anode wires, which form the second cathode of the chamber.

- **Trigger Chambers**. These chambers provide the trigger function, the bunch-crossing identification (par. 2.5) and the measurement of the "second coordinate".

  In the barrel this information is provided by three stations of Resistive Plate Chambers (RPC). They are located on both sides of the middle MDT station, and either directly above or directly below the outer MDT station (fig 2.6, 2.7, 2.12). An RPC consists of a pair of parallel bakelite plates of high resistivity with a well defined distance; the gap between the two plates is filled with a gas mixture on the basis of tetrafluoroethane ($C_2H_2F_4$). A voltage of about 10 kV is applied across the gap; this causes primary ionization electrons produced by a traversing particle to multiply while drifting towards the anode. Signals are read out via capacitive coupling by a set of metal strips on the outside of the bakelite plates. Typical spatial and time resolutions are 1 ns and 10 mm respectively. These values are adequate for identification of the muon hits with the associated bunch crossing and rough muon transverse measuremnts at trigger level (par. 2.5)

  Each chamber is made of two rectangular detector layers, each one read out by two orthogonal series of pick-up strips: the η - strips are parallel to the MDT wires and provide the measurements of the trigger detector in the bending plane; and the ϕ - strips, orthogonal to the MDT wires, provide the second coordinate measurement which is important for the off-line pattern recognition.

  In the end-caps, three stations of Thin Gap Chambers (TGC), located near the middle MDT station will be installed. The TGC have a structure similar to multi-wire proportional chambers, with the difference that the anode-wire pitch (1.8 mm) is larger than the cathode-anode distance (1.4 mm). The electric field configuration and the short drift distance provide for a good time resolution and a fast response. Signals from the anode wires, arranged parallel to the MDT wires, provide the trigger information together with readout strips arranged orthogonal to the wires, that also provide a measurement of the second coordinate.

2.4.1 The MDT chambers

A schematic drawing of an MDT chamber is shown in fig. 2.9.

A MDT chamber consists of three or four layers (a *multilayer*) of cylindrical aluminium drift tubes on each side of a supporting frame. The tubes diameter is of about

3 cm.

The four-layer chambers are located in the innermost muon detector stations where the background hit rates are the highest. An additional drift-tube layer makes the pattern recognition in this region more reliable.

The drift tubes, named MDT (Monitored Drift Tubes), are the basic unit of the chamber, they are filled with a noble gas based mixture and have a thin wire running along the cylinder axis which serves as anode when high voltage is applied beetwen the wire and the tube wall. Such a detector can be used for precise position measurements as described in detail in the next chapter.

The barrel chambers are of rectangular shape with areas of 1.5 m^2 to 12 m^2 and length between 1 m and 6 m([5]). Instead, the disk like shape of the end cap stations implies a trapezoidal chamber geometry. The tapering angles are 8.5^o for the smaller and 14° for the larger chambers. The endcap chamber areas range from 1 m^2 to 10 m^2.

There are in total 380000 MDTs in ATLAS assembled into 1194 chambers.

[5]On one end of the chamber, the tubes are connected to the high voltage and on the other end to the readout electronics. The denoinations readout (RO) and high voltage (HV) is also used to distinguish between the chamber ends (fig. 2.9). The supporting frame is a light-weight aluminium structure holding the drift tube layers. It consists of three crossplates (RO, MI and HV , fig. 2.9) oriented perpendicular to the tube axis, i.e. in z-direction in the chamber coordinate system. The crossplates are connected by two longbeams oriented parallel to the tube axis, i.e. in x-direction. The multilayers are glued to the crossplates.

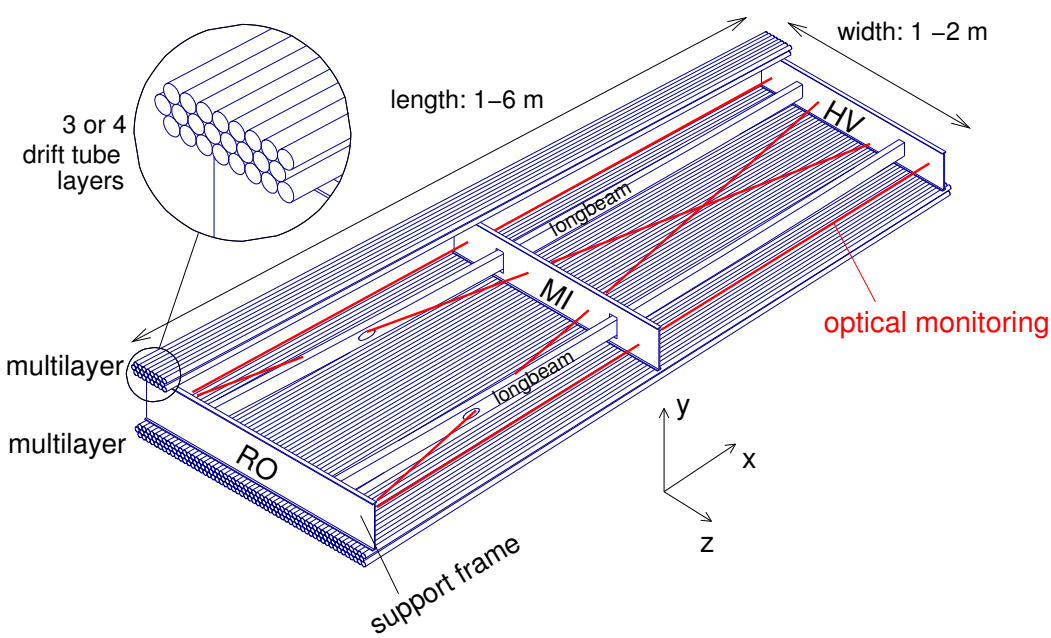

Figure 2.9: Scheme of the MDT chambers layout.

In order to achieve the desired resolution (see previous section) wires are positioned inside each tube and the MDTs are glued togheter following a special assembly procedure. The wire-tube eccentricity is below 10 μm. Considering also the relative assembly accuracy of MDTs within a chamber the anode wires are positioned inside a chamber with 20 μm accuracy.

Internal alignment

Chamber deformation due to temperature changes and gravitational forces are measured continuously during the operation of ATLAS by means of light rays (fig.2.9). A LED at one end of the chamber is used together with a lens mounted on the middle cross plate to project an encoded chess-board pattern mask onto a CCD camera at the other chamber end. Changes in the chamber geometry will result in a movement or rotation of the image; by analysing the CCD data this can be corrected for during the track reconstruction process. The system described is known as 'in-plane alignment'. The continuous recording of the chamber shape, is a core feature of the ATLAS muon spectrometer, this explains the adjective "Monitored" used to identify the ATLAS drift tubes.

The local chamber alignment (in-plane alignment) precision in lower then 10 μm.

2.4.2 The global alignment system

Displacements of the chambers position up to several millimeters are expected to be found with respect to the nominal designed position, moreover, relative chamber movements (of the same size) can be expected when the toroid magnet is switched on or because of temperature variations.

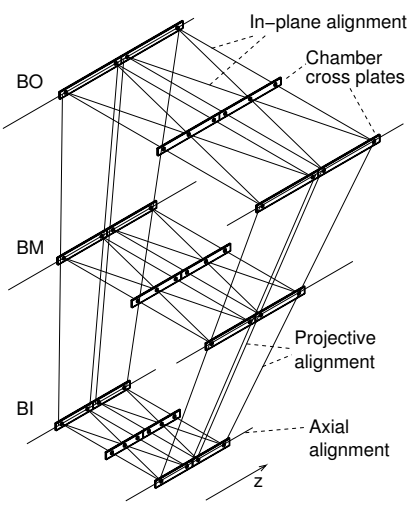

Figure 2.10: Muon chamber alignment for the barrel region. All chambers are arranged such that the lines connecting their corners point towards the interaction point ('projective towers'). A set of optical alignment rays is used to monitor chamber movements. Axial lines run parallel to the beam axis while projective lines connect different stations. Adjacent chambers are additionally connected by so-called proximity sensors (not shown).

Equally important to the measurement of the individual chamber shapes (discussed

in the previous section) is therefore the monitoring of the total muon spectrometer geometry.

This so-called 'global alignment system' is, as the in-plane, based on optical sensors connected by light rays. The barrel chambers are arranged such that they form projective towers, as shown in fig. 2.10: the hypothetical lines connecting the corners of an inner, middle and outer station chamber point towards the interaction point. Adjacent chambers are optically linked by proximity sensors; axial lines are parallel to the beam axis and connect chambers within a station. A set of projective alignment rays finally provides a connection of the three stations themselves[6].

The global alignment system allows for a relative positioning accuracy of MDTs within a chamber lower then 30 μm.

2.5 The Trigger Strategy

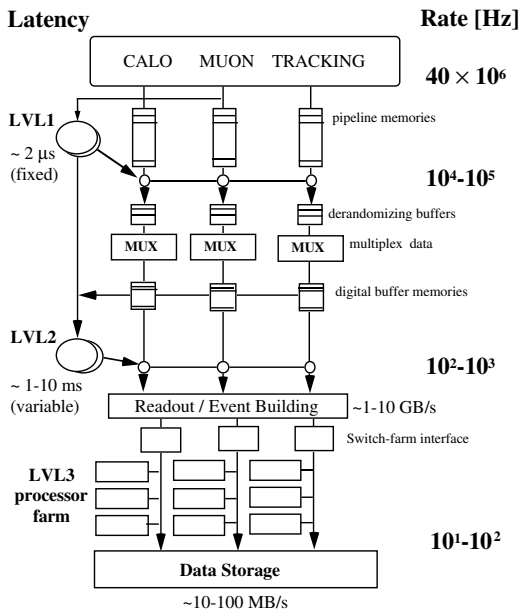

Figure 2.11: The ATLAS three level trigger architecture.

The rate with which events accour at the LHC is given by the bunch crossing frequency of 40 MHz (one every 25 ns), multiplied by the number of proton-proton collisions per bunch crossing (25 on average). For a luminosity of 10^{34} $cm^{-2}s^{-1}$, the event rate is 10^9 Hz.

[6]In the endcap region the situation is slightly more difficult since the vacuum vessels of the endcap toroids block the line of sight between some of the stations. In addition to the elements described above for the barrel, a system of rigid reference bars is therefore used. These are cylindrical metal tubes which are themselves equipped with an optical system to monitor their deformation. Sensors mounted on the alignment bars are then utilized to interconnect the individual chambers and stations.

The data-acquisition will be able to store events with a rate of 100 Hz (corresponding to about 50 MB/s).

The task of the trigger is to reduce the interaction rate from 10^9 Hz to 100 Hz selecting efficiently only the events of interest for the physics objectives (the Higgs production rate, for example, is 0.1 $\frac{events}{s}$).

The bunch-crossing period of 25 ns is much shorter than the maximum response of the MDT[7] and thus association of the event with the correct bunch crossing identification is essential to reconstruct correctly muon tracks and to correlate data from different subdetectors.

In the trigger architecture of the ATLAS experiment, data from different sectors of different subdetectors are processed in parallel to speed up the procedure. Three trigger levels of increasing accuracy and complexity are used to select the events; informations from the previous levels are used to reduce the amount of data to be processed (fig. 2.11).
The Level-1 trigger uses data with reduced-granularity from the trigger chambers. The Level-2 trigger uses full-granularity and full-precision data from the trigger and the precision chambers but examines only regions of the detector area flagged by the Level-1 trigger as "regions of interest" (RoI) . The Level-3 trigger uses the full event data for the final selection of events for offline analysis.

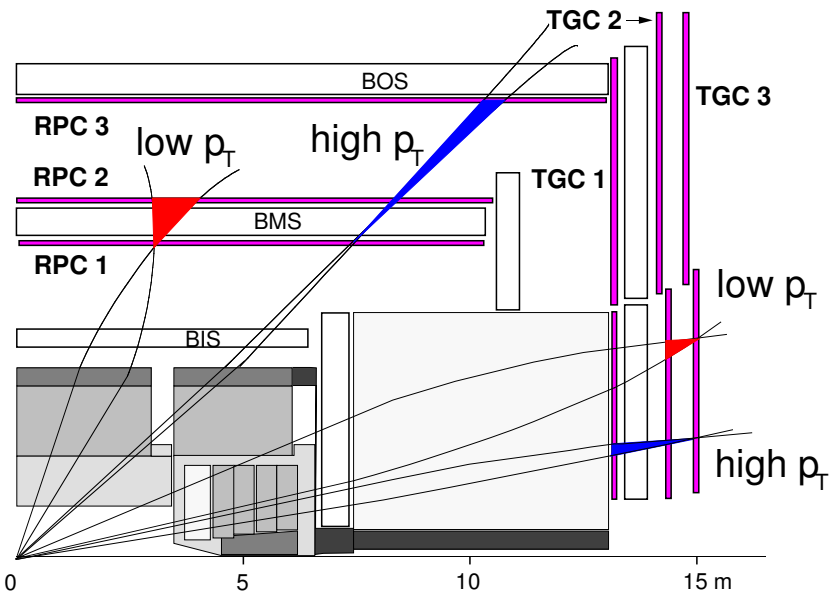

Figure 2.12: Scheme of the first level muon trigger.

- **Level-1** First level trigger accepts data at the rate of 40 MHz with a latency of 2 μs. Criteria of selection are the multiplicity of muons, electromagnetic clusters

[7]Dominated by the maximum drift time which is about 700 ns (Chap. 3).

and jets as well as global information like missing transverse enrergy. After this trigger selection the event rate is reduced to 75 kHz.

For the case of the Level-1 muon trigger two scenarios are forseen (2.12). When the LHC will operate at high luminosity (10^{34} $cm^{-2}s^{-1}$) the amount of data can only be coped with if a sufficiently high muon momentum thershold is chosen: the so colled high-p_t trigger accepts muons with $p_t > 20GeV/c$. For low luminosity runs (10^{33} $cm^{-2}s^{-1}$) momenta down to 6 GeV/c are accepted. This is the low-p_t trigger.

In the barrel region the low-p_t trigger request is satisfied if, in the stations RPC1 and RPC2, (fig. 2.12) a combination of hits (in both coordinates) can be found which fulfills the condition that the hits in RPC2 lie within a tolerance window from the straight line defined by the hit in RPC1 and the interaction region. No hits in RPC3 are required since low energy particles are likely to be deflected before reaching the outer station. For the endcap low-p_t trigger analogous hit combination is required in TGC3 and TGC2 stations.

For the high-p_t trigger an additional hit, within a coincidence window, is required in the station RPC3 (barrel) or TGC1 (encap).

- **Level-2**

  The second level is designed to reduce the Level-1 trigger rate to a about 1 kHz. To achieve the required rate reduction of a factor 100, the Level-2 trigger must process data from the trigger detectors and combine them with data from the tracking chambers. Level-2 processing is restricted to the Regions of interest in the η-ϕ space defined by level-1 informations.

  In the muon spectrometer, the p_t resolution of the first level can be improved using data from the precision chambers to measure momentum with a fast algorithm.

- **Level-3** Performs a global analysis combining information from different subdetectors. Events which meet the final criteria are stored.

section

Chapter 3

Monitored Drift Tubes

3.1 Description

The basic components of an Atlas drift tube [18] are shown in figure 3.1.

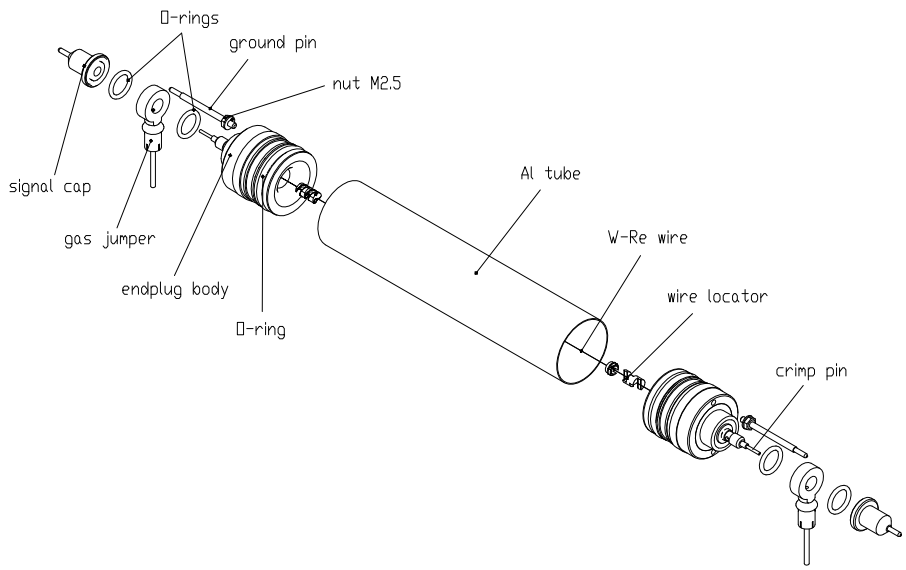

Figure 3.1: Schematic view of an ATLAS Monitored Drift Tube.

Each MDT consists of a thin wall (0.4 mm) aluminium tube with 29.97 mm outer diameter, a gold plated tungsten-rhenium wire with a diameter of 50 μm running along the tube axis and two endplugs which close the MDT at both ends. Each endplug consists of a body of modified polyphenylenether re-enforced with glass fibres, an accurately machined outer aluminium ring and a high precision central brass insert. The endplugs, besides making the gas sealing, provide also electrical insulation between the high voltage anode wire and the outer tube wall; they further fixe the position of the wire with respect to the aluminium tube and allow the connection of the MDT to

the gas distribution and front-end electronics. The precisely machined outer surface of the endplug is used during assembly of the individual MDTs to control the relative position of the wire with respect to the tube axis to the required 10 μm accuracy. The main parameters are listed in table 3.1.

Parameter	Nominal value
Outer tube radius	14.985 mm
Wall thickness	400 μm
Tube material	Al
Tube length	from 180 to 520 cm
Anode wire radius	25 μm
Anode wire material	W-Re alloy (93:7)
	gold plated 3% by weight
Anode wire resistance	40 Ω/m
Anode wire tension	350 g
Tube-wire eccentricity	10 μm (r.m.s.)

Table 3.1: Basics MDT construction parameters.

3.2 Principles of operation

Drift tubes are gas-filled ionization detectors which operate in proportional mode. The anode wire is supplied with a high voltage, typically in the kV range, while the metallic tube wall is grounded. Electron and ion pairs created by a ionizing particle traversing the gas drift towards the anode and the cathode respectively in the radially symmetric electric field

$$E(r) = \frac{V}{ln\frac{b}{a}} \cdot \frac{1}{r}, \tag{3.1}$$

where V is the anode wire potential, b the tube inner radius and a the wire radius. Close to the wire the electric field is high enough for the drifting electrons to gain sufficient kinetic energy to cause secondary ionization; the total number of electron-ion pairs increases by a factor G known as gas gain or gas amplification. For the Atlas MDTs an Ar:CO_2 $(93:7)$ gas mixture is adopted, the nominal potential is $3080\,V$ and the operating absolute pressure is 3 bar; the gas gain is $2{\cdot}10^4$.

In the section are described the physical processes involved in the signal generation in a drift tube [19, 20, 21, 22, 23, 24].

3.2.1 Ionization

Muons The average energy loss by a charged particle, heavier than electron, traversing

a thickness dx of material is given by the Bethe-Bloch fomula

$$-dE/(\rho dx) = Kz^2 \cdot \frac{Z}{A} \cdot \frac{1}{\beta^2} \cdot \left(\frac{1}{2} ln \frac{2m_e c^2 \beta^2 \gamma^2 T_{max}}{I^2} - \beta^2 \right), \tag{3.2}$$

where K is a constant equal to 0.31 $MeV g^{-1} cm^{-2}$, ρ is the density, Z the atomic number, A the mass number of the absorbing material. I is equal to ZI_0 if I_0 is the mean ionization potential per electron of the absorbing material ; β and γ are the relativistic parameters of the particle of charge ze. T_{max} is the maximum kinetic energy which can be transferred in a single collision to a free electron.

Neglecting the dependence of T_{max} on the particle mass, the energy loss depends only on the particle velocity: it decreases as $1/\beta^2$ reaching the minimum value at $\beta \sim 0.96$, and increases slowly for $\beta \to 1$ ([1]). For energies greater than few hundred MeV all the particles are at the minimum of ionization (said to be *mip*s or minimum ionizing particles) and loose the same amount of energy per unit length. For most material the minimum $dE/\rho dx$ is approximatively equal to 2 $MeV/(gcm^2)$.

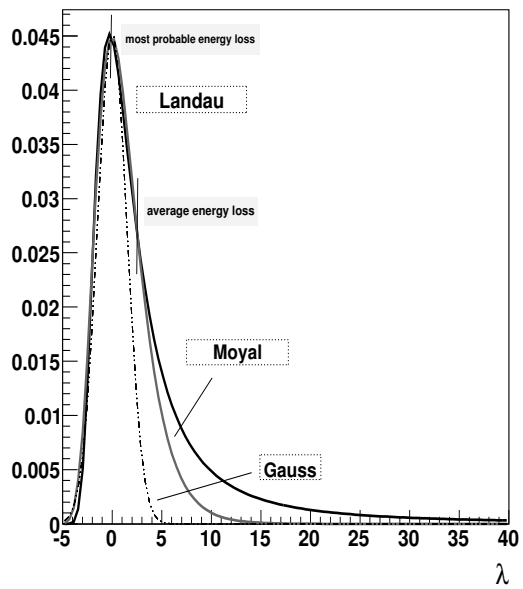

Figure 3.2: Landau and Moyal distributions. A gaussian fit to the maximum is also drawn.

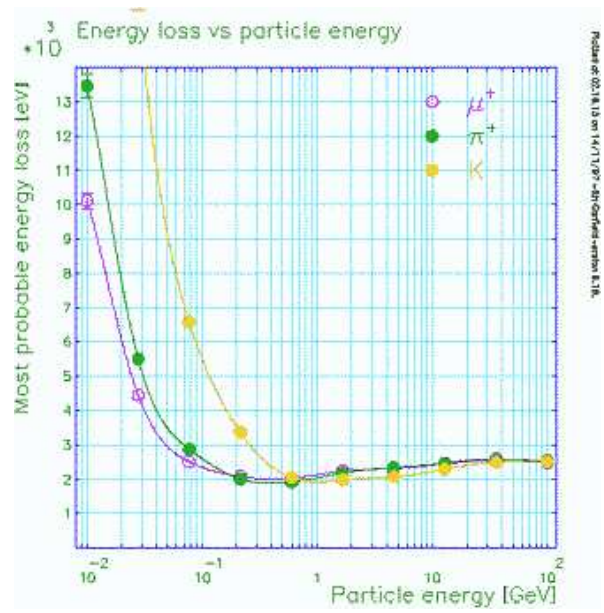

Figure 3.3: Simulation of the most probable energy loss in 1 cm of Argon for different particles.

In case of thin absorbers, like gases, the total energy deposition is given by a small amount of interactions hence fluctuations around the average can be significant. The

[1]The increase in the energy loss for momenta higher than 10 GeV/c or so (relativistic rise), due to the logarithmic term in the Bethe-Bloch formula, is saturated because of "polarization effects" (not taken into account by the 3.2). In gases saturation occurs around few hundred GeV/c at a value which is about 1.5 times minimum ionization.

energy loss distribution in thin media follows a Landau distribution [19] which is well approximated by the Moyal analytic formula [20, 21]

$$f(\lambda) = \frac{1}{\sqrt{2\pi}} e^{-\frac{1}{2}(\lambda + e^{-\lambda})}, \ \lambda = \frac{E - E_p}{\xi}. \tag{3.3}$$

The function depends on the single parameter E_p: the most likely energy loss. The parameter λ represents the normalized energy deviation from E_p being $\xi = Kz^2 \cdot Z/A \cdot \rho/\beta^2 \cdot x$ the first term of the Bethe-Bloch formula (3.2). As shown in fig. 3.2, Moyal approximation underestimates the Landau tail at high energy losses. In figure 3.3 is reported the most probable energy loss distribution in Argon at normal condition (NTP ([2])) for different particles with energy ranging from 10 MeV to 100 GeV produced with the GARFIELD [37] (par. 4.4) simulation program.

Charged particles, in a gaseous absorber, loss their energy mainly trough excitation and ionization of the atoms of the material itself. In the former case an electron can be released whether the excited atom returns to the ground state emitting an Auger electron or a photon which ionizes the gas via photoelectric effect. The total average number n_{tot} of ion pairs produced per unit length can be espressed as the ratio

$$n_{tot} = \Delta E / W_i \tag{3.4}$$

Gas	Z	δ (g/cm^3)	I_0 (eV)	W_i (eV)	$dE/d(\rho x)$ (MeV/gcm^2)	dE/dx (keV/cm)	n_p (cm^{-1})	n_{tot} (cm^{-1})
H_2	2	$8.38 \cdot 10^{-5}$	15.4	37	4.03	0.34	5.2	9.2
He	2	$1.66 \cdot 10^{-4}$	24.6	41	1.94	0.32	5.9	7.8
N_2	14	$1.17 \cdot 10^{-3}$	15.5	35	1.68	1.96	(10)	56
O_2	16	$1.33 \cdot 10^{-3}$	12.2	31	1.69	2.26	22	73
Ne	10	$8.39 \cdot 10^{-4}$	21.6	36	1.68	1.41	12	39
Ar	18	$1.66 \cdot 10^{-3}$	15.8	26	1.47	2.44	29.4	94
Kr	36	$3.49 \cdot 10^{-3}$	14.0	24	1.32	4.60	(22)	192
Xe	54	$5.49 \cdot 10^{-3}$	21.1	22	1.23	6.76	44	307
CO_2	22	$1.86 \cdot 10^{-3}$	13.7	33	1.62	3.01	(34)	91
CH_4	10	$6.70 \cdot 10^{-4}$	13.1	28	2.21	1.48	16	53
C_4H_{10}	34	$2.42 \cdot 10^{-3}$	10.8	23	1.86	4.50	(46)	195

Table 3.2: Properties of some gases used in drift detectors. See text for parameters description. Values are given at NTP.

of the total average energy loss per length ΔE and the effective energy W_i needed to produce a single pair([3]). This value sums up both primary ion pairs, produced in

[2]Normal Tempearature and Pressure conditions: 293.15 K, 1 atm $\equiv$ 1.013 bar $\equiv$ 760 $Torr$.

[3]This value is greater than the ionization potential of the gas since, during the ionization process, part of the energy can be dissipated by excitation of the inner shells of the gas atom.

the collisions of the particle itself, and secondary ion pairs, produced by those primary electrons ejected with energy sufficient to provoce further gas ionizations. Electrons have energies of the order of few keV, that means their range in the gas volume is limited to few microns; hence ionization electrons can be treated as grouped in clusters localized around the primary ionization points along the particle trajectory.

In table 3.2 are listed some useful experimental values. Measurements reported in fig. 3.4(a) suggest that the average number of primary ion pairs (n_p) is roughly proportional to the atomic number of the medium.

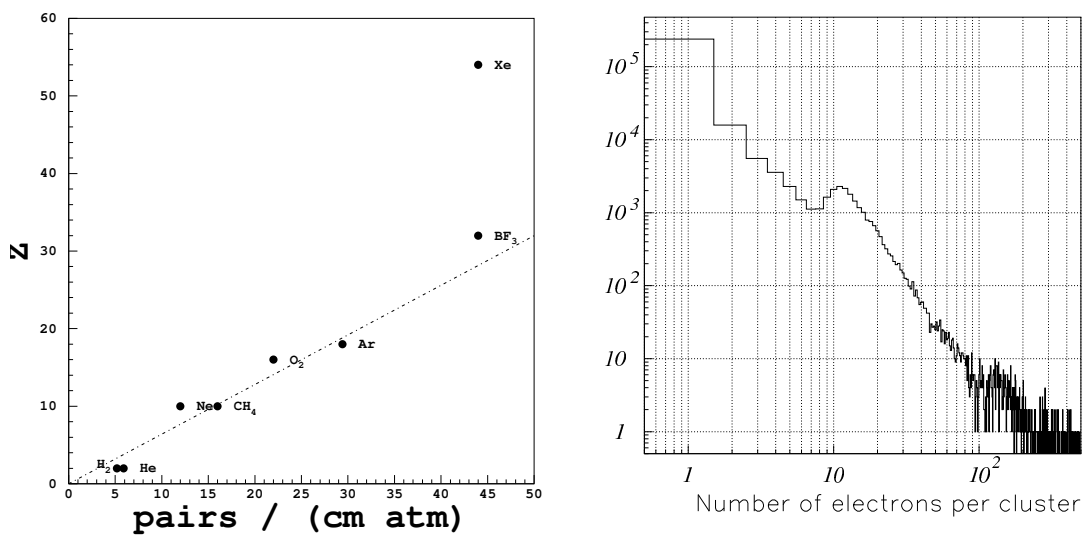

(a) (b)

Figure 3.4: (a) Number of primary ionizing events with rispect to the atomic number of the medium. (b) Electron cluster size distribution for 100 GeV muons in $Ar : CO_2$ (93:7) NTP.

Using the data from table 3.2 and the 3.4, the following values can be derived for a $93\% - 7\%$ mixture of $Ar - CO_2$ under normal conditions:

$$\mathrm{n}_{tot} = (2440/26) \times 0.93 + (3010/33) \times 0.07 \simeq 97 \text{ ion pairs /cm},$$
$$n_p = 29.4 \times 0.93 + 34 \times 0.07 \simeq 29.7 \text{ ion pairs/ cm}.$$

Therefore, the average distance between clusters is of about 1/30 cm $\simeq$ 300 μm and each cluster contains 3 electrons on the average at normal condition. Fig. 3.4(b) shows the cluster size distribution for the same mixture and for 100 GeV muons: the great majority of the collisions release a single electron but a long tail is present as direct consequence of the Landau tail in the energy loss distribution.

Because of the discrete and statistical nature of the ionization process, the MDT signal generated by a traversing muon shows different maxima, related to the individual clusters (fig.3.5), in particular for those passing closer to the wire where drift distances difference between track clusters are enhanched.

The effect of the ionization statistics on the particle position measurements will be discussed further in the chapter.

δ-electrons In a small percentage of the ionizing events, corresponding to the Landau distribution tail, a large fraction of the muon energy is transferred to an electron in a single collision. These electrons, named δ-electrons, are energetic enough to travel macroscopic distances in the gas and produce a secondary track. On the average, 0.01 electrons per centimeter are emitted, in Argon at normal condition, with energy of 30 keV that means a range of about 1 cm ([21]). A δ-electron can also to be produced in the tube wall. In both cases the secondary track can pass closer to the wire than the original muon trajectory. The consequence is a reduced reconstruction efficiency.

photons The interaction process depends strongly on the photon energy. Below 1.02 MeV the dominant processes are the photoelectric effect and the Compton scattering (which may occur both in the gas and in the tube wall). Above this value, pair production is the most probable process. If the photoconversion occurs, likely up to 20 keV or so, the whole photon energy is transferred to a single electron. The spatial range is of few millimiters. This means that the MDT signal caused by a low energy photon interaction presents a single peak shaped structure as shown in fig. 3.5.

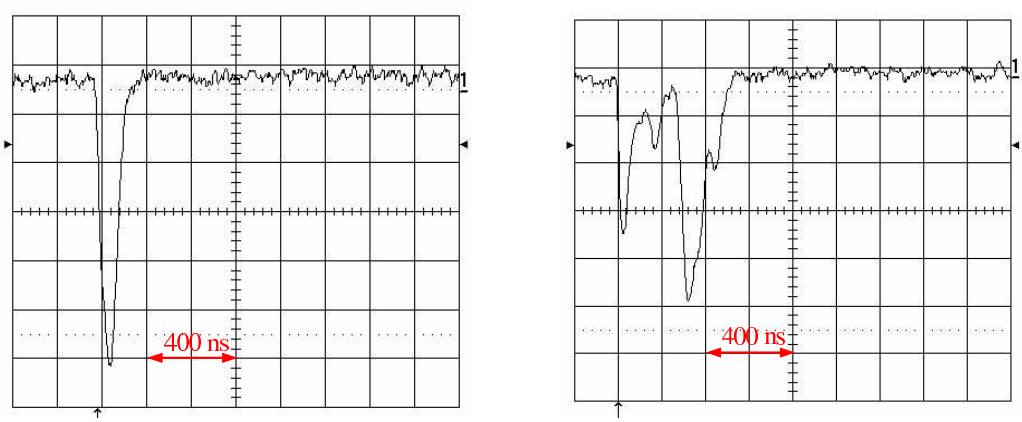

Figure 3.5: Left: MDT signal generated by 22 keV photons from a ^{109}Cd source. Right: MDT signal generated by a muon.

For a photon energy $E_\gamma \sim 100$ keV, instead, the favourable interaction is the Compton pocess. In this case, the scattered electron has a high probability to receive

an energy

$$E_e < E_e^{max} = E_\gamma \cdot \frac{2\gamma}{1+2\gamma}, (\gamma = E_\gamma / m_e c^2)$$

sufficient to traverse the whole tube and ionize the gas originating a signal similar to the muon (fig. 3.5). Similar considerations can be made for photon interaction in the gamma conversion energy range.

neutrons The products of the neutron interaction in the gas , in the tube wall or in the surrounding material are responsible of the ionization. Three processes are possible, depending on the neutron energy. Neutron capture, most probable for thermal neutrons (up to 100 eV), and conseguence photon emission and interaction. For fast neutrons (1 keV - 10 MeV) the recoil of gas nuclei with its associated inization produces a detectable signal. At higher energies ($> 100\ MeV$), charged particles, mainly protons, produces in anelastic neutron collisions are the source of the signal.

3.2.2 Diffusion and Drift

Electrons and ions, produced in the ionization process, quickly loose their energy by multiple collisions with the gas molecules up to the thermal energy $\varepsilon = \frac{3}{2}kT$ ($\simeq 40\ meV$ at the room temperature) being k the Boltzman constant and T the temperature in Kelvin. The energy distribution is given by the Maxwell-Boltzmann function $F(\varepsilon) \propto \sqrt{\varepsilon} \cdot e^{-\varepsilon/kT}$. A point-like cluster, produced at time $t = 0$ in $\vec{r}_0$, in the absence of any external field, starts to diffuse by multiple collisions according to the continuity equation:

$$\frac{\partial n(\vec{r}, t)}{\partial t} - D \cdot \nabla^2 n(\vec{r}, t) \tag{3.5}$$

where n is the particle density and D is the diffusion coefficient of the gas. Therefore, at the time $t > 0$, the particles are distributed in the space according to a Gaussian with center $\vec{r}_0$ and width

$$\sigma^D = \sqrt{6Dt} \qquad (\sqrt{2Dt} \quad \text{in one dimension}). \tag{3.6}$$

In general, the average mean free path between collisions is

$$\lambda = \frac{1}{N\sigma(\varepsilon)} \tag{3.7}$$

if $\sigma(\varepsilon)$ is the collision cross section and $N = \frac{N_A}{A}\rho$ (N_A: Avogadro constant) is the number of molecules per volume.

If charges are exposed to an electric field $\vec{E}$, a drift motion along the field lines is superimposed over the disordered diffusion motion.

The usual expression for the drift is velocity is

$$\vec{v}_{drift} = \mu \cdot \vec{E}. \tag{3.8}$$

The quantity

$$\mu = \mu(\varepsilon, E, \rho) \tag{3.9}$$

is the charge mobility. The mobility is proportional to the average time between collisions τ (3.15): it depends on the particle energy, hence on the electric field strength $E = |\vec{E}|$ also, it is directly proportional to the mean free path (3.13) thus inversely proportional to the gas density; the scaling $\mu(\rho) = \mu(\rho_0)\,\rho_0/\rho$ holds between the values at the two different densities ρ_0 and ρ.

If also a magnetic field $\vec{B}$ is present (as it happens when particle momentum measurements is required) the drift velocity follows the line of the force $\vec{F} = e(\vec{E} + \vec{v}_{drift} \times \vec{B})$ and the angle between $\vec{v}_{drift}$ and $\vec{B}$ is called *Lorentz angle*.

For particles diffusing with thermal energy, the following relation exists between the mobility and the diffusion coefficients (Nernst-Townsend formula):

$$\frac{D}{\mu} = \frac{kT}{e}. \tag{3.10}$$

From 3.6, 3.8 and 3.10 results that the diffusion width of thermal ions and electrons, over a distance $L = v_{drift}\,t$, is independent on the nature of the ion and the gas (thermal limit):

$$\sigma^D = \sqrt{\frac{2kTL}{eE}}. \tag{3.11}$$

The microscopic picture

A simple microscopic model of the particle motion in the gas can be formulated. Between two collisions the drift velocity $\vec{v}_{drift}$ of a particle with charge e and mass m is the sum of the random thermal velocity $\vec{v}_r$, the component $\vec{v}_d$ acquired, in the drift (field) direction, since the previous scattering, and the velocity $\vec{v}_E(t)$ due to the electric field $\vec{E}$ acceleration during the time t:

$$\vec{v}_{drift} = \vec{v}_r + \vec{v}_d + \vec{v}_E = \vec{v}_r + \vec{v}_d + \frac{e}{m}\vec{E}\,t. \tag{3.12}$$

It is assumed $t \leq \tau$ where τ is the average time between collisions:

$$\tau = \frac{\lambda}{v_{rel}} = \frac{1}{N\sigma\, v_{rel}}. \tag{3.13}$$

The quantity v_{rel} is the average relative velocity of the drifting particle and the gas particles in the laboratory frame.

The random thermal contribution $\vec{v}_r$ vanishes once averaged over angles (e.g. over many collisons) and can be neglected. If E is fixed, an equilibrium condition is reached when the momentun gained between two encounters is lost in the next collision. The equilibrium condition is

$$m\,\vec{v_E}(\tau) = f_p\, m\,(\vec{v}_d + \vec{v}_E(\tau)). \tag{3.14}$$

The quantities in 3.14 are assumed averaged over many collisons. The factor f_p is the average fractional momentum loss in the scattering in the field direction Form 3.12, 3.14 results:

$$\vec{v}_{drift} = \vec{v}_d + \vec{v}_E = \vec{v}_E \frac{1-f_p}{f_p} + \vec{v}_E = \frac{\vec{v}_E}{f_p} = \frac{e}{m}\tau\frac{1}{f_p}\cdot\vec{E}. \tag{3.15}$$

This relation justifies the expression 3.8.

Deriving an explicit expression for the relative velocity v_{rel} in the 3.13, the mobility depends on the energy through the scattering cross section σ only. The total energy of a particle moving with instantaneous velocity v is made up of the thermal energy and the energy received from the electric field (ε_E):

$$\varepsilon = \frac{1}{2}mv^2 = \frac{3}{2}kT + \varepsilon_E. \tag{3.16}$$

Two limiting cases can be distinguished according to the field strength.

- Low field limit: $\varepsilon_E << 3/2\,kT$.

  In this case both the gas molecules velocity v_{gas} and the drifting particle velocity v are comparable and the relative velocity can be calculated by the equipartition of energy

  $$v_{rel}^2 =< |\vec{v} - \vec{v}_{gas}| >^2 = v^2 + v_{gas}^2 = 3kT\left(\frac{1}{m} + \frac{1}{M}\right) = 3kT/m^* \tag{3.17}$$

  where M is the mass of the molecules of the media and

  $$m^* = \left(\frac{1}{m} + \frac{1}{M}\right)^{-1} \tag{3.18}$$

  is the reduce mass of the two colliding bodies.

  The scattering can be considered elastic in the energy range considered.

  The factor f_p has the following (non relativistic) expression in case of elastic scattering:

  $$f_p = \frac{M}{M+m}(1 - \overline{cos\,\theta}) = \frac{m^*}{m}(1 - \overline{cos\,\theta}) \tag{3.19}$$

(θ is the scattering angle). In the following the scattering will be assumed isotropic: $\overline{cos\,\theta} = 0$ (which is a good approximation for electrons but not always for ions especially at high momenta). Using 3.13, 3.15 and 3.19:

$$v_{drift} = \frac{e}{m^*}\tau \cdot E = \left(\frac{1}{m^*}\right)^{\frac{1}{2}} \left(\frac{1}{3kT}\right)^{\frac{1}{2}} \frac{e}{N\sigma} \cdot E. \tag{3.20}$$

It follows that mobility is rather constant in the low field limit (fig. 3.6).

- High field limit: $\varepsilon_E >> 3/2kT$. In this case $\varepsilon \simeq \varepsilon_E$ and $v_{rel} \simeq v$. The velocity v reaches the equilibrium value when the energy acquired from the field E between two encounters is lost in the next collision:

$$eE \cdot v\tau = f_E\,\varepsilon = f_E\,\frac{1}{2}mv^2 \tag{3.21}$$

where f_E is the fraction of the total energy ceded to the gas. From 3.15 and 3.21 follows:

$$v^2_{drift} = \frac{e}{m^* N\sigma}\left(\frac{1}{2}\frac{f_E}{f_p}\right)^{\frac{1}{2}} \cdot E. \tag{3.22}$$

It follows that mobility is approximatively proportional to $1/\sqrt{E}$ in the high field limit (fig. 3.6).

—— * ——

It can be demonstrated that the mean displacement σ_D in one direction after a large number $n = t/\tau$ of isotropic scatterings is given by

$$\sigma^2_D = n\,\frac{2}{3}\lambda^2 = \frac{2}{3}\frac{\lambda^2}{\tau}\,t. \tag{3.23}$$

The coefficient D is the part proportional to $2t$ as in the 3.6:

$$D = \frac{\lambda^2}{3\tau} = \frac{v^2_{rel}}{3}\,\tau. \tag{3.24}$$

For particles diffusing with thermal energy, relations 3.17 and 3.20 can be used, and the 3.24 becames $D = kT/e\,\mu$ which is the 3.10.

Ions

Measured values for the mean free path, velocity, and diffusion coefficient of several ions are listed in table 3.3.

For electric field strength normally used for drift chambers the ion mobility is almost independent on the electric field. As shown in fig. 3.6, Argon mobility is constant up

gas	$\lambda(cm)$	v (cm/s)	D (cm$^2/s$)
H_2	1.8×10^{-5}	2.0×10^5	0.34
He	2.8×10^{-5}	1.4×10^5	0.26
Ar	1.0×10^{-5}	4.4×10^4	0.04
O_2	1.0×10^{-5}	5.0×10^4	0.06
H_2O	1.0×10^{-5}	7.1×10^4	0.02

Table 3.3: *Mean free path, velocity and diffusion coefficient for ions in their parent gas (normal conditions).*

to values of the reduced electric field $E/p \sim 20\,V/(cm\,Torr)$([4]) that means up to a distance $\sim 100\,\mu m$ from the wire at the nominal MDT voltage. In fact, a great fraction of the energy aquired by the ions on a mean free path, is lost in the collision with the gas molecules because of the small mass difference. Therefore their energy remains almost thermal and only a small fraction is due to the field. For a mixture of n different gases, the mobility μ_i of the ion i is given by (Blanc's law):

$$\frac{1}{\mu_i} = \sum_{k=1}^{n} \frac{c_k}{\mu_{ik}}, \tag{3.25}$$

where c_k is the concentration by volume of the gas k and μ_{ik} is the mobility of the ion i in the gas k. Measured mobilities of different ions in their own gas or in a different one can be found in table 3.4.

If different type of ions are present, those with higher ionization potentials are neutralised after 10^2-10^3 collisions by the capture of electrons from atoms with lower ionization potentials. Mean free paths are of the order of 10^{-5} cm, only one kind of ions is thus left after a drift length of about $5 \cdot 10^{-2}/k$ cm if k is the percentage of the lowest ionization potential molecules.

Gas	Ion	Mobility (cm^{2}V^{-1}s^{-1})
He	He^+	10.42
Ne	Ne^+	4.10
Ar	Ar^+	1.53
Kr	Kr^+	0.96
Xe	Xe^+	0.57
CO_2	$[CO_2]^+$	1.09
CH_4	$[CH_4]^+$	2.26
Ar	$[CO_2]^+$	1.72
Ar	$[CH_4]^+$	1.87

Table 3.4: Measured mobilities for different ions (normal conditions).

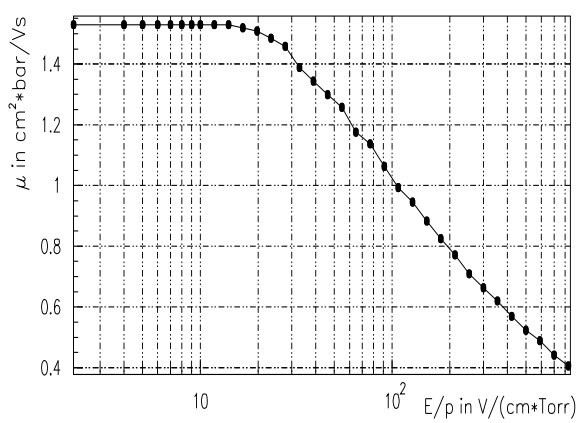

Figure 3.6: Mobility for Ar^+ ions in Ar with respect to the reduced electric field E/p.

[4]The equivalent field at 1 atm is obtained by multiplying by 760.

Electrons

In an electric field, electrons can gain much more energy between two collisions compared to ions because they are lighter and they have a longer mean free path. Moreover the small mass implies that they lose less energy when colliding elastically with the gas molecules. For these reasons electrons can reach random energies several orders of magnitude higher than the thermal one. In a simplified model the drift velocity can be written as

$$v_{drift} = \frac{e}{2m_e} E\tau, \tag{3.26}$$

where $\tau(E, \varepsilon)$ is the average time between collisions. The collision cross section and, on the consequence τ, depends critically on the electron energy and the electric field. In fact, electron energy can easily pass the threshold of inelastic excitation of the gas molecules; in this case, the drift velocity (the mobility) becomes a function of the energy loss associated with such process.

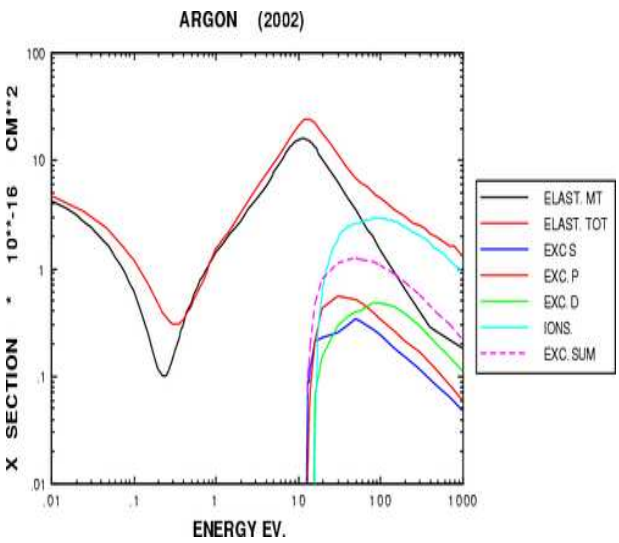

Figure 3.7: Collision cross section for electrons in Argon as function of the energy.

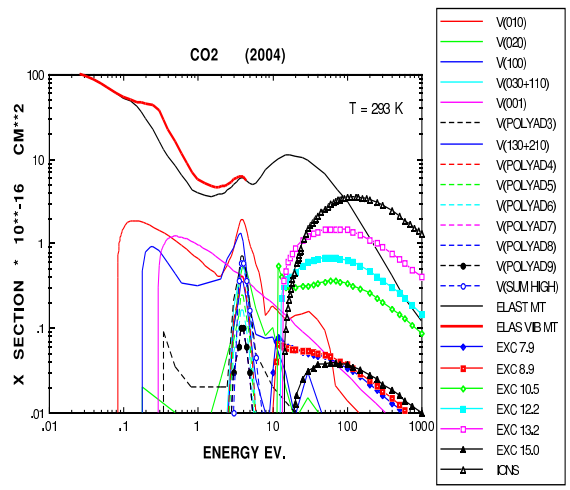

Figure 3.8: Collision cross section for electrons in CO_2.

A characteristic phenomenon which may occour for electrons in the eV range is the Ramsauer effect. At these energies electrons wavelength are comparable to bound electron orbits in the molecules of the gas and quantum mechanical effects arise which make the atoms nearly transparent to electrons, i.e. leads to a minimun in the collision cross section. An example of this behaviour is given by the cross section of electrons in Argon (fig. 3.7). The energy distribution will favour those energies for which the interaction cross section is lower. An increase in the energy in fact implies an increase in the probability of scattering with the subsequent energy loss. This tends to keep electron energy close to the cross section minimum. This effect leads to a saturation of the drift velocity which remains almost constant with increasing electric field (fig. 3.9 for pure Argon).

The major consequence of the sensitive dependece of the cross section on the energy is that drift velocity can vary cosiderably with small changes in the gas composition since one gas may have a large scattering cross section where another has a minimum. This happens for example for mixture of Argon with polyatomic gases. In fig. 3.8 is shown the cross section for carbon dioxide. Figure 3.9 instead shows some examples of drift velocity versus the electric field for different gases and compositions.

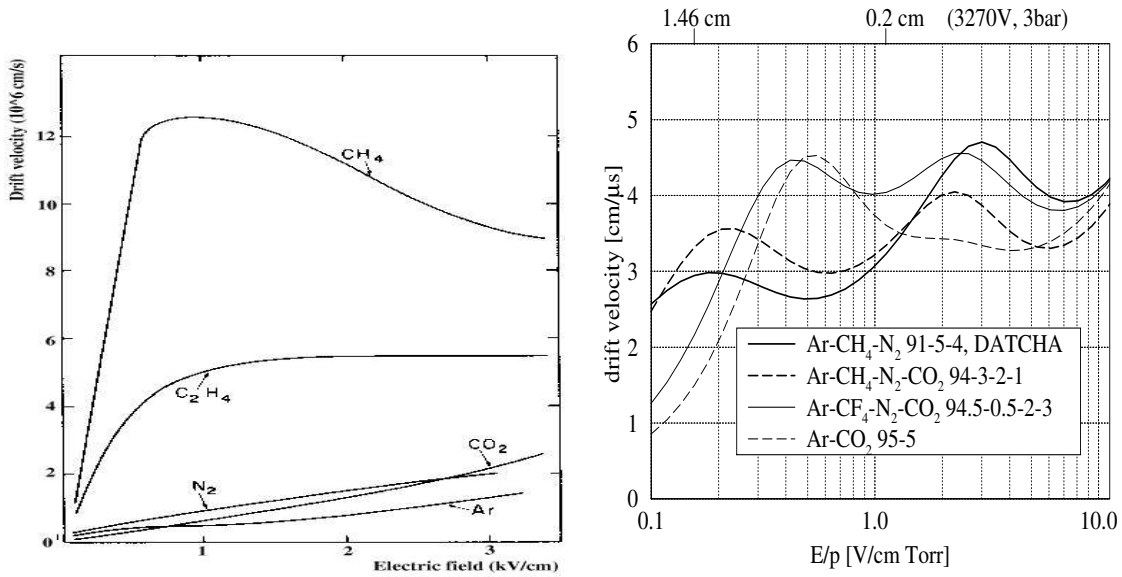

Figure 3.9: Drift velocity for several gases.

Drift velocities of the order of 10^6 cm/s can be attained before saturation sets in. On the average, the electrons drift velocity is three order of magnitude higher than the ions velocity.

3.2.3 Ionization amplification. Gain

Drifting towards the anode, electrons gain more and more energy between two consecutive collisions due to the increasing electric field strength. When their kinetic energy is such to cause gas ionization an avalanche multiplication process sets in.

If α is defined as the average number of electron-ion pairs produced per unit length ($\alpha = N_p \sigma_i$ if N_p is the number of molecules per unit volume and σ_i the inization cross section for electrons), a given number N of pairs is then augmented to $N + dN$ over the length dr where

$$dN = \alpha \cdot N \cdot dr. \tag{3.27}$$

For a given gas mixture, the coefficient α (first Townsend coefficient) depends strongly on the electric field and gas density. The final number N of electrons in the avalanche is obtained by integrating 3.27 between the point r=r_0 where the mul-

tiplication starts (and N_0 electron-ion pairs are present) and the wire surface (r=a):

$$N = N_0\, e^{\int_{r_0}^{a} \alpha(E(r))\, dr} = N_0\, e^{\int_{E(r_0)}^{E(a)} \alpha(E)\, \frac{dr}{dE}\, dE}. \tag{3.28}$$

The quantity $G = N/N_0$ is usually called *gain* and represents the amplification factor of the drift tube.

Because of the nature of the underlying phenomena involved, the amplification is a statistical process. Fluctuations $g = G/\bar{G}$ around the mean value $\bar{G}$ (given by the 3.28) are well described, for a cylindrical geometry, by a Polya distribution:

$$f(g) \propto g^{\Theta} \cdot e^{-(\Theta+1)\, g}. \tag{3.29}$$

The parameter Θ ($0 < \Theta < 1$) is related to the fraction of electrons whose energy exceeds a threshold energy for ionization and depends on the gas properties and on the field geometry [26].

Equation 3.28 can be integrated assuming α to be proportional to the electric field. Measurements state this is a good approximation for heavy noble gases between 10^3 and 10^4 V/cm, a typical range for drift detectors near thin wires. The result is (Diethorn's formula):

$$G = \left[\frac{E(a)}{E_{min}(\rho)}\right]^{\frac{ln2 \cdot a \cdot E(a)}{\Delta V}}. \tag{3.30}$$

The minimum field E_{min} at which the multiplication can start is given by the ratio of the energy required to ionize the molecules of the media to the mean free path between collisions. Therefore E_{min} is proportional to the gas density ($E_{min} = E_{min}(\rho_0)\, \rho/\rho_0$ if $E_{min}(\rho_0)$ is the value given a the density ρ_0). The quantity $e\, \Delta V$, instead, is the average energy required to liberate an electron in the gas. The field at the wire surface ($E(a)$) can be calculated from the 3.1.

Gain measurements for different values of the applied voltage are shown in 3.10 for several Ar:CO_2 mixture at 3 bar [25]. For the 93:7 choice, aperated at 3080 V, the gain is about $2 \cdot 10^4$. Fits to the measured points give the following values of the Diethorn parameters:

$$\Delta V = 34\, V, \;\; E_{min} = 24\, kV/cm$$

for ρ_0 at 1 bar and 295 K (errors are about 10%). From the E_{min} value results that $r_0 \simeq 200\, \mu m$.

Mode of operation

In 1 cm of Argon NTP about 100 electrons are released by a minimum ionizing particle. A signal consisting of such a little amount of charge is impossible to detect since the electronic read-out noise is orders of magnitude higher (par. 3.3.2). Hence

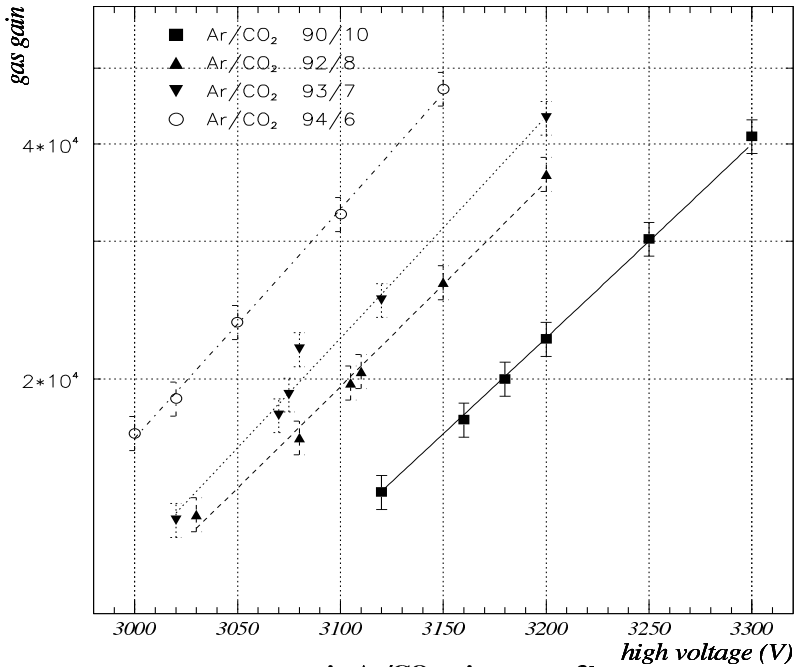

Figure 3.10: Gas gain for different $Ar : CO_2$ mixtures.

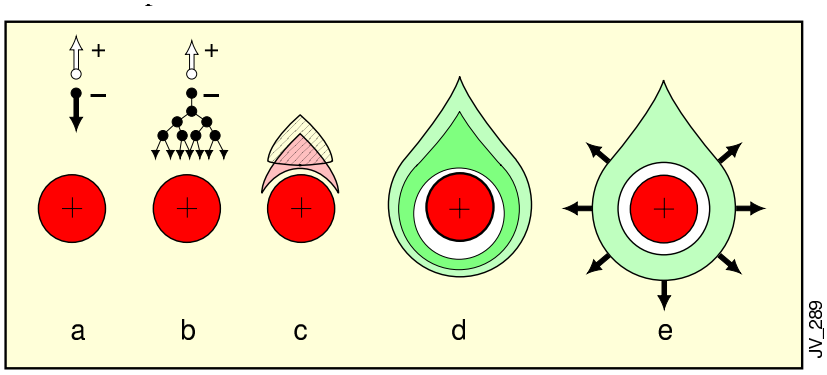

Figure 3.11: Avalanche development steps. Ions separate from electrons as the avalanche approches the anode. The drop-like shape surrounding the wire is due to lateral diffusion.

ionization amplification is necessary. In order to be useful, however, field geometry must be cosidered also. If, for example, the electric field is uniform between cathodes, the detected signal will depend on the avalanche length. For events with the same energy deposit, the signal amplitude will then vary with position and proportionality between energy and signal amplitude is lost. Moreover, spark break down rate would be very high along the whole drift path making the detector operation stable only for low value of the gain.

These limitations are overcome in a cylindrical geometry where the electric field, thanks to the $1/r$ dependence, is relatively weak along the drift path besides close to the wire surface. Electrons produced in the primary ionization simply drift along the field lines until the proximity of the anode (typically few wire radii) where the condition for the avalanche to start is met. Fig. 3.11 illustrates the time development of the avalanche. Gain as high as 10^5 can be achieved with this kind of detectors before proportionality is lost. The maximun value depends strongly on the gas used.

3.2.4 Development of the signal

The signal on the elctrodes is induced by the movement of the charges.

Considering an electron drift velocity of 5 $cm/\mu s$ and that the drift path of the electron avalanche is only as big as the amplification zone ($\sim 100\mu m$) the whole multiplication process lasts few nanoseconds. Therefore electrons induce a very short signal and the size and time development of the whole signal is determined mostly by the ion drift.

If the anode is kept at the constant potential V, the current signal I induced on an electrode by a carge q in $\vec{r}(t)$ moving with velocity $\vec{v}(\vec{r})$ in the field $\vec{E}(\vec{r})$ can be conveniently calculated using the Ramo's theorem [22]:

$$I(\vec{r}(t)) = -\frac{q}{V} \cdot \vec{v} \cdot \vec{E}. \tag{3.31}$$

With $\vec{E} = \frac{V}{ln(b/a)} \frac{1}{r} \hat{r}$ and $\vec{v} = \mu \vec{E}$, 3.31 becomes

$$I(r) = \frac{qV\mu}{(ln\frac{b}{a})^2} \cdot \frac{1}{r^2}. \tag{3.32}$$

The ion mobility can be assumed to be constant outside the avalanche region (see par. 3.2.2). In this approximation, if the ion is produced at the distance r_0 from the wire, the time it takes to move from r_0 to r is

$$t(r) = \int_{r_0}^{r} \frac{dr'}{v(r')} = \frac{ln(b/a)}{\mu V} \int_{r_0}^{r} r'\, dr' = \frac{1}{2} \frac{ln(b/a)}{\mu V} \cdot (r^2 - r_0^2). \tag{3.33}$$

from which follows

$$r^2(t) = \frac{2\mu V}{ln(b/a)}(t + t_0), \qquad t_0 = \frac{r_0^2}{2\mu V} ln(b/a). \tag{3.34}$$

The time t_{max} needed to reach the tube wall is then

$$t_{max} = t(b) = \frac{ln(b/a)}{2\,\mu V}(b^2 - r_0^2). \tag{3.35}$$

Substiting 3.34 in 3.32:

$$I(t) = \frac{q}{2ln(b/a)} \cdot \frac{1}{t + t_0}, \qquad 0 \leq t \leq t_{max}. \tag{3.36}$$

The current induced by a single ionization cluster of n_p electrons, in the approximation that the whole charge multiplication occurs at the point r_0 is obtained setting

$$q = e\, n_p\, G. \tag{3.37}$$

Assuming $\mu \simeq 1.7\ cm^2/(Vs)$, $a = 25\,\mu m$, $b = 1.46\,cm$, $V = 3080\ V$, q=e=1.61 $\times$ $10^{-19}\ C$; $G = 2 \cdot 10^4$ and $n_p = 3$, $r_0 \simeq 70\ \mu m$ for Argon at 3 bar results that:

$$t_0 \simeq 30\,ns, \quad t_{max} \simeq 1.3\,ms \text{ and } I(0) \simeq 0.26\,\mu A. \tag{3.38}$$

The 3.36 implies that the rise of the voltage signal $V(t)$ is very fast:

$$V(t) \propto \int I\,dt \propto ln\left(1 + \frac{t}{t_0}\right). \tag{3.39}$$

This can be seen also from the espression of the fraction of the total charge integrated over the time t:

$$\frac{Q(t)}{Q(t_{max})} = \frac{\int_{t_0}^{t} I(t')\,dt'}{\int_{t_0}^{t_{max}} I(t')\,dt'} = \frac{\ln\left(1 + \frac{t}{t_0}\right)}{\ln\left(1 + \frac{t_{max}}{t_0}\right)}. \tag{3.40}$$

Using the values in 3.38, it can be estimated that half of the total charge is integrated already after a time $t \simeq 6\,\mu s \simeq 5 \cdot 10^{-3}\,t_{max}$. According to the t_0 definition the fraction increases with decreasing anode wire radius.

3.2.5 Gas mixtures

One of the basic properties of a detector gas mixture is the stability of the operation at high gain and low voltage.

The principal component of a desirable gas is usually a noble gas such as Argon. Noble gases allow multiplication at relatively low electric fields. In fact they do not have molecules: this means that electrons are easily accelerated as they mostly undergo elastic collisions with little loss of energy, and that the inelastic collisions are dominated by ionization rather than excitation processes. Moreover electrons can easily be absorbed in complex molecules.

Argon is usually preferred since it gives more primary ionisation than He or Ne and is more affordable than than Kr or Xe.

However a gas detector filled with a noble gas only does not allow stable operation. During the avalanche process many Ar atoms are excited and decay emitting UV photons (e.g. with an energy of 11.6 eV). These photons can strike the cathode (Aluminum has a ionisation threshold of 6 eV) and eject photoelectrons which give rise to another avalanche. There is therefore a positive feedback and a continuous discharge sets in. A chamber filled with pure Ar suffers from such breakdown at relatively low gain. Some kind of gases can be added in order to *quench* the secondary avalanches. Polyatomic gases have many non-radiative vibrational and rotational excited states over

a wide energy range. If a chamber contains a fraction of such a gas, its molecules will absorb energy from excited argon atoms by colliding with them or by dissociating into smaller molecules. Since $\sigma_{emission} << \sigma_{collision}$ the UV photon emission is eliminated or quenched. The presence of a quenching gas can allow an enormous increase in stable gain obtainable. Carbon dioxide (CO_2) Isobutane (C_4H_{10}), methane (CH_4) as well as many hydrocarbons and alcohols belong to this type of gases.

Symptoms of an imperfect quenching is, for example, the presence of spurious signal pulses at $t \simeq t_{max}$ (after pulsing) with the consequent increase of the dead time and resolution reduction.

3.3 Electronics

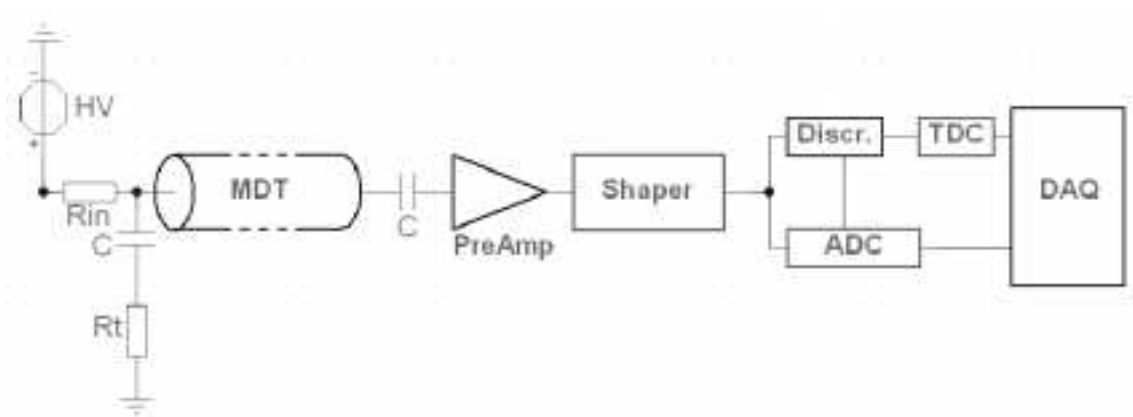

Figure 3.12: MDT electronics scheme.

Fig 3.12 shows a schematic view of the electronics of an MDT. On one side of the tube (HV side) the high voltage is provided to the anode wire while the tube wall is grounded. The current signal is read at the other side of the tube (RO side), amplified, shaped and then presented to a discriminator. The logical output signal of the discriminator is sent to a TDC which measures the time difference between the pulse and the signal provided by an external trigger. An ADC chip integrates the discriminated signal over a defined time window (*gate*). Such a circuit allows for drift time measuments in fact, if the pulse comes from a triggering muon then the TDC time is equal to the drift time plus a constant due to signal propagation time in the electronics. The TDC information can be used for position measurements as discussed further.

As reported at the end of the par 3.2.4 the signal induced in the tube is characterised by a very short rise time. Atlas MDT are used for precise position mesurements therefore high timing resolution is required. This means that the relevant information is mostly contained in the early portion of the pulse. It is not convenient either to

use the entire signal since it will introduce events pile-up effects and a large dead time in the read-out chain reducing the high event rate capability of the system. The long signal tail is shorten by means of a double differentiator circuit (the shaper module in the figure) which attenuates the low frequency components.

In the next pragraphs the various steps involved in the signal processing are descibed in more detail.

3.3.1 The tube circuit

A simple model of an MDT tube, including also the High Voltage (HV) distribution and part of the on-chamber read-out electronics, is shown in figure 3.13. The resistor

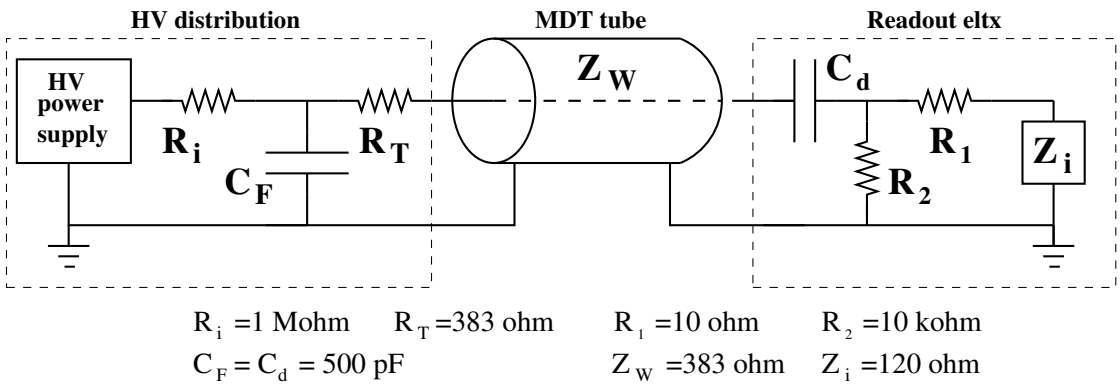

Figure 3.13: A simple model of the tube. The HV distribution and part of the on-chamber read-out electronics is also drawn.

R_i=1 $M\Omega$ is the HV protection resistor it limits the current in case of breakdown. The capacitor C_F=500 pF is a filter connected to ground which minimizes the HV induced noise. R_T=383 Ω is the termination resistor, equal to the tube impedance in order to avoid signal reflections. C_d = 500 pF is the HV decoupling capacitor, R_2=10 $k\Omega$ is a protection resistor, on the read-out side, Z_i=120Ω is the input impedance of the amplifier. The tube characteristic impedance is $Z \simeq \sqrt{L/C}$=380 Ω, where $L=\frac{\mu}{2\pi}ln(b/a)$ and $C=\frac{2\pi\epsilon}{ln(b/a)}$ are the capacitance and the inductance per unit length (for gases $\epsilon=\epsilon_0$ and $\mu=\mu_0$).

The voltage at the output of the front-end electronics is shown in figure 3.14(b) [27].

3.3.2 Read-out

The full read-out chain is made in three different steps:

1. Amplification, shaping and discrimination of the tube signal

2. Time to digital conversion and charge to digital convertion

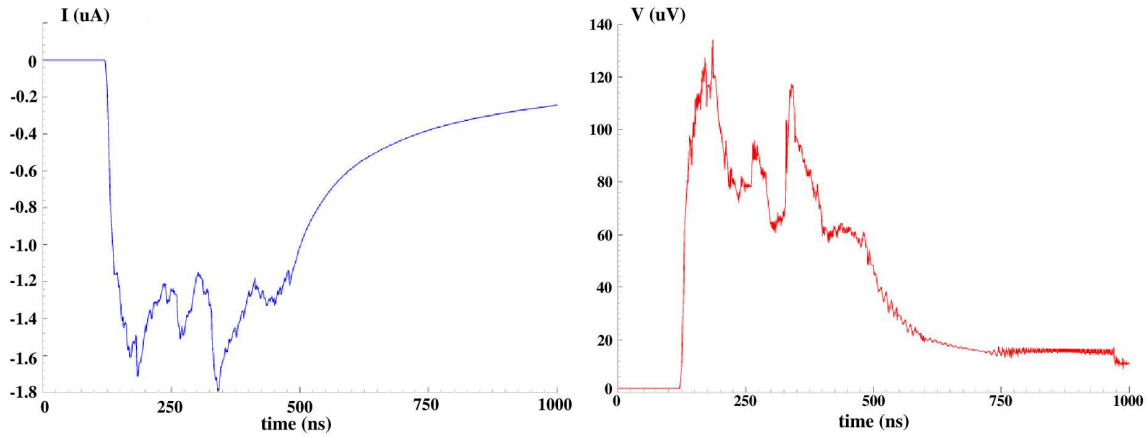

(a) Current (μA) induced on an MDT wire as seen at the tube signal pin

(b) Voltage signal (μV) induced at the amplifier input

Figure 3.14: Current and voltage signal induced by a charged particle at the input of the read-out electronics.

3. Electronics initialization and chamber data collection

The first two steps are performed by two different chips (ASD [27] and AMT [28]) both mounted on a front-end board (*mezzanine*) which is connected to the tubes via

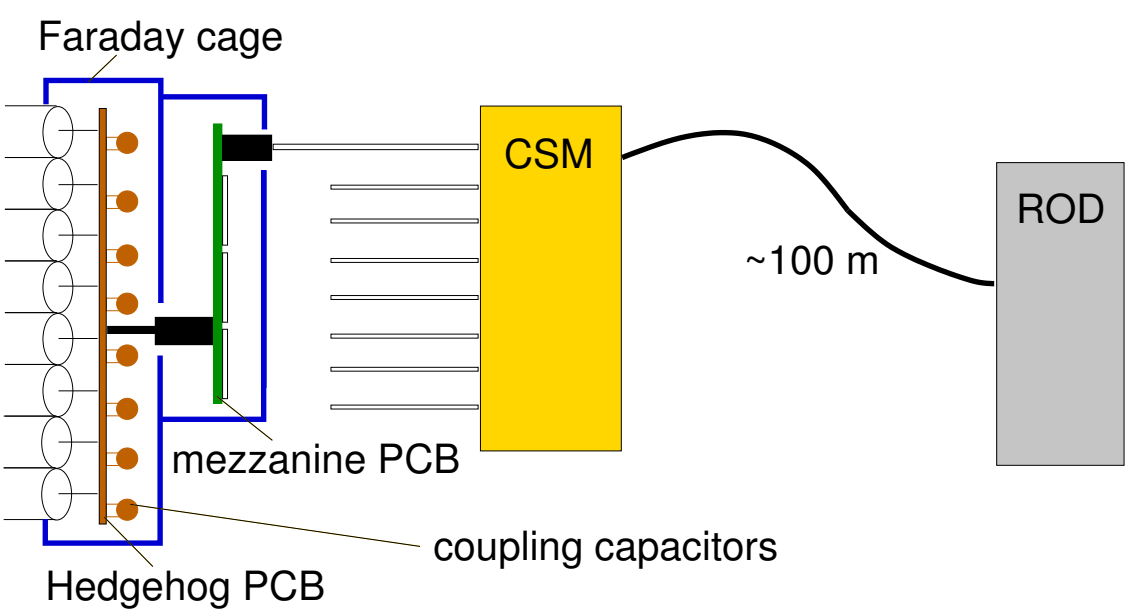

Figure 3.15: Scheme of the MDT read out system.

a two layer printed circuit board (the "*hedgehog*") which is mounted directly onto the ends of the tubes. The hedgehog couples the electronics capacitively to the wires and provides a discharge protection for the amplifier input. For a MDT of the type BIL, for example, 6×4 tubes, 6 in each of the 4 layers of a multilayer, are read out via one hedgehog and one mezzanine board. The High Voltage is connected to the tubes via different hedgehog boards at the opposite end of the tubes. Both ends of each multilayer are enclosed by a Faraday cage. The different mezzanines of each chamber are then read by the CSM (Chamber Service Module) which is a board mounted directly on the chamber. The CSM provides the interface between the on-chamber read out electronics and the Data Acquisition System (DAQ). In the ATLAS detector, the data will be delivered from the CSM by about 100 m long optical fibres to the Readout Driver modules (ROD). A scheme of the read out layout id shown in fig. 3.15

The ROD board performs both data collection and initialization of the parameters of the ASD and AMT chips. A description of the read-out chain and of the software used for this purpose is given in chapter 4.

A block diagram of the ASD (Amplifier, Shaper, Discriminator) chip is given in figure 3.16 while in table 3.5 the most relevant analog specification of the ASD are given.

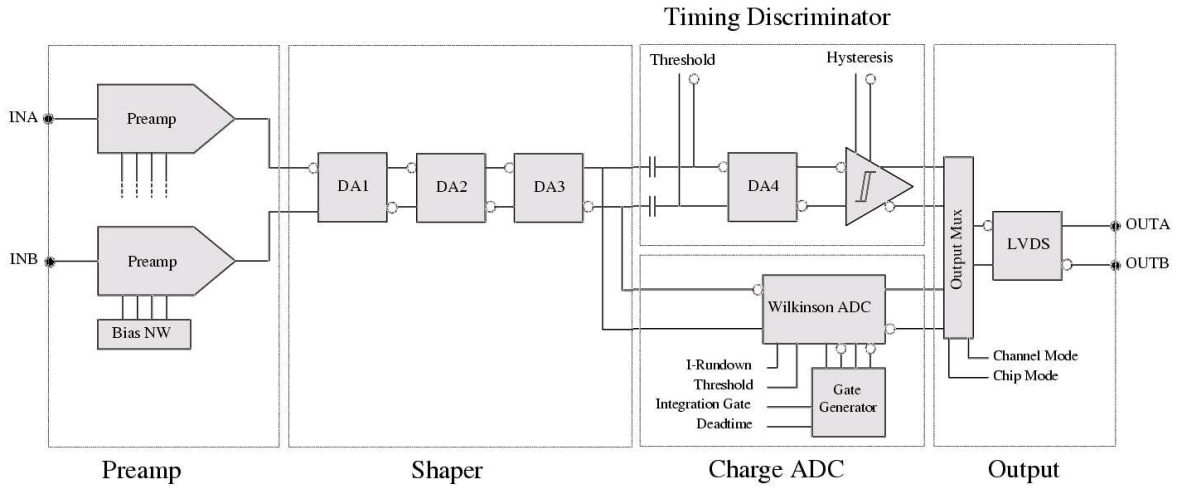

Figure 3.16: Block diagram of the ASD chip.

Each tube is connected to a preamplifier (a second preamplifier is inserted to provide DC balance for the subsequent stages and a common-mode rejection of noise). The amplified signal is sent to a series of three differential amplifiers (DA1, DA2, DA3) that provide signal gain and implement bipolar shaping. Bipolar shaping was chosen to prevent baseline shifts caused by the foreseen high ionization level.

The output of the shaper is split and sent to an ADC and to a discriminator. The ADC integrates the signal in a given time gate and stores the charge in a capacitor that is then discharged with a constant *run-down* current. The discharge time is

proportional to the pulse charge. The leading edge timing and the pulse width are read and converted into digital data by the AMT TDC.

The signal is also sent to a discriminator which commutes when the signal is higher than a programmable threshold to measure the leading edge of the signal. A useful way to parametrize the threshold of the discriminator is in term of number of primary electrons N_{thr}. Converting N_{thr} in the value of the voltage requires the knowledge of the amplifier response as a function of frequency. The response function is the output of the device when the input is a current signal $q\delta(t)$. For the ASD it is 12 mV/fC (table 3.5). As the amplifier has a limited bandwidth, the response function is a curve with a finite rise time τ_s (*peaking time*) of about 15 ns. For an input current given by 3.36 the corresponding sampled charge is

$$Q(\tau_s) = \int_{t_0}^{\tau_s} I(t')\,dt' = \frac{eN_{thr}G}{2ln\frac{b}{a}} ln\left(1+\frac{\tau_s}{t_0}\right) = eN_{thr}Gf(\tau_s) \tag{3.41}$$

where G is the gas gain and $f(\tau_s)$=0.031 (for t_0=30 ns, see 3.38). For a gas gain of $2{\cdot}10^4$ we have Q=0.25 fC (3 mV signal) per primary electron.

The value of the threshold N_{thr} has to be fixed taking into account the electronic noise which can be expressed in terms of ENC (Equivalent Noise Charge) for a direct comparison with the signal. ENC is the amplitude, expressed in equivalent electrons, of a signal equal to the r.m.s of the electronic noise. In the ASD the noise level is 6000 electrons (table 3.5). In order to have the amplitude of ionization signals larger than the noise

$$N_{thr}Gf(\tau_s) > ENC \tag{3.42}$$

must hold for a given threshold. This expression relates threshold and gas gain; the choice of their value will be discussed in the next paragraph .

In the final stage of the ASD chip, the signals are sent to an LVDS cell that converts them to external low level signals. These signals are then sent to the AMT TDC chip which is also mounted on the mezzanine board.

A simulation of the signal in the different stages is shown in figure 3.17 [27].

In figure 3.17(a) the output of the pre-amplifier is shown while in figure 3.17(b) the bipolar output of the shaping system is shown. In figure 3.17(c) a threshold of 60 mV has been applied. In figure 3.17(d) the final signal and the discriminator output is shown.

Input impedance	$Z_I = 120\ \Omega$
Noise	ENC=6000 e r.m.s.
Shaping function	bipolar
Shaper peaking time	$\tau_s = 15$ ns
Sensitivity at shaper output	12 mV/fC (delta pulse into terminated MDT)

Table 3.5: ASD analog specifications.

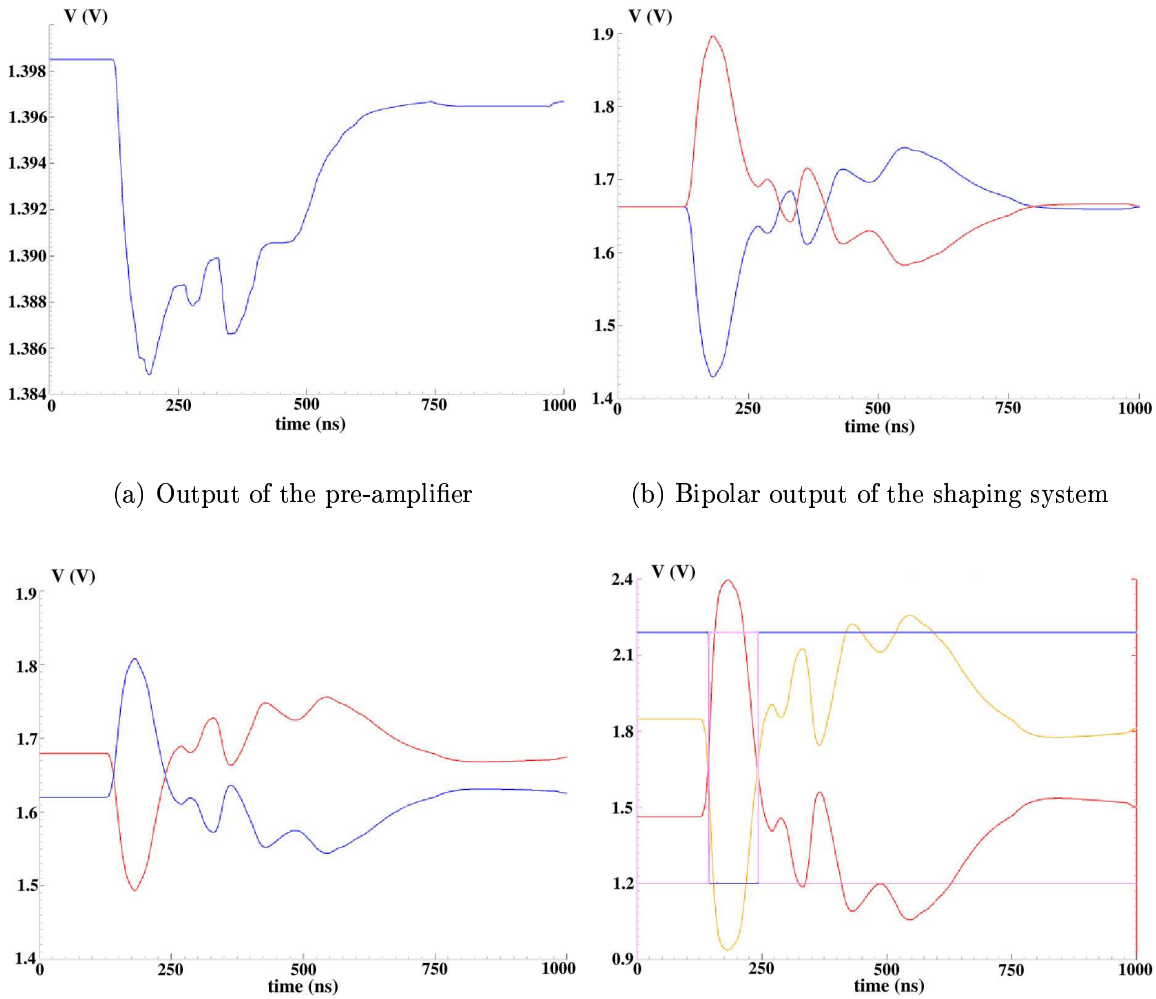

(a) Output of the pre-amplifier

(b) Bipolar output of the shaping system

(c) Bipolar signal with a 60 mV threshold applied

(d) Final signal and discriminator output

Figure 3.17: Simulation of the signal in the different stages of the ASD chip.

The AMT TDC chip is a 24 channel programmable TDC. All detector front end electronics is clocked at the LHC frequency of 40 MHz; as the TDC works with a 5-bit interpolator, the least count is 25/32=0.78125 ns. This TDC measures the starting time of the signal with respect to an external trigger that receives through the CSM; also the width of the signal can be measured as it can be related to the charge collected by the ASD.

Further information about the ADC and TDC operation will be given in in the chapter 4.

3.4 Background environment

The enormous rate of proton-proton collisions at the Large Hadron Collider (10^9 collisions per second) is one of the major challenges for the *LHC* experiments. The large amount of particles produced at the interaction point makes the wire aging, radiation damage, activation of detector parts, and radiation-induced backgrounds in the detector a major concern and has a critical impact on the design of the whole system.

The expected background condition defines parameters such as the rate capability of single tubes and the aging properties, granularity and redundancy of the trigger logic, the pattern recognition efficiency, and are an important input for the choice of the baseline gas and the front-end electronics [30].

The background sources in the Muon Spectrometer can be classified into two main categories:

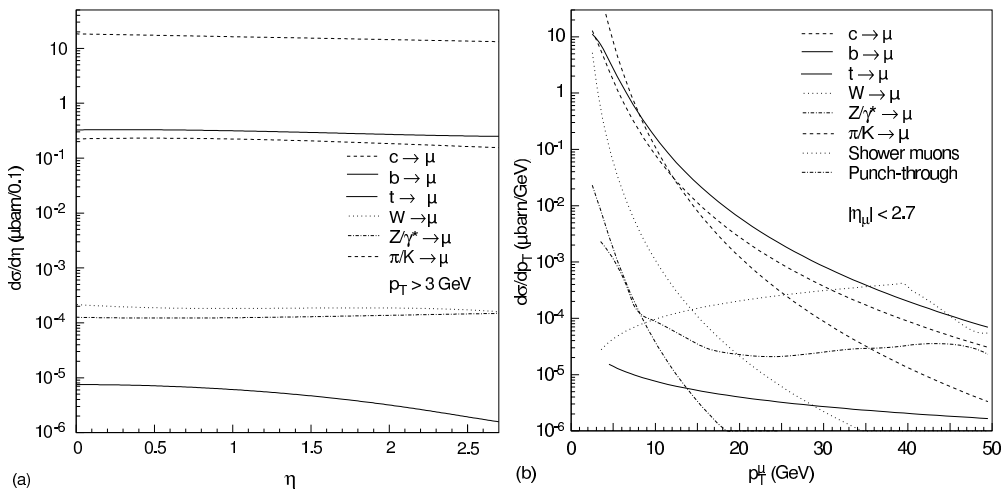

Figure 3.18: Simulate inclusive cross section for primary collision products: (a) as a function of the psudorapidity integrated over $3 < p_t < 50\ GeV/c$; (b) as a function of p_t integrated over $|\eta| < 2.7$.

- **Primary backgound** Primary collision products penetrating into the Muon Spectrometer through the calorimeters, are correlated in time with the $p-p$ interaction. As shown in fig. 3.18 the sources of primary background are semileptonic decays of light ($\pi, K \rightarrow \mu X$) and heavy (c, b, $t \rightarrow \mu X$) flavours, gauge Boson decays ($W, Z, \gamma^* \rightarrow \mu X$), shower muons and hadronic punch-through. At small p_t (less than 10 GeV/c), the largest source of background are muons from π/K decays in flight; depending on pseudorapidity, muons with momenta from 3 GeV/c to 6 GeV/c will be absorbed in the calorimeters. At moderate p_t (above 10 GeV/c), *top* and Z decays also give a sizeable contribution.

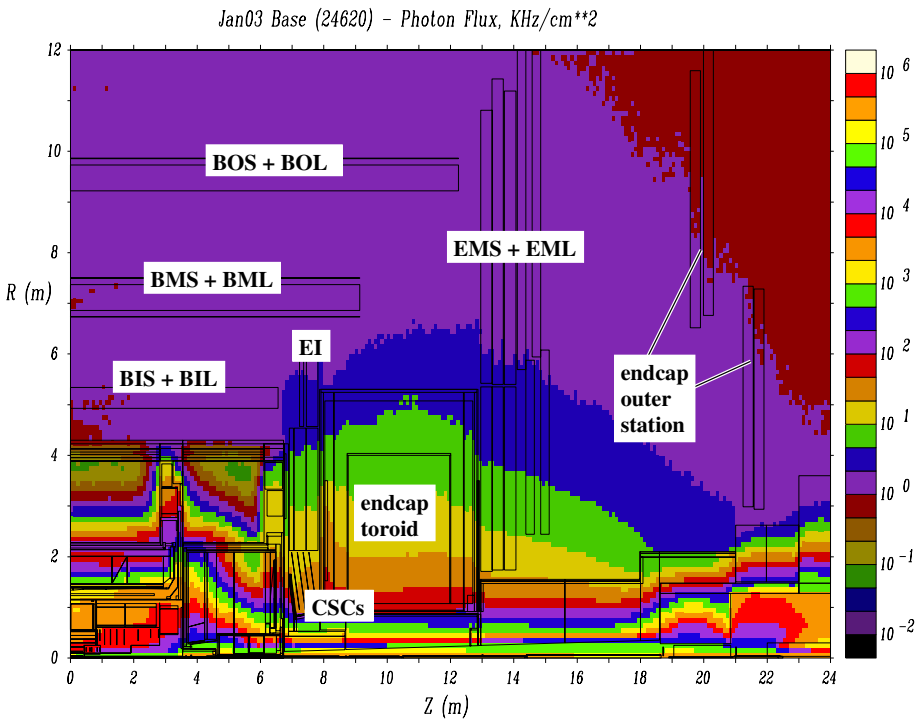

Figure 3.19: Photon flux (kHz/cm^2) in an ATLAS quadrant (GCALOR simulation).

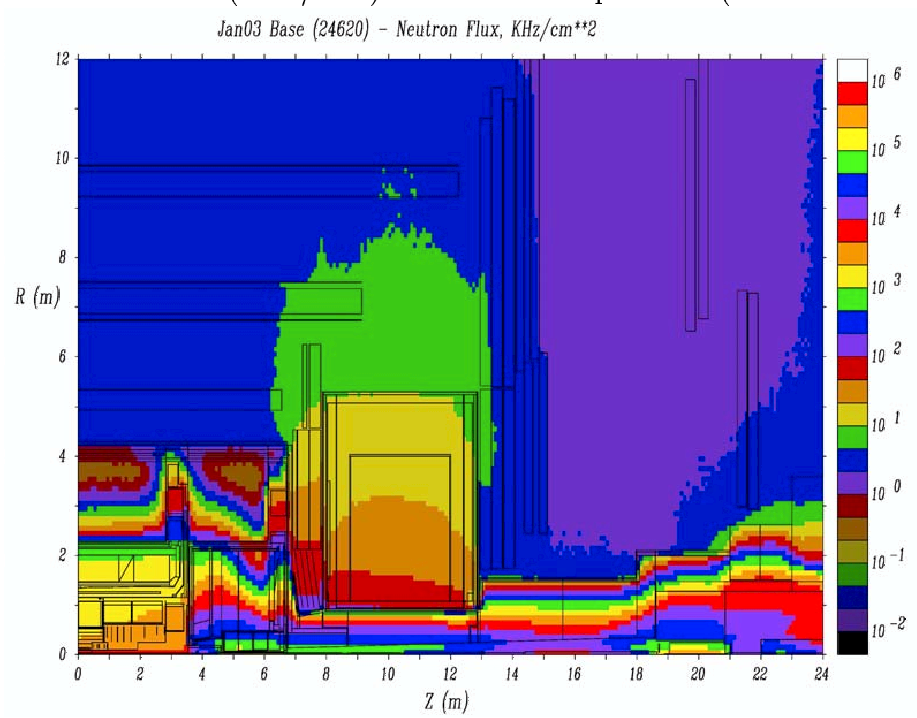

Figure 3.20: Neutron flux (kHz/cm^2) in an ATLAS quadrant (GCALOR simulation).

From the point of view of the particle rate the primary background is negligible compared to the uncorrelated background, which is discussed in the next point. The maximum expected particle flux due to the primary background is of the order of 10 Hz/cm^2 in the innermost precision chamber.

- **Radiation background** When high-energy particles from the interaction point enter detector material and machine elements (beam pipe, calorimeter, shielding material etc.), they begin to shower. If the material is thick, the shower development will continue until most charged particles have been absorbed; the remnants are mostly neutrons and associated photons. Electromagnetic showers are absorbed very rapidly, while neutrons travel long distances, losing their energy gradually. Nuclear capture of thermal neutrons frequently results in the production of photons via (n,γ) reactions. The typical photon energies from these processes range from 100 keV to up to some MeV.

  Neutrons produced in the showering process are scattered many times before being captured, giving rise to a rather uniform background radiation in the muon spectrometer. This background enters into the spectrometer from all directions and is not any longer correlated in time time to the primary $p-p$ interaction.

  Figures 3.19 and 3.20 show the expected flux of photons and neutrons obtained with the GCALOR (Jan03 version) Monte Carlo. The maximum flux is of about 10 kHz/cm^2 for photons and 5 kHz/cm^2 for neutrons.

  The particle flux is higher in the inner layer of the forward regions since most of the hadrons are produced at small angles with respect to the beam axis.

3.4.1 Expected counting rate

The radiation background affects the muon system mainly by generating uncorrelated noise hits in the chambers with the consequent pattern recognition degradation, space-charge build-up and aging.

The counting rate is an estimator of the rate at which drift tubes in the muon system will count in response to the background particle rates. It can be evaluated as:

$$\gamma \times \varepsilon_\gamma + n \times \varepsilon_n + p + \pi + \mu + 0.25 \times e. \tag{3.43}$$

Where γ, n, π, μ, e stand for the particles flux while ε_γ, ε_n are the photon and neutron chamber sensitivity([5]). The sensitivities to charged particles is taken as 100 %. The electron flux is multiplietd by a factor 0.25 to avoid double counting of electrons produced in photon interaction in the surrounding materials [30]. Since all these quantities depend on the energy in the 3.43 is implicit the convolution with the individual

[5]Efficiency for a particle to produce a detectable signal (hit) in the chamber.

particle energy distibution. Figures 3.21 and 3.22 show particle flux and sensitivity for neutron and photons as a function of the energy.

Average values used for the estimations are 8×10^{-3} and 5×10^{-4} for the sensitivity to photons and neutrons respectively.

Despite the low sensitivity the relative contribution to the counting rate is dominated by neutral particles because of their higher flux with respect to charged particles.

In particular, photons contribute for about 70% while neutrons contribute at 10% level.

The evaluated count rate is reported in fig. 3.23 for the different spectrometer stations. For the $MDTs$ it ranges from about 10 Hz/cm^2 in the middle of the barrel to about 100 Hz/cm^2 for $|\eta| \sim 2$([6]).

MDT chambers have been designed to handle up to 5 times the estimated counting rate. In fact, several sources of uncertanties have to be taken into account: due to the limited knowledge of the shower processes in the calorimeters and of the (n,γ) cross-section, the simulated photon and neutron fluxes might be wrong by a factor of 2.5; chamber sensitivities could be in error by a factor of 1.5 from comparison between different simulation programs and measurements; finally the uncertainty in the $p-p$ cross-section and in the multiplicity of the particles produced in the primary collision is estimated to be $\pm 30\%$.

A conservative linear superposition of these uncertainties yields a factor of five. The ATLAS muon instrumentation is therefore designed to operate at a nominal luminosity of $10^{34} cm^{-2} s^{-1}$, allowing for a safety factor of five on the background rate.
Consequently the highest background rates for one MDT is assumed to be 500 Hz/cm^2.

3.4.2 Accumulated charge

During the ionization amplification process, described in 3.2.3, the great amount of drifting charges present in a restricted region (the avalanche) around the anode, can prime chemical reactions with the conseguent deposit of molecular compounds on the wire. This leads to a progressive deterioration of the tube performance and might finally compromise the tube operation. This phenomenon, usually called aging, is described in detail in Chapter 7. The aging of a given drift tube, after the period of operation ΔT, is therefore proportional to the total charge Q produced in gas during the interval ΔT. The quantity Q is usually expressed in unit of length and can be written as

$$Q = R \cdot d \cdot \bar{n}_e \cdot G \cdot e \cdot \Delta T \tag{3.44}$$

where R is the counting rate per unit area as defined in the previous paragraph, d is the tube diameter, $\bar{n}_e$ is the average number of primary ionization electrons (e is the electron charge) and G is the gas gain.

According to the information given in 3.4.1 the quantity $\bar{n}_e$ can be evaluated in the

[6] for the CSC it can be as high as 300 Hz/cm^2.

approximation that all background particles are photons; the photon energy can be assumed to be in the MeV range. In that case ionization due to photon interaction is similar to the ionization caused by a charged particle: in $Ar : CO_2$ (93:7) at 3 bar the number of primary electrons produced per unit length is $\Delta n/\Delta x \sim 300\, p.e./cm$ (par. 3.2.1). Hence the average number of primary electrons released is proportional to the average distance travelled in the tube by the ionizing particle:

$$\bar{n}_e = \frac{2\int_0^R \sqrt{R^2 - b^2}db}{R} \cdot \frac{\Delta n}{\Delta x} \sim 1000 \text{ electrons.} \tag{3.45}$$

In the above equation R is the tube radius and b is the track distance from the wire.

In 10 years of LHC operation ($\Delta T = 10^8\, s$), with a background counting rate of 500 Hz/cm^2 (par. 3.4.1),

$$Q = 500\frac{Hz}{cm^2} \cdot 3\, cm \cdot G \cdot 1000\, e \cdot 10^8\, s = G \cdot 2.4 \cdot 10^5 \frac{C}{cm}.$$

(3.46)

Operating the chamber at a gain of $2 \cdot 10^4$ the accumulate charge in 10 years will be about 0.5 C/cm.

Therefore from the knowledge of the tube aging, which depends on the gas and on the operating conditions, with respect to the accumulated charge is possible to derive the expected lifetime of the detector for a fixed gain (Ch. 7).

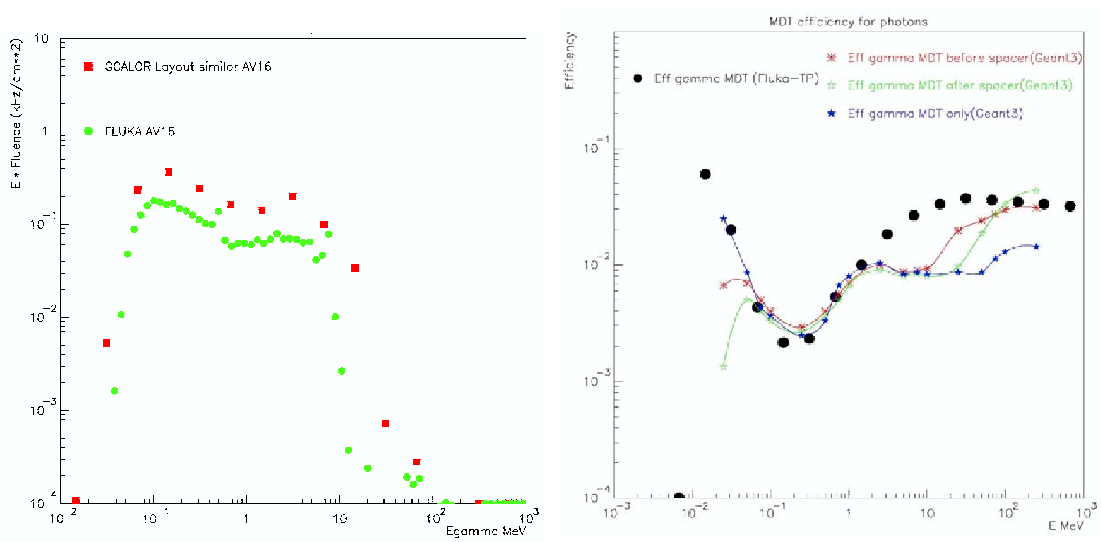

(a) (b)

Figure 3.21: (a) Photon flux as predicted by FLUKA and GCALOR Monte Carlo (nominal luminosity). (b) MDT efficiency for photons. The efficiency below 100 keV is due to photo-electric effetc in the gas while the rising around 1 MeV is due to the Compton scattering in the tube wall (par. 3.2.1).

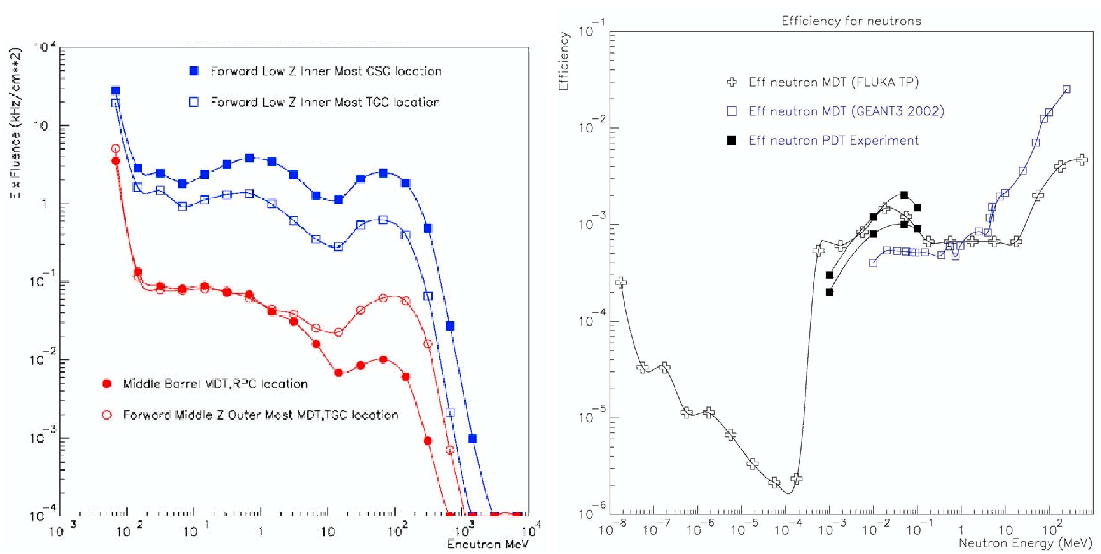

(a) (b)

Figure 3.22: (a) Neutron flux in the various region of the muon spectrometer as predicted by GCALOR Monte Carlo. All neutrons with energy below 10 keV are collapsed in the single bin (nominal luminosity). (b) MDT efficiency for neutrons. The rise around 1 keV (detection threshold) is due to the recoil of gas nuclei(par. 3.2.1).

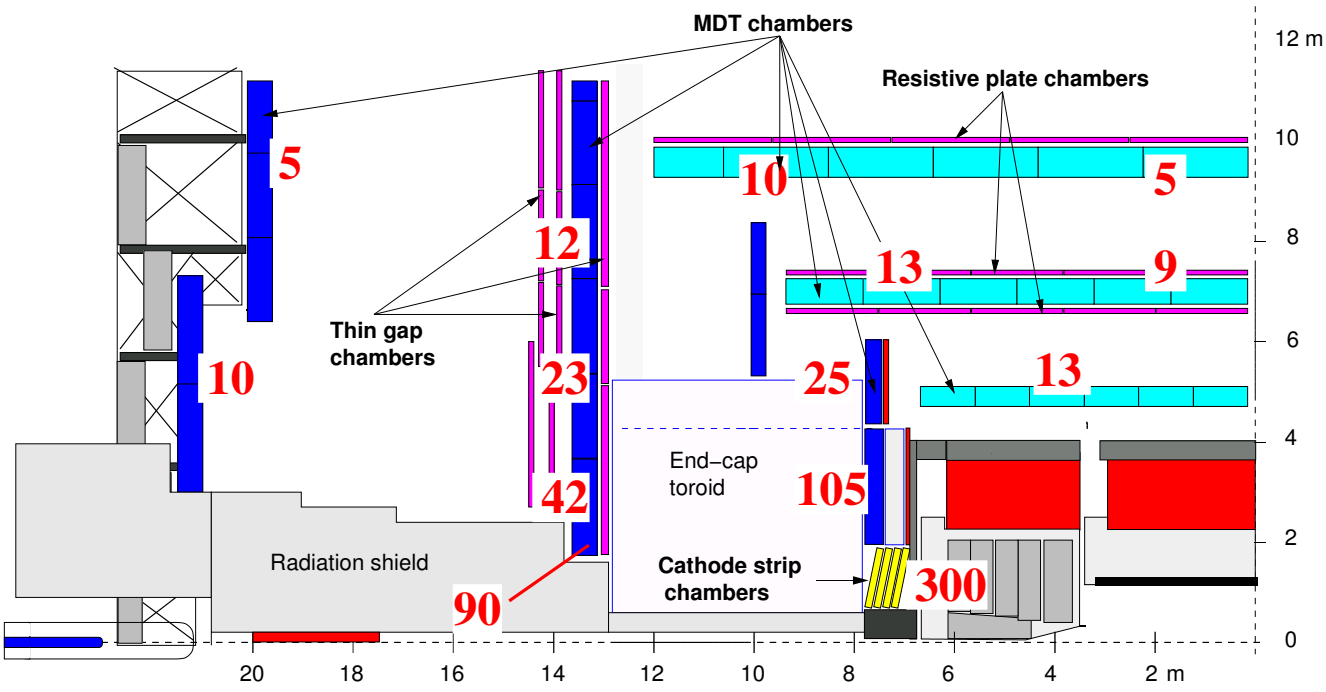

Figure 3.23: Background count rate (Hz/cm^2) in the precision chambers of the muon spectrometer at the nominal luminosity.

Chapter 4

Experimental setups, datasets and tools

Different experimental setups and datasets have been used for the studies presented in this work. In the present chapter the MDT test stand built in the Roma Tre laboratory and the CERN SPS test beam stand are described. The main differences between the two setups, that is to say the experimental probe (cosmic rays versus energetic monochromatic muons/pions) and the trigger devices, make them suitable environments for analysis concerning the calibration an the resolution of the MDTs. An introduction to the analysis procedures and software tools used and developed for the analysis is also given.

Another dedicated setup, developed for purposes of ageing studies, is described in the chapter 7.

4.1 Roma Tre MDT test site

The construction, assembly and test of a significant fraction of all the the MDT chambers (namely BIL and BML) of the ATLAS experiment has been committed to the INFN institute. Half of the MDT BIL chambers (62 in number) have been host in Roma Tre site ([47]) for the last part of the assembly and for the final control. In fact, each chamber, to be installed in the experiment, has to fulfill specific requirements in terms of mechanical precision, gas tightness, electrical stability, noise level and uniformity of response. In the Roma Tre test site they are equipped with the gas distribution system, the high voltage distribution and the on-chamber front end electronics. Then they undergo the Quality Assurance Quality Control ($QAQC$), a set of well defined tests conceived to monitor the detector functionality (more details in [47, 44]).

The test stand consists mainly of a gas distribution system, a high voltage distribution system and a trigger hodoscope. The gas system guarantees a high stability of the operating conditions as well as the monitor of the pressure, temperature, composition and flux of the gas.

MDTs are operated with Ar:CO_2 (93:7) at 3 bar absolute pressure.

In the next sections, the read out electronics and the trigger, which are relevant for the presented work, are described in more detail.

4.1.1 Read-out electronics and DAQ

The read-out system used consists of 24-channel mezzanine boards, containing the Amplifier-Shaper-Discriminator (ASD) chip and the AMT-1 TDC chip, connected to the VME Chamber Service Module CSM0 [33] that performs AMT and ASD initialization and read-out. Between the CSM0 (which can serve up to 18 boards) and the mezzanines there is an adapter [34] that provides the boards with the proper low voltage power supply and rearrange the signals to and from the CSM0. The scheme of the setup is shown in figure 4.1. In the final configuration, instead, the CSM is a board mounted directly on the chamber (see 3.3.2, fig. 3.15).

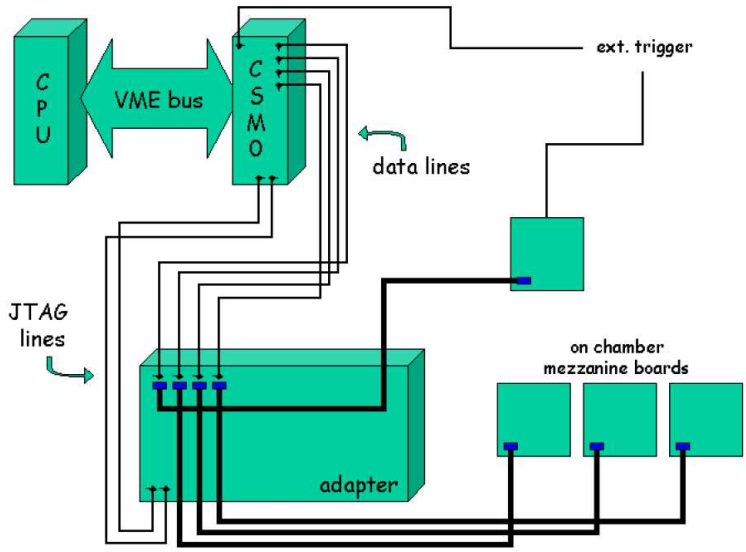

Figure 4.1: Hardware setup of the read-out electronics.

Each mezzanine board is connected to the adapter which in turn is linked to the CSM0 trough several RJ45 cables; there is an RJ45 cable for each mezzanine for the DS-link data connection and 2 Ethernet cables, the JTAG lines, for the initialization protocol (described below) transmission.

Three different steps are required to read-out the mezzanine boards with the CSM0:

1. CSM0 initialization
2. Configuration of TDC and ASD on the mezzanine board
3. Data read-out

After the reset of the CSM board a series of instructions to set the parameters needed for the system operation (as the JTAG transmission rate) are set and serial operations are enabled.

The mezzanine board is programmed using a serial bus with a JTAG protocol. The bus is accessed via VME. A setup string, the JTAG string, containing all the required parameters [28] is loaded from an external ASCII file and is sent to the mezzanine boards. The first parameter (first 8 bit of the string) provides the setting for the DAC which controls the ASD threshold value; this value can be varied from -254 mV to 256 mV in steps of 2 mV: for example, the value 108 corresponds to a threshold of -254+108×2=-38 mV. The ADC integration gate can be chosen between 8 and 45 ns in step of 2.5 ns. The default value is 15 ns. The default discharge (run down) current value is 4.5 μA and can range from 2.4 μA to 7.3 μA in steps of 0.7 μA. Other programmable parameters control the TDC time measurement. The meaning of these parameters is explained in figure 4.2.

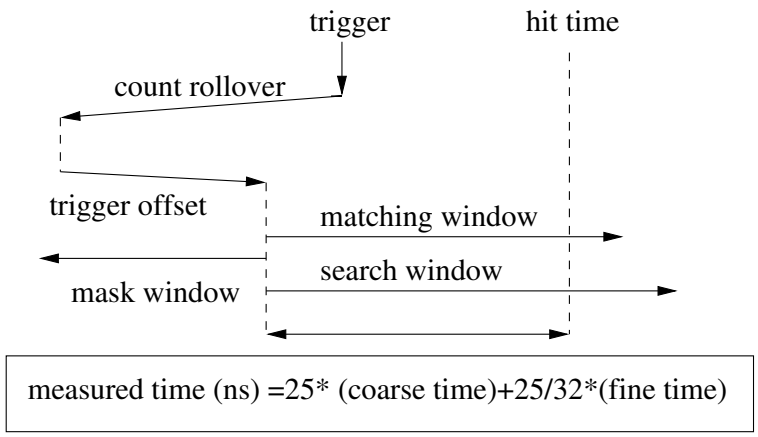

Figure 4.2: Definition for the time measurements parameters.

The *match window* defines the time interval in which hits are considered to match the trigger while the *search window* controls the window in which hits are measured. The *count rollover* and the *trigger offset* parameters fix the starting point of the various time windows with respect to the trigger signal. The *mask window* defines a time window before the trigger time where to look for hits that may have obscured hits in the matching window. All these parameters are given in course time counts (25 ns). The behaviour of the TDC must also be programmed by choosing to measure the time on the *leading edge*, on the *trailing edge* or to measure the width of the signal (*time over threshold*). The default choice is to measure the leading edge of the signal.

Once the configuration has been performed, incoming triggers are enabled and data collection can start.

The CSM0 receives a signal from an external trigger device and distributes it to the TDC in an asynchronous way (on the first falling edge of the internal clock of the CSM following the trigger signal). Having no information on the internal clock (which in the experiment will be related to the machine timing) it is necessary to measure the time between the trigger and the clock edge sending the same trigger signal in a channel of a TDC connected to the same CSM0. The number of words in the event

AMT parameters (μs) and settings	
matching window	1.575
search window	1.6
mask window	0.5
count rollover	102
trigger offset	100
Time Measurement	Leading Edge

ADC parameters	
integration gate	15 ns
threshold	-38 mV
run down current	10 μA

has to be retrieved from the proper register and then the data registers can be read. Data are stored in the event raw data file and then analyzed with dedicated software tools as described in the following.

4.1.2 Trigger

Two cosmic ray hodoscopes are available as trigger device for the MDT chambers.

The RPC hodoscope

This hodoscope [31] has been built for the test and certification of the BIL chambers.

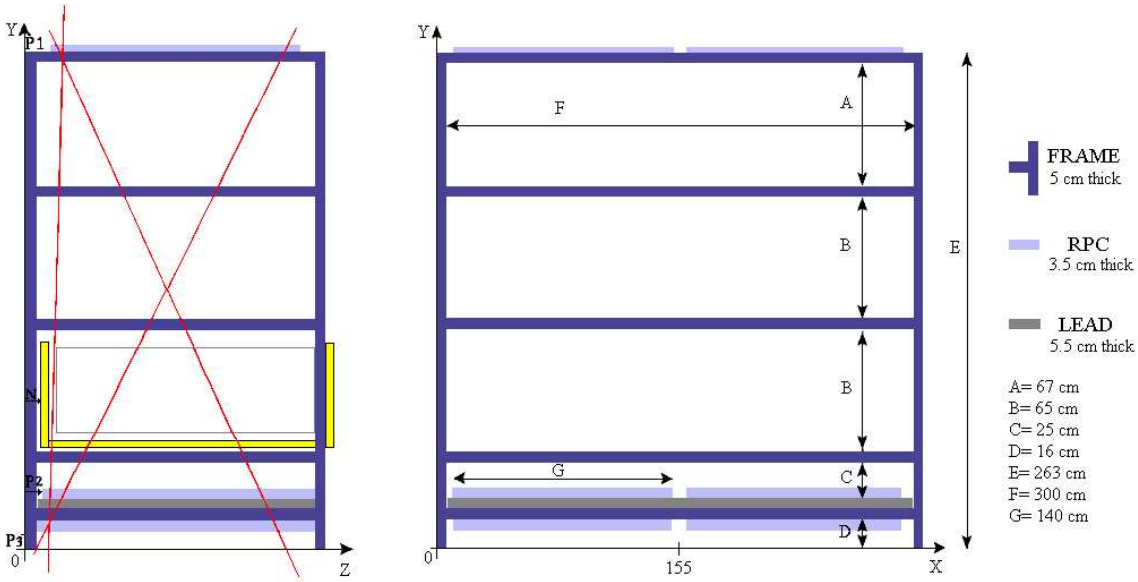

Figure 4.3: Scheme of the hodoscope.

The hodoscope provides an almost uniform illumination of the whole BIL chamber

surface and allows the simultaneous operation of three chambers. Three planes of RPC measure the coordinate along the drift tubes and provide a fast trigger with a time resolution of about 1 ns. The distance between the lower two planes is 12 cm and they are separated by 5.5 cm of lead to stop particles with energy lower than about 120 MeV. The third plane is at a distance of 2.4 m from the top lower plane. Three MDT chambers can be inserted in the hodoscope and positioned at three different heights. Reference marks insure positioning of the chambers with an accuracy of 0.1 mm. A scheme of the layout is shown in figure 4.3.

Each RPC covers a surface of 48×124 cm^2. Six RPCs for each plane, for a total trigger surface of 288×124 cm^2 as shown in fig. 4.4. are necessary to cover the whole length of the chamber.

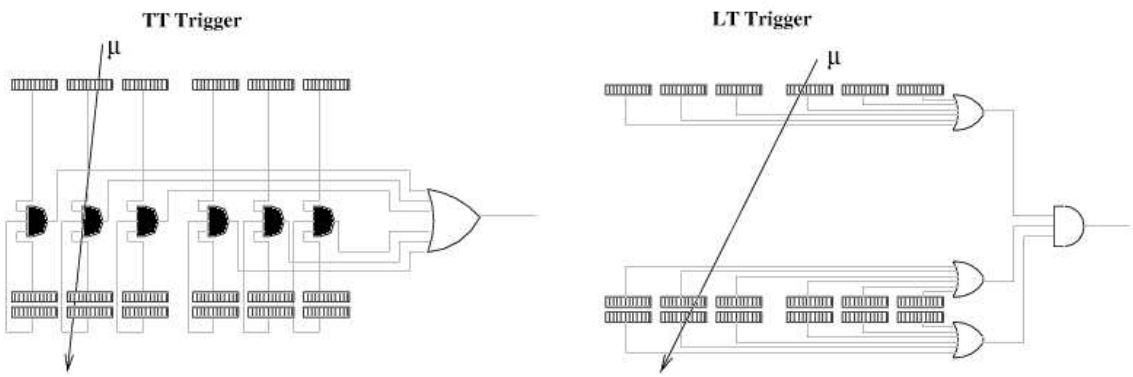

Figure 4.4: The two trigger logics implemented starting from the 18 fast-OR signals.

The electrodes of the RPCs are segmented in strips normal to the drift tubes of 2.9 cm pitch. One end of the strips is connected to the electronics board which receives the signals from 16 adjacent strips; each plane is divided in 6 read out slices. It contains the amplifiers and discriminators and the logic to form a fast-OR signal which is split and sent to a TDC and to the trigger logic to form the global trigger.

Two different trigger logics (see figure 4.4) have been implemented starting from the 18 fast-OR signals. A large acceptance trigger (LT), made with the coincidences of the three planes, selects an aperture of about ±40° around the vertical in the plane parallel to the wires. A tight acceptance trigger TT, made with the OR of the six threefold coincidences, defines vertical sectors with aperture of about ±12°. The LT rate is about 80 Hz and the TT rate is about 15 Hz.

The scintillator hodoscope

A system of four scintillator bars has been built to be used as an altenative trigger device for the data taking with the MDT chambers. The scintillator type is UPS89, based on Polystirene. Each bar covers a surface of 120 × 20 cm^2 and is read out at

both ends by two photomultiplier tubes (PMT)[1]. The scintillators thickness is 1 cm.

A possible trigger layout, made up of two trigger planes, is drawn in fig. 4.5.

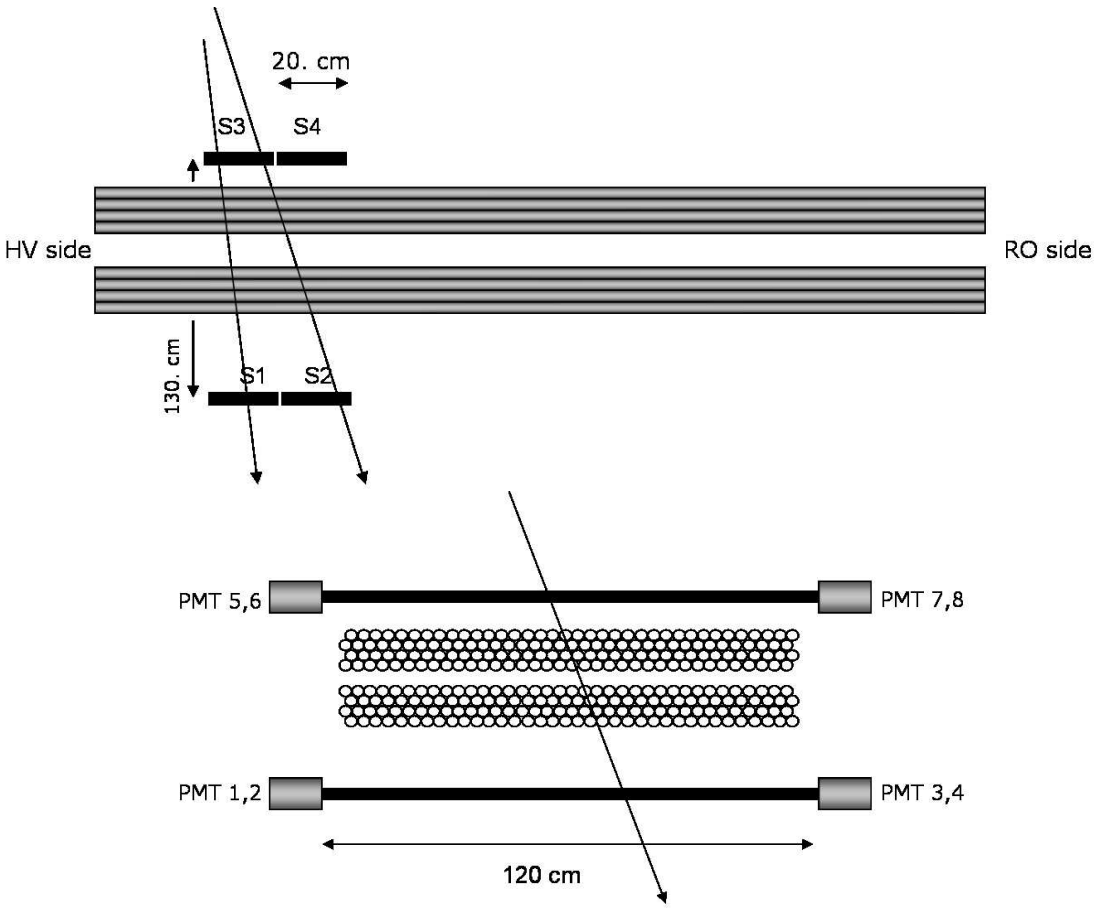

Figure 4.5: An example of a scintillator hodoscope layout.

The trigger logic used is:

$$(S_1\, OR\, S_2)\, AND\, (S_3\, OR\, S_4)$$

where S_i is the signal originated by the coincidence of two PMTs of the same scintillator number i (i.e. PMT 1 and 3, PMT 6 and 8 and so on) (fig. 4.5). Since the trigger time is provided by the last PMT signal which arrives at the coincidence unit the two lower PMTs (numbered as 1 and 2) are delayed in time by an equal arbitrary quantity in order to avoid event-by-event unknown fluctuations of the trigger time itself and the consequent uncertainty on the hit time measurement.

In this configuration the trigger rate measured is of about 10 Hz.

The scintillators are movable and can be placed along the tubes at different positions.

[1]Model Photonis XP2262

The relative distance between the planes and the trigger logic (i.e.: $S_1\, AND\, S_3$) can be chosen so that to vary the geometrical acceptance of the hodoscope as needed. This can be exploited to select muons traversing the chamber in a restricted range along the wire direction.

The RPC trigger plane is segmented as well in that direction (fig. 4.4), nevertheless each sector is longer compared to a single scintillator slab, moreover a uniform response between sectors is not garanteed because of delays due to differences in the electronics equipment (i.e. cables connections) and response.

4.2 Test Beam Setup

An extensive set of tests of the ATLAS Muon Spectrometer has been performed at the H8 beam line at the CERN SPS accelerator. The beam is made up of either muons or pions with energies from 20 GeV to 350 GeV. The main aim of the test is to allow a carefully study of the MDT drift properties and a better understanding of the calibration constants: definition and determination algorithms, study of the systematics effects and evaluation of their impact.

The entire Test Beam (TB) setup is made up of several modules of the ATLAS Muon chambers, the hadron TILE calorimeter and the electromagnetic Liquid Argon Calorimeter.

A schematic top view of the experimental layout for the muon chambers is drawn in fig. 4.6.

The H8 Muon stand reproduces an ATLAS slice of the barrel and a sector of the endcap, fully instrumented with the front-end electronics and equipped with the alignment system.

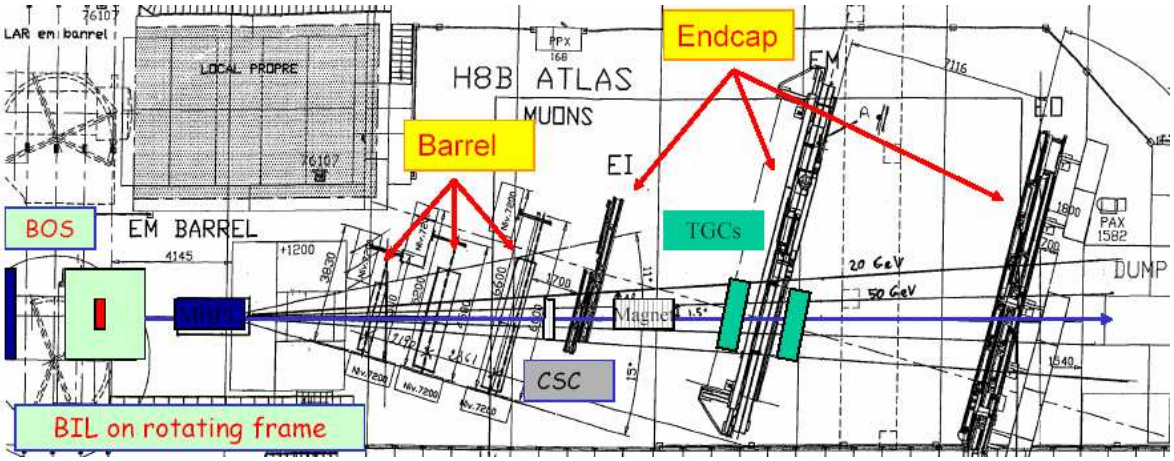

Figure 4.6: Schematic view of the muon chambers setup in the H8 area. MDT tubes are perpendicular to the plane of the figure. The beam axis is parallel to the plane of the figure.

The barrel-like stand consists of six MDT chambers[2], two for each type:

2 inner (BIL),

2 middle (BML),

2 outer (BOL).

An additional BIL chamber, named

$BILrot$,

is placed on a rotating support. The support can be operated remotely and a rotation up to $\pm 15^o$ around the chamber axis (parallel to the wire direction) is possible. Some sample were taken while keeping the chamber in rotation in order to enlarge the range of the track incidence angle.

A magnet was also installed bewtween the $BILrot$ and the barrel stand and used to bend the beam on the horizontal plane (orthogonal to the MDT wires).

4.2.1 Electronics

All the chambers are equipped with the Read Out electronics that will be used in the ATLAS detector. Therefore the CSM is an on chamber board which receives the trigger and the 40 MHz clock from the Time Trigger Control system (TTC) via optical link. It collects the the data from all the mezzanines and send them via optical link to two prototypes of the Muon Read Out Derive (MROD) which are VME board controlled by the ATLAS DAQ system. An addional mezzanine board was used to encode the time of the trigger signal since this is not synchronous to the CSM clock. The front end electronis is initialized trough a JTAG bit string.

4.2.2 Trigger

Two types of trigger have been used. The first is a coincidence of two scintillators covering an area of about 10×10 cm^2 (the 10×10 trigger) to select the core of the beam. In the second, the trigger signal is the coincidence of two larger scintillator planes covering an area of about 60×100 cm^2 and the veto of the 10×10 trigger (the *hodoscope* trigger). In this way, muons in the beam halo, covering a larger fraction of the muon setup, can be selected.

[2]In the end-cap stand there are six MDTs as well: two inner (EI), two middle (EM) and two outer (EO). Three TGC units (one triplet and two doublets) are also present. A CSC chamber has been installed later between the barrel and the end-cap stand and integrated in the data taking. These type of chambers have not been used for the presented studies.

4.2.3 Data Samples

The data used were taken with the chambers operated in the nominal ATLAS conditions: Ar:CO_2 (93:7) gas mixture at 3 bar absolute pressure, high voltage at 3080 V. Three different dicriminator thresholds have been used: 36 mV, 40 mV and 44 mV. Runs when the rotating BIL chamber was rotating have been selected for the present analysis; the energy of the beam particles was greater then 100 GeV. These samples are suitable for the space-time relation calculation. In the runs taken with the 10×10 trigger the beam spot illumintes 2-3 tubes. The temperature of each chambers has been measured in different positions and at regular time intervals.

4.3 From data decoding to track fit

In the analysis of MDT data, a series of operations have to be performed to reconstruct tracks from the read-out data. For each triggered event the data file contains the list of the hits of event itself. A hit is indetified by

- a tube identifier,
- the TDC measurement associated to the tube (*raw time*),
- ADC measurement (*raw charge*).

In the standard procedure the main operations are:

t_0 determination

The t_0 is the drift time associated to a particle crossing a given tube at a distance $r = 0$ from the wire. This value has to be measured for each tube and subtracted to the raw time measurement in order to have the correct drift time ossociated to the hit. This drift time can be converted into a drift radius assuming an $r(t)$ relation.

pattern recognition and track fit

Track reconstruction requires the selection of the hits that can be associated to form a track (*pattern recognition*) and the fit with a line tangent to the *drift circles* (circles centered on the wire with radius equal to the drift radius).

autocalibration

The actual $r(t)$ of an MDT is not know *a priori*. It depends on several parameters (such as gas composition, density, electronic threshold, cfr. Ch.3) and therefore must be derived time by time to fully exploit the precision of the drift tubes. The determination of the $r(t)$ relation requires a dedicated analysis; it is done using data from the chamber with an iterative procedure (*autocalibration*) which allows to find the correct

$r(t)$ relation.

The analysis presented in this work has been performed using the CALIB program [35]. CALIB is a package (developed in Roma Tre and Roma "La Sapienza") for the analysis of MDT data and in particular for the autocalibration of the chambers and for the evaluation of the resolution and of the efficiency. As will be shown in the next chapters, CALIB has been used successfully in various setup like the H8 test beam, the Roma Tre cosmic test site and also on simulated data.

A complete description of the CALIB package, sub-packages, of the data files needed, of the datacards and of the procedures for installing, compiling and running the program are provided in [35]. In the next two sections the data decoding and the track finding task are described while the t_0 determination, autocalibration and other specific algorithms are treated in the next chapters.

4.3.1 Data decoding and geometry handling

In the various setups the data acquisition system is different. For each data format, a different data decoding has been implemented; anyway the bulk of the decoding is the association of a hit (time measurement and sampled charge for a given electronic channel) to a tube of the chamber. This association depends on the electronics and on the chamber type. A description of the inner structure of the chambers (in terms of number of tubes, tube length, distances between multilayer) and of their relative positions is required for a correct positioning in space of the tube. Two different geometry description systems are available in the software package.

One is based on dedicated text files (GeoFile) which contain all the relevant informations; this is useful when dealing with few chambers and allows a fine tuning of the parameters (for example to easily take into account tomograph measurements of the chambers).

The other system is based on the AMDB detector description [36] and is used when the setup becomes more complicated (like the H8 setup or for data simulated in the whole spectrometer).

Once a data entry has been fully decoded a new hit is added to a list which will contain all the hits of the event.

4.3.2 Pattern recognition and track fit

The pattern recognition is a procedure to find the tracks associated to a given hit list.

As outlined in Ch. 2, an MDT chamber is made of two multilayers of 3 or 4 layers of

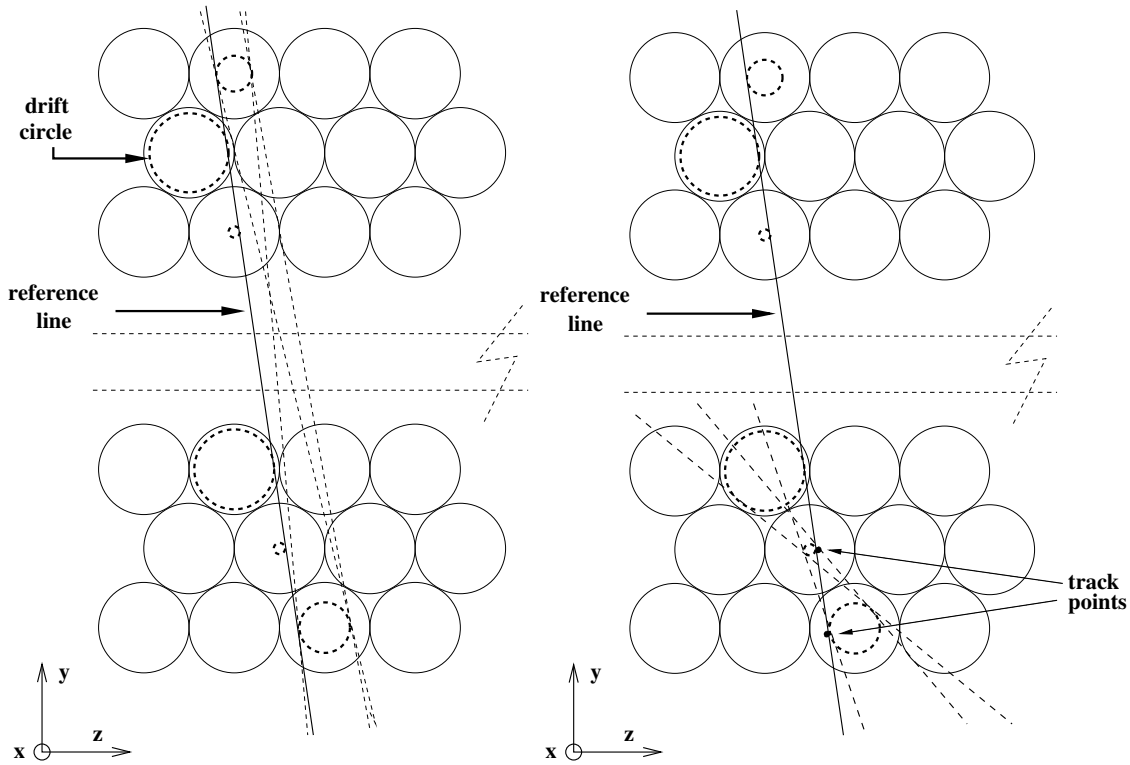

(a) Definition of the reference line (b) Definition of the first two track points

Figure 4.7: Description of the track element calculation. An example of a fit to the hits within two multilayers of three layers is given.

tubes that are fixed on an aluminum structure (*spacer*). The pattern recognition and track fit procedure can be applied to a chamber or to the two multilayers separately; this depends on the requirements of the application and will be discussed in the following.

Pattern recognition is performed in two steps.

- At initialization, a list of reference patterns, the *Candidate Tracks*, are created taking tubes that are aligned in a given angular range (which is programmable by the user). A comparison (at tube level with no use of drift information to speed up the procedure) between tubes in an event and the *Candidate Tracks* is made to quickly understand which hits can be associated to the same track.

- Once hits have been selected, a fit to the drift circles, the *track fit* (described below), is done and the track is accepted or rejected on the basis of a χ^2 test. If the track is not accepted, the hit which gives the higher contribution to the χ^2 can be removed from the list and the fit is done again. The maximum number of hits that can be removed is user-defined as well. When the track is accepted, the two parameters of the line, their errors, the χ^2 of the fit and the pointers to the hits used are registered and are available for later use. The centers of the tubes

are given in a global reference system (taking into account the position of the chamber). The global system is chosen to have the y and the z axis on the drift plane and the x axis along the tubes.

Once n tubes within a chamber (the same applies considering one multilayer) have been associated to a *Candidate Track*, the procedure applied to determine the parameters of the track (track fit) is the following:

- The four possible tangents to the first and last drift circles are computed.
- Among these straight lines, the one having the smallest χ^2 with respect to the other drift circles is chosen as the *reference line* (see figure 4.7(a)).
- Then, for any pair of adjacent tubes other four tangents are computed and the tangent points closest to the reference line are used as *track points* (figure 4.7(b)).
- To each *track point* is assigned an error defined by the tube resolution function and the parameters of the final track are obtained fitting the *track points*.

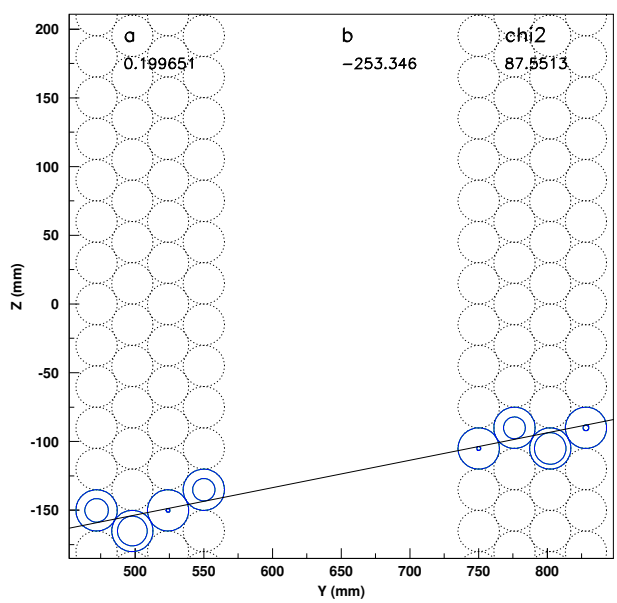

Figure 4.8: A track reconstructed with a BIL chamber. The parameters of the fitted function $z = a \cdot y + b$ and the χ^2 of the fit are also reported.

In the event display of figure 4.8 is shown an example of a track reconstructed in a BIL chamber.

4.4 GARFIELD simulation program

The GARFIELD Monte Carlo program represents the most accurate simulation of the physics processes and the electronics which characterize the behaviour of a drift detector.

Actually it is made up of three packages: HEED[38], MAGBOLTZ[39] and GARFIELD[37] itself.

The HEED program computes th energy loss of fast charged particles in gases, tacking, optionally, delta electrons and multiple scattering into account. The program can also simulate absorption of photons in the gas through photo-ionization.

The MAGBOLTZ program, computes electron transport parameters, for example the mobility and the Townsend and the diffusion coefficients (Ch. 3), for a large variety of gases and mixture of gases. The program is based on the numerical solution of the Boltzmann transport equation. The principals initialization parameters are the gas composition, temperature, pressure and the electric(magnetic) field range.

GARFIELD is a program for the simulation of two and three dimensional drift chambers. It is interfaced to HEED and MAGBOLTZ and computes field maps, electron and ion drift lines, drift time maps and arrival time distribution, signal induced on the wires by drifting electrons and ions and the electronics response.

Examples of simulations performed with GARFIELD are given in plots shown throughout Ch. 3.

4.5 A Monte Carlo for MDT tracking studies

A Monte Carlo simulation program has been developed with the purpose of a systematic and accurate study of the calibration and tracking with an MDT chamber.

Originally the program has been written to study the impact on the resolution of

- multiple scattering in the tubes wall
- trigger induced time jitter

and for

- reconstruction algorithm validation

- miscalibration studies.

It has also been conceived to exploit the accuracy of the GARFIELD simulator and to allow for a direct comparison of the results with the experimental data.

In fact, it can be optionally interfaced with both the GARFIELD program and the CALIB package.

The simulation chain can be outlined as follows:

1 Particle generation. The traversing particle can be generated according to an arbitrary momentum and angular distribution function.

For comparison with the Roma Tre test site measurements, a simulation of the momentum and angular distribution of the cosmic rays has been implemented (Ch. 6).

2 Trigger acceptance check. For computing time economy, by default, the production vertex of the particle is distributed (i.e. uniformly) on the trigger surface which is upstream with respect to the detector. Then particles which are not in the trigger geometrical acceptance are rejected.

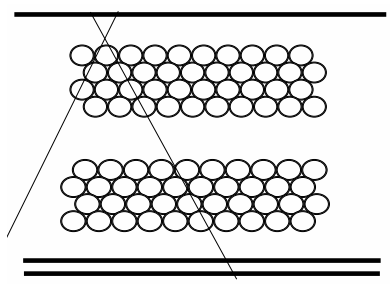

3 Transport. The accepted particle is then transported through the chamber volume. This means that, for each tube encoutered, the deflection of the trajectory due to multiple scattering in the tube wall is calculated. When the particle is inside the tube volume the *impact parameter*, that is the distance with respect to the wire (the tube center), is calculated and stored. This is done for each traversed tube until the particle exits the chamber volume. At this level a list of the crossed tubes and the associated impact

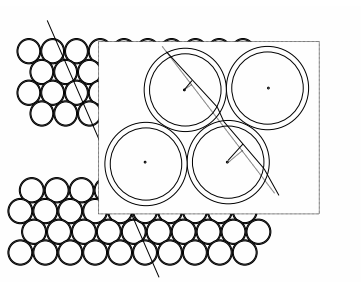

parameters is available.

4 Hit generation. Once the impact parameter is determined it must be converted into a drift time. Two options:

a GARFIELD is invoked for the drift time calculation. In this way the intrinsic time resolution of the drift tube is automatically taken into account.

b the radius is converted into a drift time interpolating a user defined $r(t)$ relation table. In this case a parametrization

$$f_{res} = f_{res}(r)$$

of the gas resolution f_{res} with respected to the radius r must be provided as well. Before the conversion, the impact parameter r_i is smeared according to the relation

$$r_i = r_i + \sigma_{gauss} \cdot f_{res}(r_i)$$

where σ_{gauss} is a random number distributed according to a Gaussian function with mean equal to zero and unitary standard deviation. By default, negative radii are changed into positive.

Optionally, the following effects can be simulated.

Trigger delay: each hit time calculated in one of the two ways described above is then augmented by a quantity corresponding to the time the signal takes to reach the read out electronics of the hodoscope. This time depends, on an event-by-event basis, on the impact point of the track on the downstrem trigger plane and on the signal propagation velocity (provided by the user).

Tube t_0: This option implies that a tube dependent time shift is added to the simulated hit times. A list of the t_0 value to be associated to each tube must be provided by the user.

Electronic noise: If this option is selected spurious (non physical) hits are added to the hit list. For each tube the probability to give a noise hit is calculated according to the desired noise level.

At this level a list of the crossed tubes and the associated times is available.

5 Event data production. These generated hits are then written in a format which is readable by the same data decoding and analysis programs, i.e. CALIB, used to process the experimental data.

Steps from 2 to 4 are described in detail in the next chapter.

Chapter 5

Autocalibration

5.1 The drift time spectrum

Drift tubes are used for drift time measurements: the time interval between the passage of the particle in a tube and the time the induced signal cross the threshold of the discriminator (Ch. 3). What is actually measured is the *raw time*, t_m:

$$t_m = t_{part} + t_{drift} + t_{delay} - t_{trig} \tag{5.1}$$

Where t_{part} is the time the particle hit the tube, $t_{delay} = t_{wire} + t_{ele}$ is the propagation time of the tube signal; it sums up the propagation time along the anode wire (t_{wire}) and the delay (t_{delay}) due to the read-out electronics. The trigger time $t_{trig} = t_{part} + t_{flight} + t_{trig,prop} + t_{mezz} + t_{trig,ele}$ is the time at which the trigger gives the start pulse to the TDC connected to the tube. It is the sum of several contributions. The time of flight (t_{flight}) of the particle from the tube to the trigger plane; $t_{trig,prop}$, that is the propagation time inside the trigger plane. The t_{mezz} is the difference between the trigger signal and the clock edge as explained in 4.1.1 and is measured by means of a dedicated mezzanine board while $t_{trig,ele}$ is the delay introduced by the trigger read-out electronics. Equation 5.1 can be written as:

$$t_m = t_0 + t_{drift} \tag{5.2}$$

The quantity t_0 is a constant of the tube (and varies from tube to tube). In fig. 5.1 is shown a typical distribution of the measured time t_m, usually called drift time distribution. Because of the behavior of the drift velocity which reaches its maximum value close to the anode wire and decreases for larger distances, the drift-time spectrum rises sharply at early times reaching a maximum, then drops continuously for later times. The spectrum ends with another less sharp edge

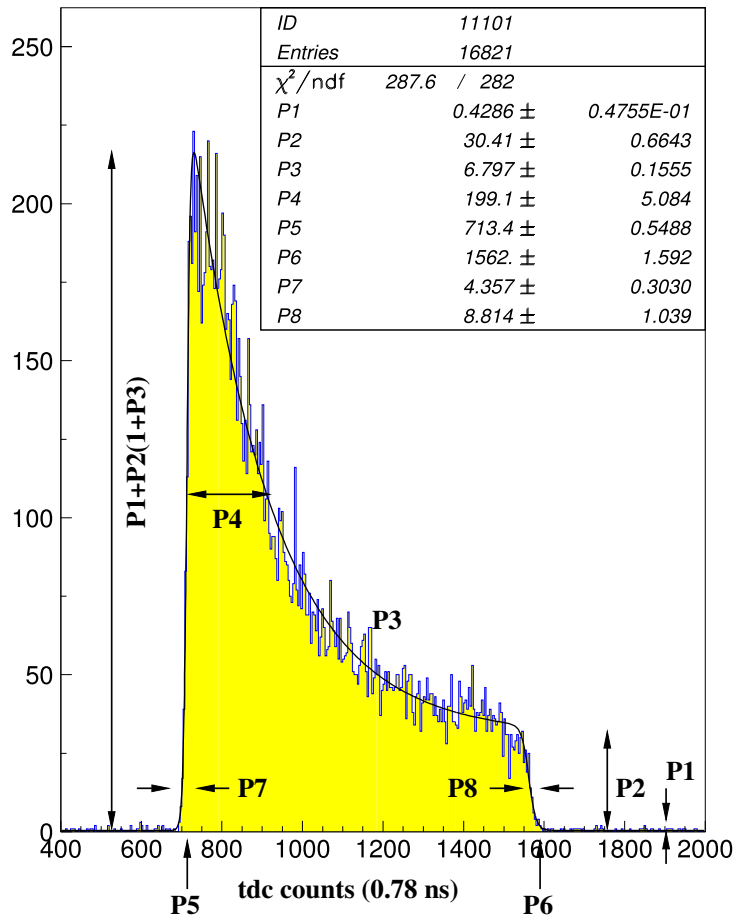

Figure 5.1: Typical drift time distribution at nominal operating conditions and the fitted function 5.3.

The distribution can be fitted with the empirical function:

$$f(t) = p_1 + \frac{p_2 \left(1 + p_3 e^{-\frac{t-p_5}{p_4}}\right)}{\left(1 + e^{\frac{-t+p_5}{p_7}}\right)\left(1 + e^{\frac{t-p_6}{p_8}}\right)}. \tag{5.3}$$

The parameter p_1 is the uncorrelated (flat) background, p_2, p_3 and p_4 describe the shape of the central portion of the distribution; p_5 and p_6 are the turning points of the rising and of the trailing edge respectively; p_7 and p_8 describe the rising and trailing edges time amplitude.

Muon hits contribute to the so-called *physical time window* of the distribution which is assumed to be comprised between p_5 and p_6 (indicated also as t_{max}).

5.1.1 t_0 determination

The t_0 in the 5.2 is usually measured by fitting the rising edge of the drift time spectrum.

Despite the value obtained by a fit procedure does not corresponds to the start of the physical drift window, all drift times are related to that value ($t_{drift} = t_m - t_0$), hence a systematic shift will be reabsorbed in the definition of the $r(t)$ relation. The aim of the tube t_0 determination is to syncronize the starting time of the disrtibution for all the MDT tubes. The t_0 can be defined as the parameter p_5

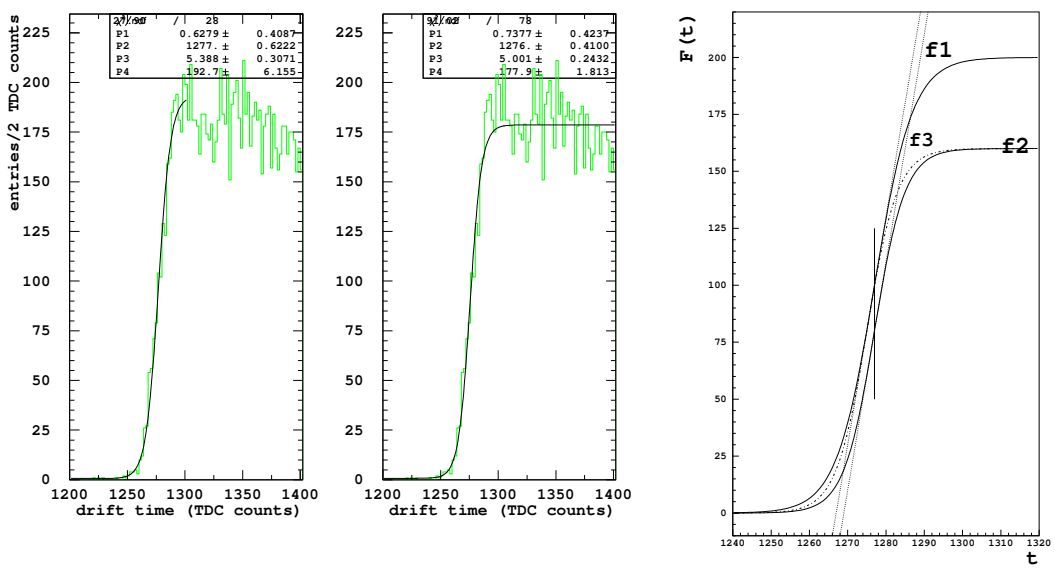

Figure 5.2: (*left and center*) Fit results for two different choices of the range. (*right*) Curves f_1 and f_2 have the same slope and t_0 but different A parameter (eq. 5.5). Curve f_3 concides with f_1 in the rising edge: has the same slope but different t_0 and A. Tangents to $t = t_0$ are also drawn.

of the 5.3. This parameter is strongly correlated to the others, in particular, it is influenced by the function used to fit the central part of the spectrum: there is a double peak at the maximum of the distribution (e.g. fig. 5.1) which is poorly parametrized by the exponential at the numerator of the 5.3. This makes p_5 sensitive, for example, to sample size variation.

Fitting only the rising portion of the distribution (using a part of the 5.3) with the Fermi-Dirac function

$$F(t) = p_1 + \frac{A}{1 + e^{-\frac{t-t_0}{T}}}, \tag{5.4}$$

the time range of the fit is not defined unabiguously. This introduce a bias in the determination of t_0, the turning point of the 5.4. Since maximum of the 5.4 is given mostly by the parameter A (assuming, for simplicity, $p_1 = 0$) its value may vary significantly with the range chosen for the fit. In the example shown in fig. 5.2(left) a value of 192 ± 6 if found, increasing the range to later times the fitted value for A is 177 ± 1 (center). The slope of the rising edge is proportional to A, in fact

$$\frac{dF}{dt}|_{t=t_0} = \frac{A}{4T} \tag{5.5}$$

hence if A varies by a factor, say k, the rise time parameter T will be varied by the same factor to keep the slope unchanged as for the curves f_1 and f_2 in fig. 5.2(right). Those have the same slope and the same t_0 but are shifted along the abscissa. To make the rising edge of f_2 to coincide to the rising edge of f_1 the t_0 of the former function must be shifted to earlier times: curve f_3. As can be derived from the parameters of the two fits reported in 5.2 the found slope is the same but the t_0s differ (by about one TDC count) as a consequence of the different plateau A. Quantitatively (see also fig. 5.2(right)): the tangent $s(t)$ to $F(t)$ at $t = t_0$ is

$$s(t) = \frac{A}{4T} \cdot (t - t_0) + \frac{A}{2} \tag{5.6}$$

and intersetcs the time axis at $t - t_0 = -2T$; if $A \to A' = kA$ and $T \to T' = kT$ $(k < 1)$ then 5.6 becames $s'(t) = A/4T \cdot (t - t_0) - kA/2$ which vanishes at $t - t_0 = -2kT$. Hence, the t_0 has to be shifted by the quantity $-2T(1 - k)$. Since a typical value for the lower limit of k is 0.9 and 6 TDC counts for T the consequent t_0 variation is of about 1 TDC count. The 5.6 suggests that the quantity

$$t_0 - 2T \tag{5.7}$$

is invariant with respect to the tranformation $A \to kA$:

$$t_0' - 2T' = t_0 - 2\ (1 - k)\ T - 2kT = t_0 - 2T. \tag{5.8}$$

Relation 5.7 can be used as the new definition of the tube t_0 if the estimated precision is needed.

Alternatively a more conservative procedure can be followed. A fit with the 5.3 is performed for a first t_0 and T estimation. Then the drift time distribution is fitted with the 5.4 between two times corresponding to the 5% and 95% of the rising edge, that is approximatively the range $[t_0 - 2T, t_0 + 2T]$.

5.1.2 Chamber response monitor. Noise

Parameters from the fit to a drift time distribution are useful for monitoring chamber response and performance. A typical hit tube distribution for a cos-

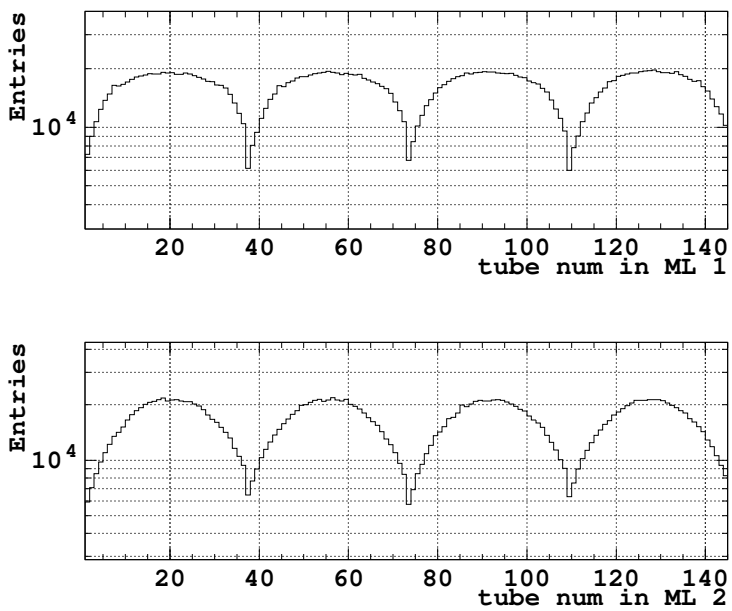

Figure 5.3: Tube hit distributuion on a sample of cosmic muon triggers.

mic muon trigger data sample 4.1 are shown in figure 5.3. The shape of the hit distribution is determined by the angular coverage of the RPC hodoscope. The uniformity of the distributon assures that no dead or extremely inefficient

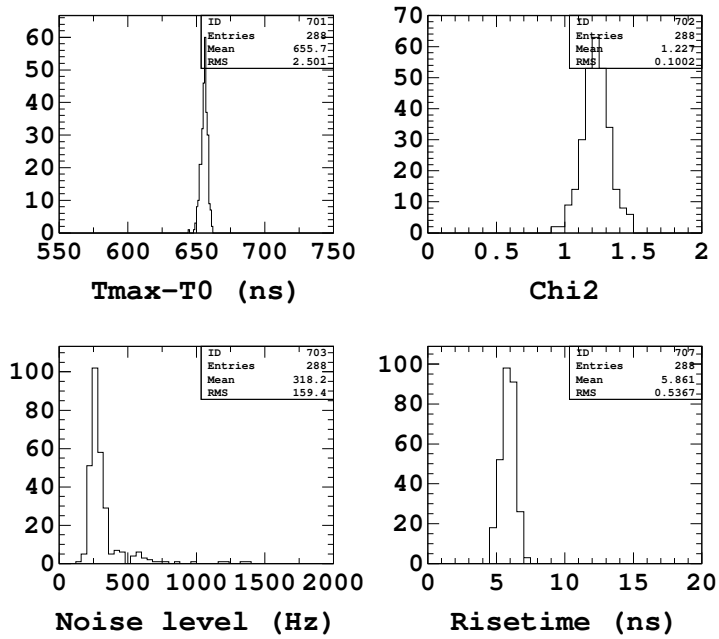

Figure 5.4: Distribution of fit parameter related quantities.

electronics channels are present. Distribution of the parameters p_7, of the fit χ^2

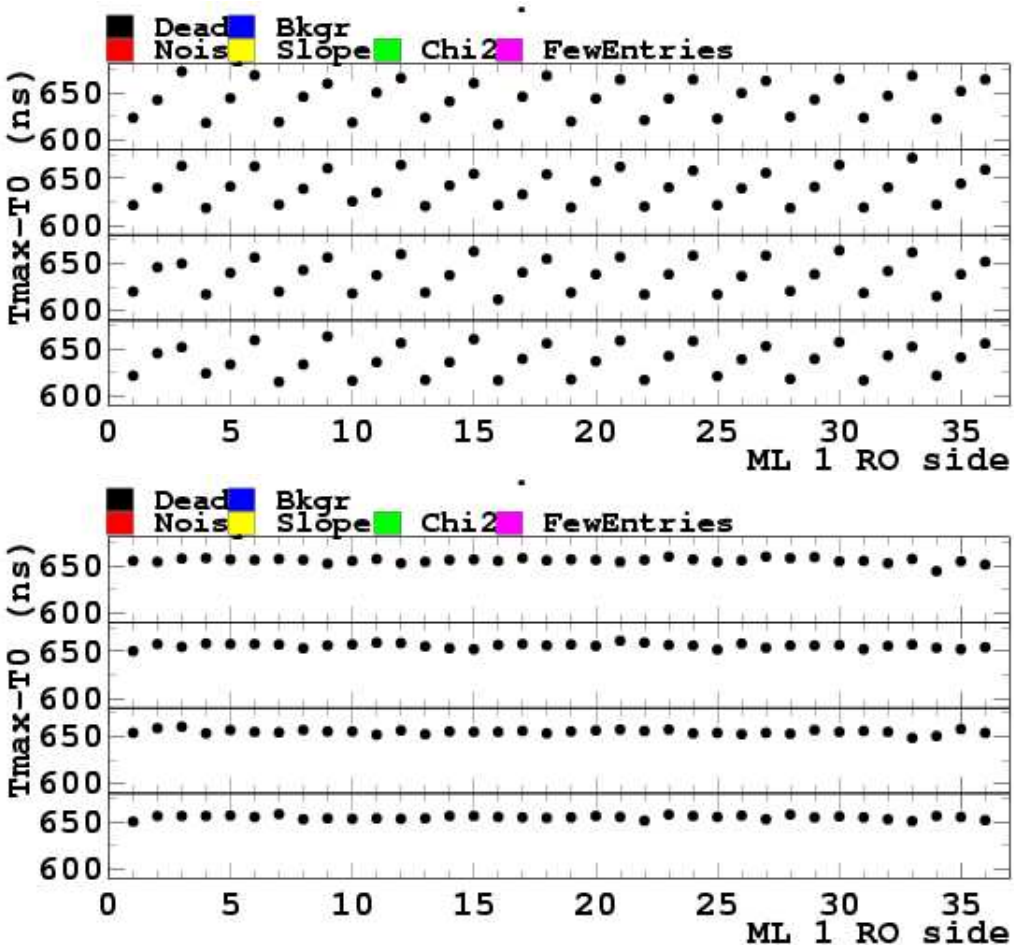

Figure 5.5: Maximum drift time distribution forn uneven (top) and even gas condition.

and $t_{max} - t_0$ (fig. 5.4) can reveal significant deviations from the reference mean values.

The maximum drift time $t_{max} - t_0$, in particular, is very sensitive to the gas properties: density (pressure and temperature) and composition. The tube $t_{max} - t_0$ distribution is shown in fig. 5.5 for two different cases. In the upper plot the distribution is not uniform and a "triplet" serial structure is visible. This behavior is due to the gas distribution system layout: groups of three tubes of the same layer are supplied in parallel and the gas flows serially whithin each group. This may lead, expecially at the beginning of the gas supply, to an uneven gas dendoty and composition inside the tubes belonging to the same group (lower density means higher drift velocity or shorter maximum drift time). The lower plot shows the same distribution once a uniform pressure whitin the chamber is reached. Gas leak or contamination can affect the $t_{max} - t_0$ distribution as well.

Noise

Entries outside the physical time window are due to uncorrelated hit from particle background in the experimetal hall or to electronic noise. The rate f_{random} of such random hits can be estimated as

$$f_{random} = \frac{n_{out}}{\Delta t_{out}} \frac{1}{N_{trig}} \tag{5.9}$$

where n_{out} is the number of entries outside the physical time window in the interval Δt_{out} and N_{trigg} is the number of triggers. Parameter p_1 in the 5.3 is related to the noise rate since $n_{out} = p_1 \times \Delta t_{out}/\Delta t_{bin}$ (Δt_{bin} is the bin width). Typical noise distribution is shown in fig. 5.4.

5.2 Autocalibration

As anticipated in 4.3, in order to fully exploit the accurate mechanical properties of the chambers and the good spatial resolution that can be achieved with the drift tubes, a precise knowledge of the $r(t)$ relation is needed. The $r(t)$ relation depends on the operation conditions as pressure, temperature and local value of the magnetic field; therefore it can be different for tubes in different regions of the spectrometer. It is mandatory to have a procedure to measure and monitor $r(t)$ relations for chambers installed in the experiment.

The autocalibration aims at finding the space-time relation using only data from a chamber.

The method is based on the assumption of straight line tracks.

The t_0 of each tube has to be known (see previous section) so the drift time of a given hit can be derived from 5.2.
The algorithm starts with an input $r(t)$ which is used to convert drift times to radius. For each event a fit to the line tangent to the drift circles is performed as described in 4.3.2. A track in the plane perpendicular to the wires can be written as

$$z = a \cdot y + b. \tag{5.10}$$

The reference system (z, y) can be deduced from the fig. 4.8. Once the track points are defined, the parameters a and b are calculated by minimizing

$$\chi^2 = \sum_{i=1}^{N} \left(\frac{|a \cdot y_i + b - z_i|}{\sqrt{1+a^2}} - r_i \right)^2 / \ \sigma_i^2 = \sum_{i=1}^{N} \frac{d_i^2}{\sigma_i^2}. \tag{5.11}$$

The sum runs over the hits belonging to the track. For each hit (y_i, z_i) are the coordinates of the wire, $r_i = r(t^i_{drift})$ is the drift radius calculated from the

known drift time and the assumed $r(t)$ relation. The term d_i, usually referred to as *residual*, is the distance between the track and the circle with radius r_i and center (y_i, z_i) as sketched in fig. 5.6. The residual distribution is then divided

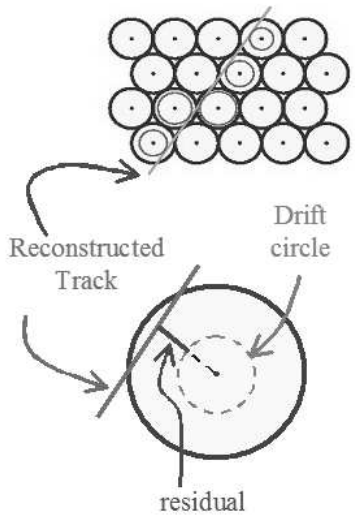

Figure 5.6: Residuals definition.

in time slices (usually 51 slices). The mean value of the residual distribution for each time slice is used to correct the initial $r(t)$ relation.

The procedure is iterated until the $r(t)$ relation reaches a prefixed accuracy (that has to be of the order of 10 μm) or requiring that the *i-th* iteration doesn't differ from the (*i*-1)-*th* one within errors. In general, at each iteration a χ^2 cut is imposed on the reconstructred tracks. A useful variable to describe the convergence is the quadratic average of the correction μ^j at a given iteration j:

$$\mu^j = \sqrt{\frac{\sum_{i=1}^{N} m_i^2}{N}} \tag{5.12}$$

where m_i is the $r(t)$ correction for the *i-th* slice at *j-th* iteration and N is the number of the slices.

5.3 Systematics

A sample of type *BILrot* (about $10^5 events$) taken at the Test Beam setup (par. 4.2) has been used for the following considerations.

In fig. 5.7(left) the residual distribution is shown as a function of the drift time. The larger spread for small drift times reflects the behaviour of the resolution

near the wire (next chapter). Fig. 5.7(right) shows the average of the residual distribution in the various time slices: these are the values of the correction to apply to the $r(t)$ relation. It can be seen that after about 10 iterations the correction is below 10 μm. For a given choice of the parameters of the autocalibration algorithm the minimum mumber of iterations needed depends on the initial $r(t)$ relation used.

The obtained $r(t)$ is shown in the bottom plot of 5.7.

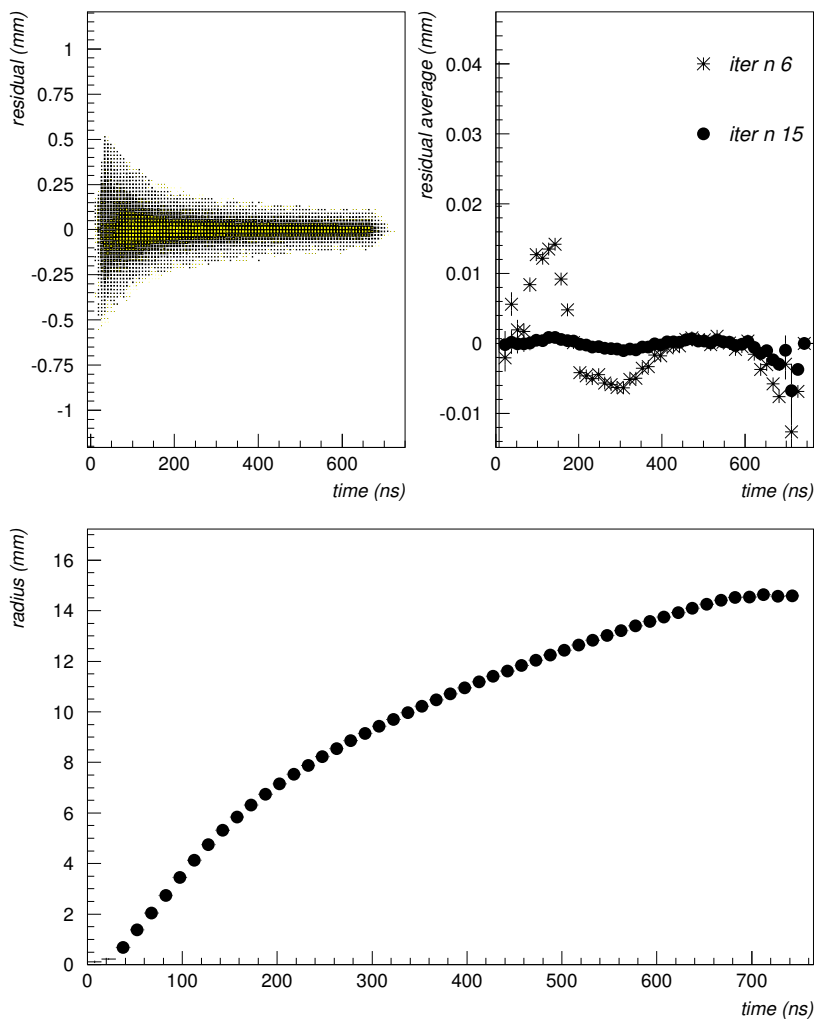

Figure 5.7: (top) Residual distribution (iteration 15) and average value versus time for two different number of iterations. (bottom) Calculated $r(t)$ relation.

In the following a study on the dependence of the $r(t)$ relation on:

- number of events processed,
- χ^2 selection,
- spatial resolution function,
- tube $t_0's$,
- track angular spread,

is summarized. The $r(t)$ relation obtained processing all the events ($\sim 10^5$) of

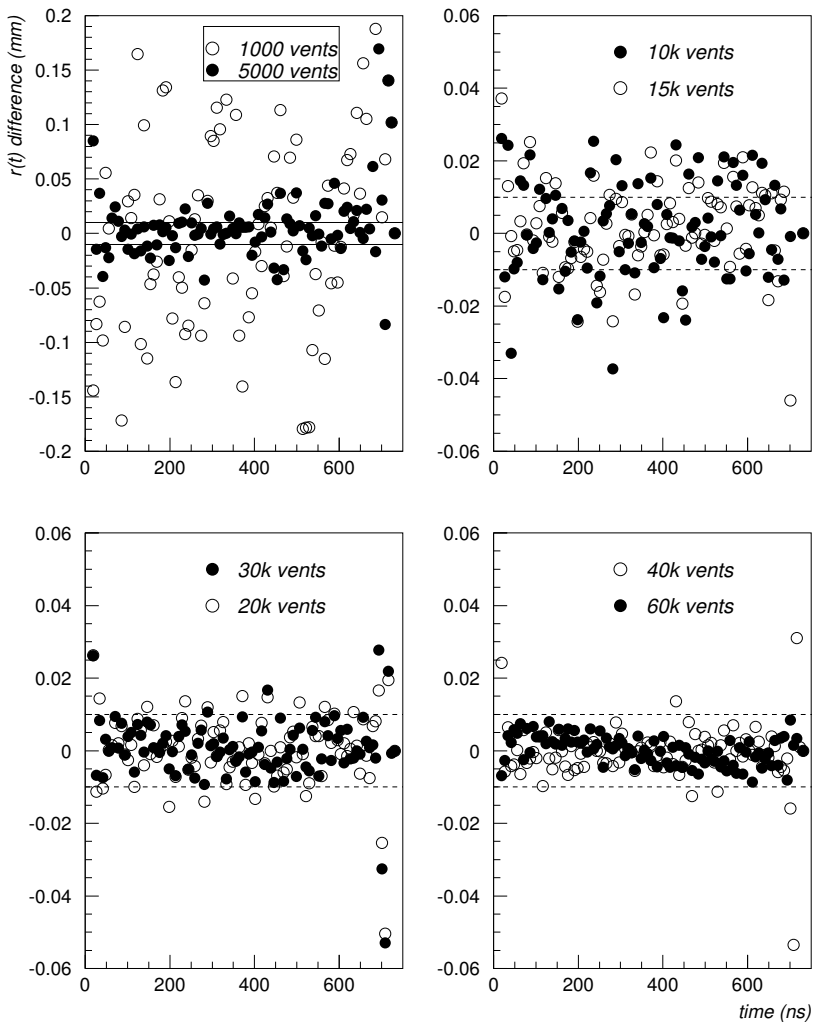

Figure 5.8: Space time relation differences with respect to the refence for different sample sizes. Dotted lines delimite the area where the difference is below $10\mu m$.

the indicated sample, accepting tracks with angular spread $a : [-0.3, +0.3]$ (corresponding to $[-15^o, 15^o]$, the maximum value allowed for the rotating BIL) and

using $t_0's$ determined by fitting only the rising portion of the drift time spectrum (as decribed a the and of the 5.1.1) is taken as refence. For all $r(t)'s$ (reference one included) the minim mumber if iteration is fixed by requiring a distribution of the average residual (i.e. the correction to be applied to the $r(t)$) is within $3\mu m$. This can be achieved by requiring the convergence 5.12 to be lower than 1 μm.

In what follows the events of a subsample are uniformly distributed over the

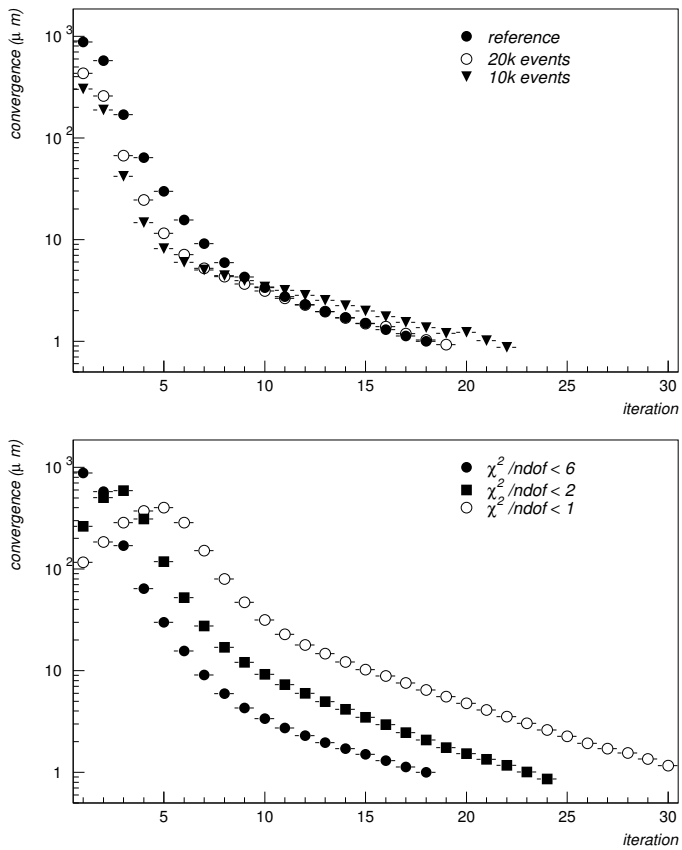

Figure 5.9: Convergence for different sample size and reduced χ^2 cuts.

whole sample of origin in order to avoid systematic effects related to possible variations of the operating conditions during the data taking.

In fig. 5.8 are shown the differences in the calculated radius for each time slice with respect to the reference $r(t)$ for different sizes of the processed sample. With $20 - 30 \times 10^3$ events differences are within 20 μm and within $10\mu m$ using at least 60×10^3 events. A higher number of events makes the convergence slightly faster

as shown in fig. 5.9. The choice of the χ^2 cut affects the convergence as well. A thighter cut slows down the convergence. Appling the same cut for all the iteration has turned out to be the most efficient choice. In the example of fig. 5.9 the cut on the reduced χ^2, $\chi^2/ndof < 6$ is a very loose cut, it rejects less then 1% of the events after the first iteration.
In general, at each iteration, the correction to be applied to a given radius (5.2) may be scaled by a factor α (which in the standard procedure is unitary). Convergence speed is very sensitive to this factor as shown in fig. 5.10. and reaches a minimum for $\alpha \sim 1.5$ where the number of iterations needed is almost half of the number nedeed in the case $\alpha = 1$.

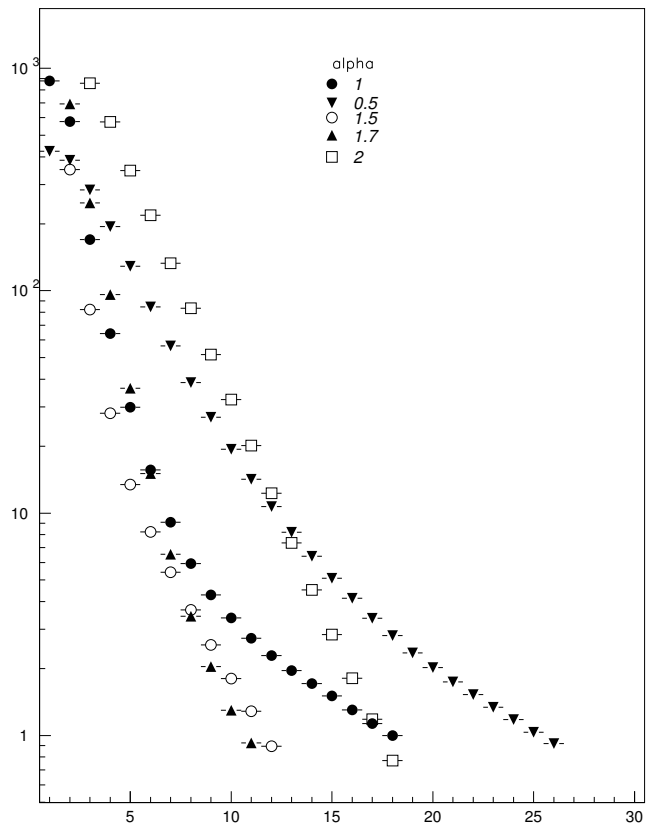

Figure 5.10: Convergence with respect to the value of the factor α (see text).

In order to perform the track fit, a resolution function has to be provided to the autocalibration algorithm. It will be shown in the next chapter that the resolution can be parametrized as an exponential function of the radius. The reference $r(t)$ is calculated using the resolution measured from the data (Ch. 6). A comparison

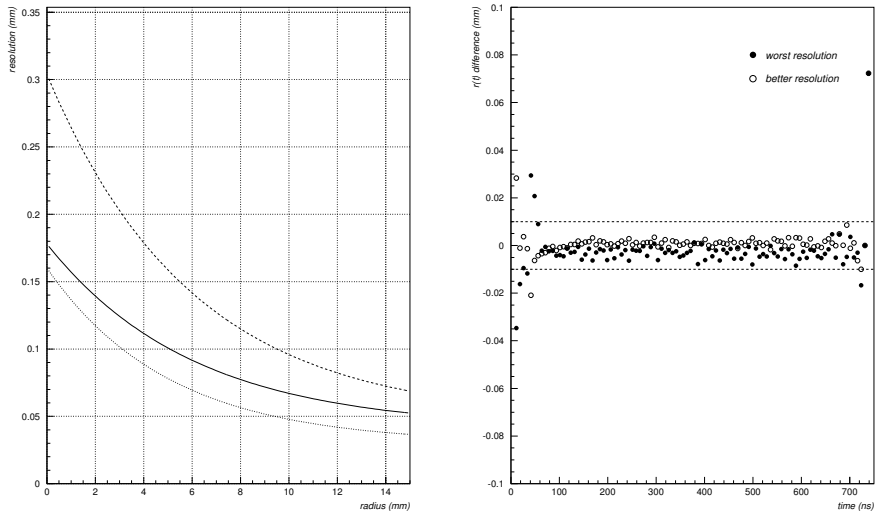

Figure 5.11: On the left plot the middle curve is the resolution function used to determine the reference $r(t)$. On the right plot the difference with respect to the reference $r(t)$ assuming a worst(better) resolution, drawn in upper(lower) curve on the left plot.

with the $r(t)$ obtained using both a higher and a lower resolution (reported in fig. 5.11(left)) is shown in fig. 5.11(right). For very general assumptions about the resolution function, differences in the calculated $r(t)$ are neglibile.
In fig. 5.12(top) it is shown the difference in the t_0 determined by fitting the whole drift time distribution (function 5.3) and fitting only the rising edge (function 5.4). The Gaussian fit to the distribution gives a standard deviation of about 1 TDC count. Fig. 5.12(bottom) instead shows a typical distribution of the $t_0's$ within the chamber. Tube-to-tube variation have a spread of about 1 TDC count as well. It is useful to quantify the sensitivity of the autocalibration algorithm to the $t_0's$ fit function used and to the tube dependent $t_0's$ variation. Fig. 5.13 reports the differences, with respect to the reference, of the $r(t)'s$ calculated by smearing the fitted $t_0's$ adding at random ± 1 TDC counts or zero TDC counts. The same is repeated by adding ± 2, ± 1 or zero TDC counts. The former operation does not vary the $r(t)$ by more then $10\mu m$ while the latter causes a deviation up to $20\mu m$ close to the wire. This means that a rough knowledge of the $t_0's$, regardless of the fitting method, is enough for a good calibration. The effect is larger if the average $t_0's$ is used for all the tubes. The discrepancies are as high as 100 μm if the maximum or the minimum value of the $t_0's$ is assumed. This case will be discussed later. The track incident angle also affects the autocalibration as shown in fig. 5.14. An angular aperture of at least ± 0.15 in the parameter a of the track is required (corresponding to $\pm 8.5^o$) for an accuracy of $10\mu m$. The samples analyzed have the same number of events. The systematics caused by

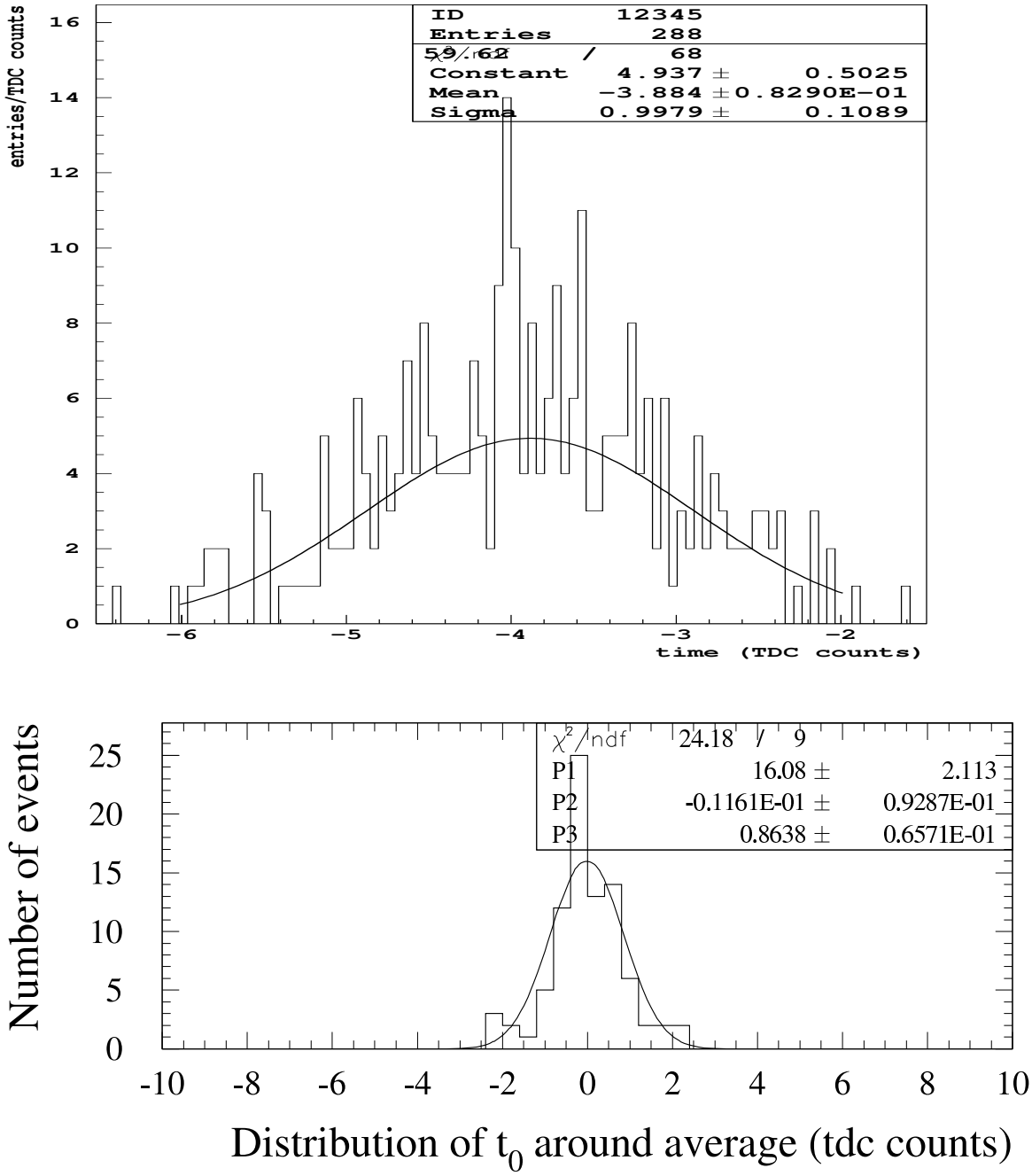

Figure 5.12: (*top*) Difference in the fitted t_0 using the function 5.3 or the function 5.4. (*bottom*) Distiribution of the $t_0's$ in a chamber.

almost parallel tracks is due to the fact that they correlate a unique set of drift radii and the autocalibration is not constrained enough.

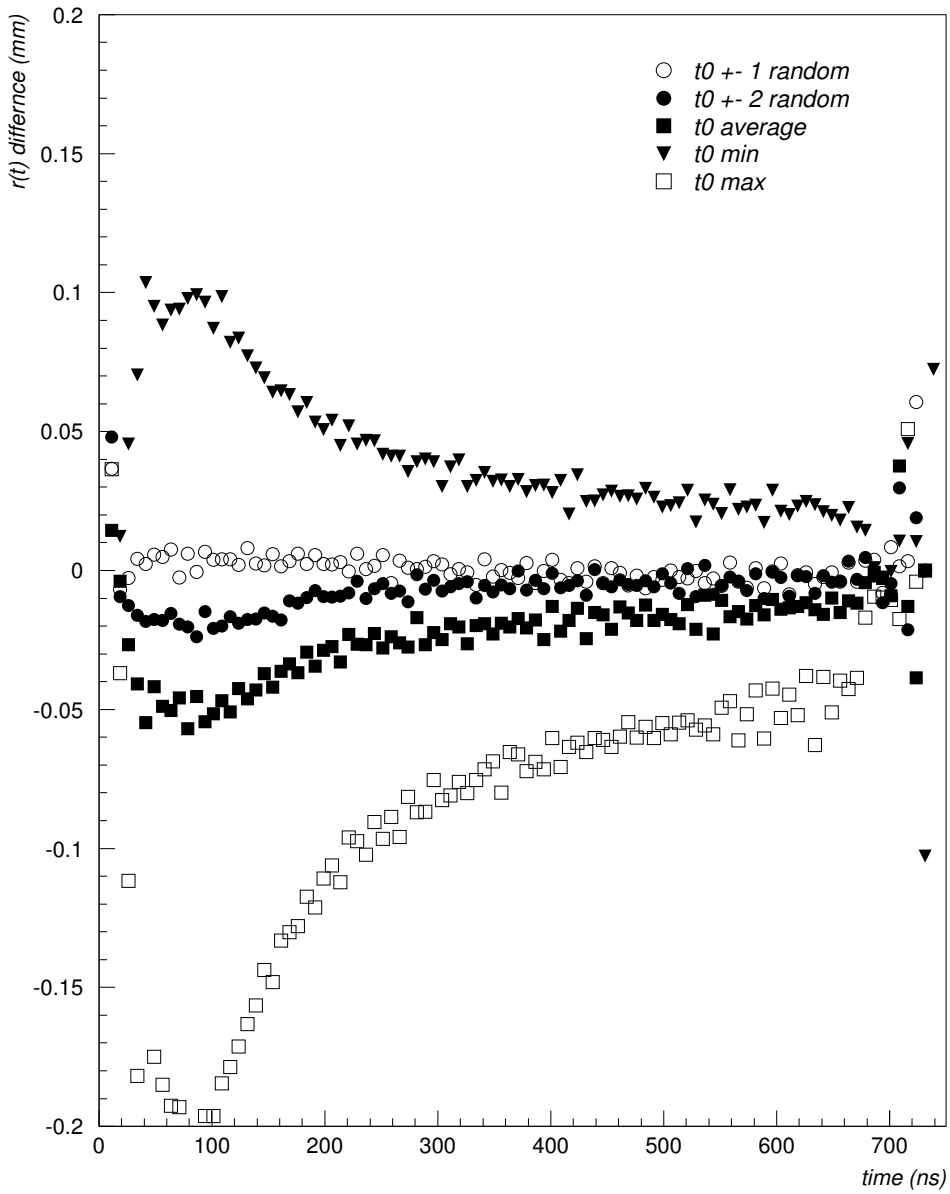

Figure 5.13: Differences with respect to the refrence $r(t)$ when the $t_0's$ are smeared (see text) and when a unique value corresponding to the average, the maximum or the minimum one is assumed.

5.4 Global Time Finding algorithm

A modified fitting algorithm can be coceived once cosidered that two hits associated to the same track cannot differ, in time, by more then the maximum drift

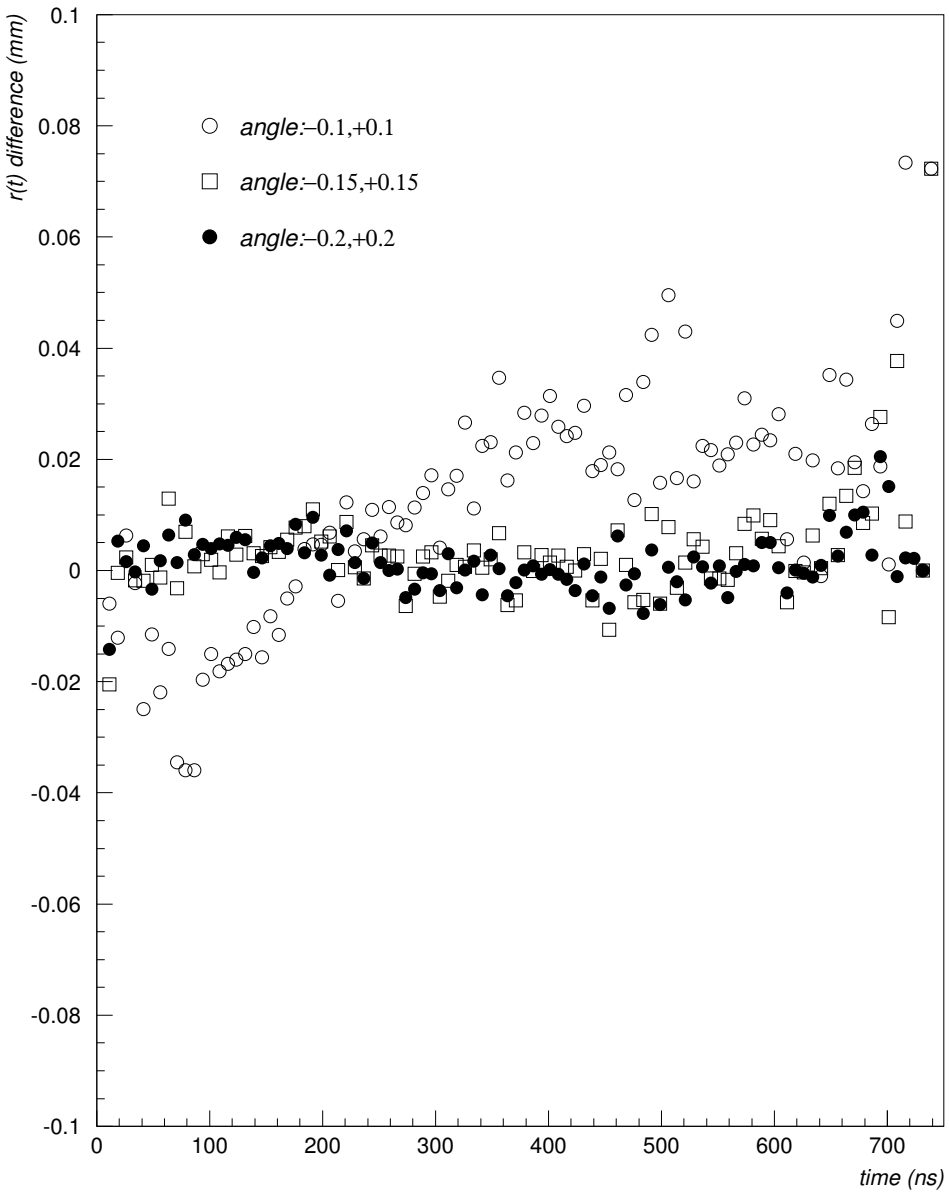

Figure 5.14: Difference between the $r(t)$ calculated using tracks with slope $a = [-0.1, +0.1]$, $a = [-0.15, +0.15]$, $a = [-0.2, +0.2]$ with respect to the reference $r(t)$ ($a = [-0.3, +0.3]$)

time of the tube, and, that small variation in tube $t_0's$ have a small effect on the $r(t)$ calibration. In fact, according to 5.2 the difference between two raw time of any two physical hits, 1 and 2 is

$$t_{m,1} - t_{m,2} = t_{drift,1} - t_{drift,2} + t_{0,1} - t_{0,2} \simeq t_{drift,1} - t_{drift,2}. \tag{5.13}$$

Anyway, the t_0 differences are characteristics of the chamber, and, if not negligible, can be determined preliminary by measuring directly the time delay of the signal in the electronics. From the 5.13 only in not possible a unique convertion into a radius since it is undetermined by a common *time shift* in the physical window as illustrated in fig. 5.15.

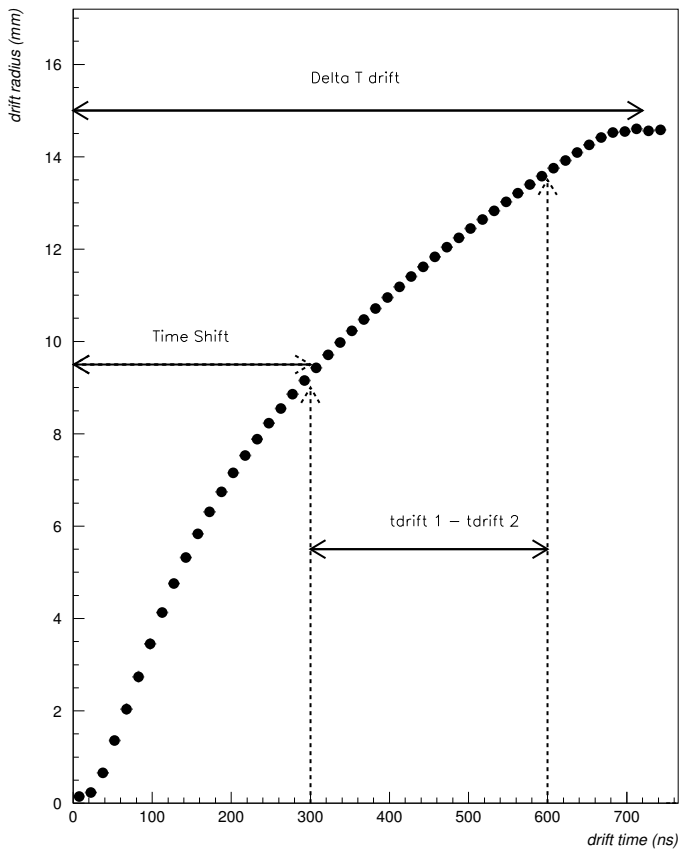

Figure 5.15: The knoledge of the *time shift* quantity is necessary. to associate the correct radius to each time measurements.

The following algorithm has been applied to determine the *time shift*.

1. A valid pattern is identified, as in the standard procedure (Ch. 4.3.2), that means a list of raw times t_m^i is available.
2. It is checked that the difference between the larger and the smaller time in the list, t_m^i, max - $t_m^i, min < \Delta T_{drift} = 923\ TDC$ counts ($\sim 720\ ns$). If this is not the case the hit with the largest time difference from the average (usually a noise hit) is removed from the hit list. The procedure is repeated until the inequality is met.

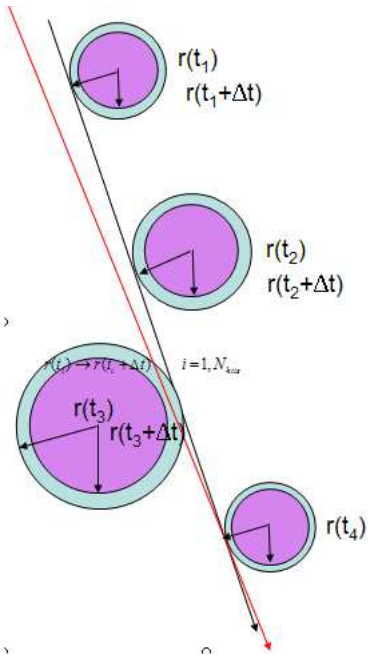

Figure 5.16: To minimize the χ^2 adding a common time to the time measuremnts is like to vary the associated radius to fit a tangent straight line.

3. times are scaled with respect to the minimum $t_{m,min}$:
   $t^i_m \rightarrow \hat{t}^i_m = t^i_m - t^i_{m,min}$, hence
   $0 < \hat{t}^i_m < \hat{t}^i_{max} = t_{m,min} - t_{m,max}$

4. Assuming an $r(t)$ relation, all the possible sets of radii (fig. 5.16) $r^i(0 + t_{shift}), ..., r^i_m(\hat{t}^i_{m,max} + t_{shift})$, are obtained by varying the time shift parameter in the range $0 < t_{shift} < \Delta T_{drift} - \hat{t}^i_{max}$ (see fig. 5.15). The correct t_{shift} value is defined as the one which minimize the χ^2 of the track fit (par. 5.2).

The last step is rather slow since several hundredths fits can be necessary to determine t_{shift}. The algorithm can be optimized using a binary research algorithm (3-4 itertion on average). This aspect can be compensated also choosing a proper value of the correction factor α (5.3).
The steps from 2 to 4 subsitutes the standard fitting algorithm and can be used for tracking and autocalibration without the information on $t'_0 s$. Moreover the knowledge of the *time shift* can be exploited to extract other information obout the event like the t_{delay} term of the 5.1 which, in turn, is related to the distance of the track along the tube.

The method has been validated by comparison of the autocalibration results. Fig.5.17(top) shows the difference in the calculated $r(t)$. Such a large discrepancy can be explained by the fact that its shape looks like a TDC spectrum. This

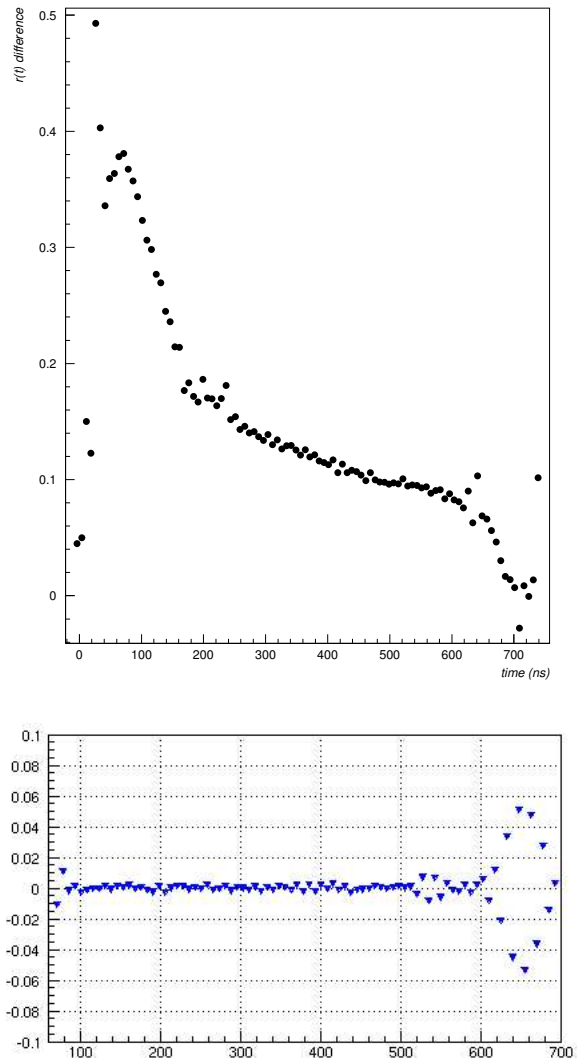

Figure 5.17: Differences of the $r(t)$ determined with the two methods described in 5.2 and 5.4. The same difference after a shift along the abscissa. The large differences at the borders reflects the behaviour of the Chebyshev polynomial at the boundaries of the fitted region.

happens when confronting two $r(t)'s$ which differ by a shift δt in time. In fact

$$r(t+\delta t) - r(t) \simeq \frac{d\ r(t)}{dt}\ \delta t \tag{5.14}$$

and the drift time distribution

$$\frac{dn}{dt} = \frac{dn}{dr} \cdot \frac{dr}{dt} \tag{5.15}$$

is proportional to dr/dt if the tube is uniformly illuminated: $\frac{dn}{dr} = const$. The two $r(t)'s$ have been fitted with a Chebyshev polynomial of order 16 and then

the difference computed as a function of the quantiy δt. Fig. 5.17(bottom) shows the results for $\delta t \simeq 7ns$. Differences are at the micron level.

This consideration explains also that the major differences with respect to the reference obtained in the two $r(t)s$ of fig. 5.13 determined assuming all the $t'0$ equal to the minimum (maximum) one are mostly due two a systematic shift of the times superimposed to the less relevant tube to tube t_0 variation. Diffences

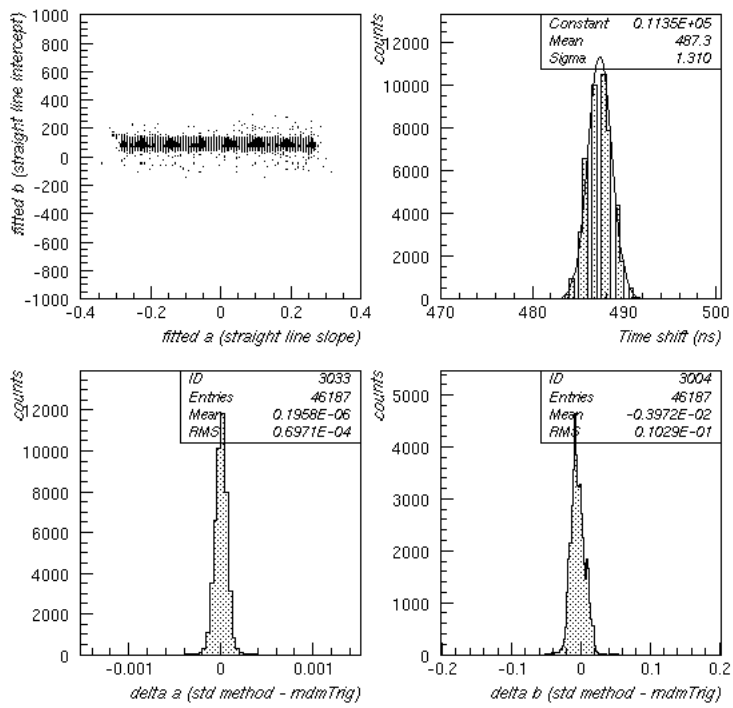

Figure 5.18: (*top left*) Correlation between the track parametr a and b. (*top right*) TimeShift distribution. (*bottom*) Comparison between track parameters.

in the fitted track parameters are within $70\mu m$ for the slope a and of about $10\mu m$ for b (calculated between the two multilayers), fig. 5.18. Fig. 5.18 shows also the distribution of the quantity:

$$TimeShift = t_{shift} - t_{m,min} \tag{5.16}$$

TimeShift inidicate the beginning of the physical spectrum. For tracks crossing the tubes in a very narrow region in the wire direction, like at the Test Beam setup, it should not vary from event to event. The width of it's distibution, 1.3 ns, it is assumed as the measure of the intrinsic time resolution of the method.

5.4.1 Second coordinate measurement

The setup reported in fig. 5.19 is described in 4.1.2. Three runs (420,432 and 433)

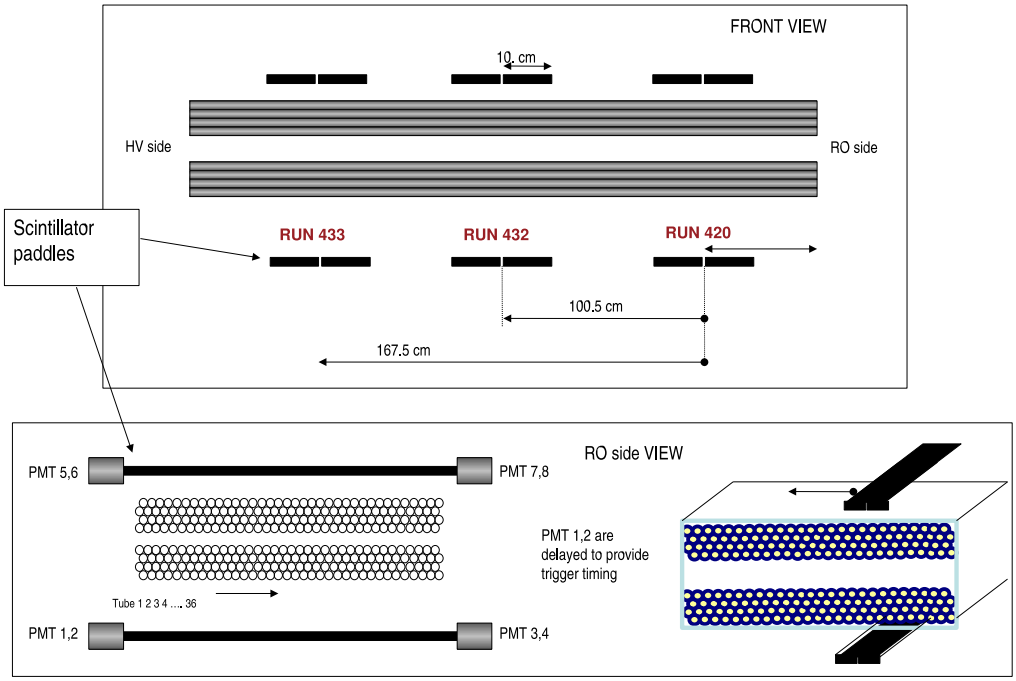

Figure 5.19: Experimental setup used for second coordinate measurements.

have been taken placing the trigger planes at diffrent distance from the RO along the tubes. As expected the TimeShift distributions have the same width but different mean for different runs. This reflects the delay due to the propagation of the signal along the wire. With this setup the width of the TimeShift is larger (2.3 ns) with respect to the test beam: this is mostly due to the propagation of the signal in the scintillators which induces a delay dependending on the distance of the muon impact point from the scintillator read out (fig. 5.21). After correcting for this effect the rms width is still a 30% larger beacuse of the finite length of the scintilltor pad in the wire direction and of trigger jitter effects already experinced with this setup. A scatter plot of the TimeShift mean versus the average trigger position gives the propagation velocity along the wire (fig. 5.22). The meausured value is 23.4 ± 0.2 ns. Hence with a time resolution of 1.3 ns it is possible to determine the position of the track in the tube direction with a precision of about 30 cm. This may be useful in regions where the information on the second coordinate is missing.

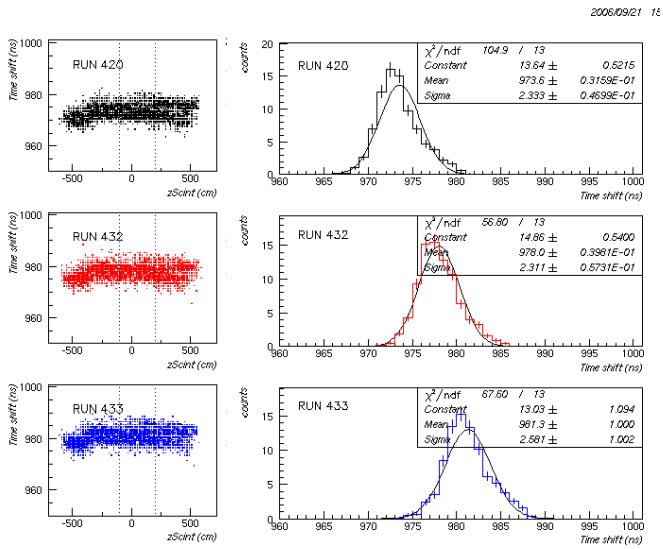

Figure 5.20: TimeShift for different runs.

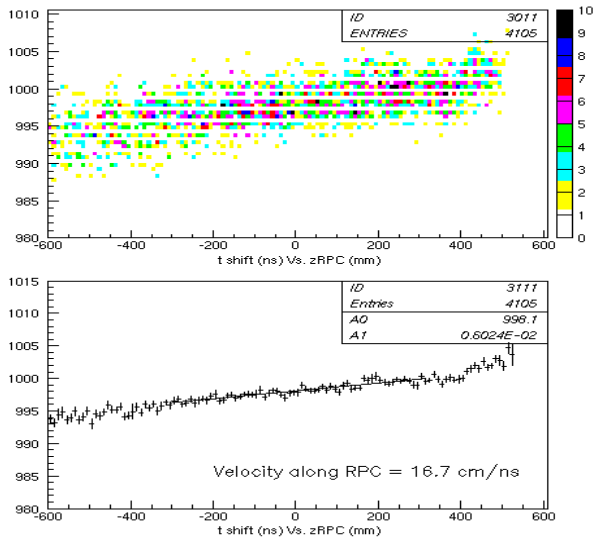

Figure 5.21: The signal speed in the trigger plane can be measured from the distribution of the TimeShift versus the impact point of the reconstructed track on the trigger plane.

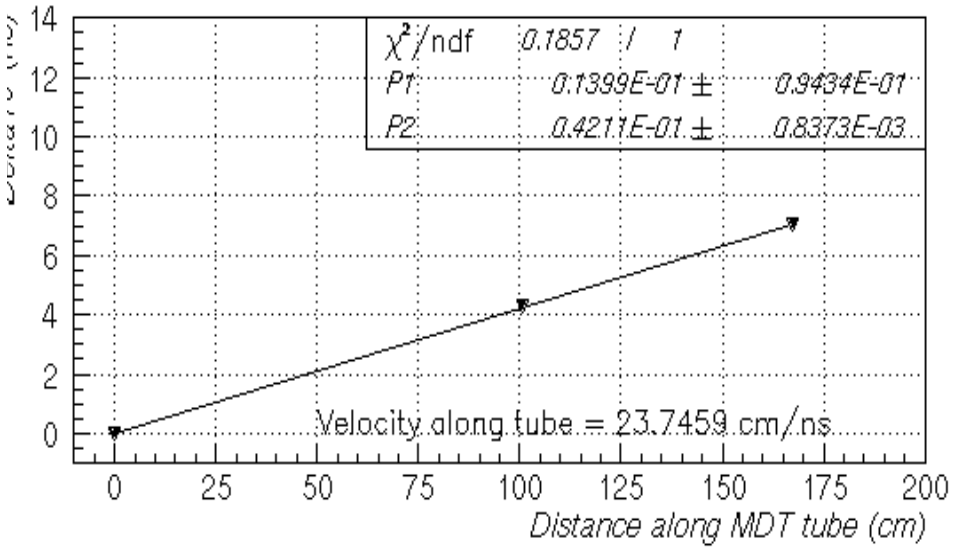

Figure 5.22: Signal speed along the anode wire.

Chapter 6

Resolution studies

6.1 Single tube resolution

The single tube resolution is the intrinsic accuracy of a drift tube for track reconstruction depends, in general, on the drift radius. For a sample containing a large number N of tracks, which all traverse an MDT in a distance d from the wire, the resolution is

$$\sigma^2(d) = \frac{1}{N} \cdot \sum_{i=1}^{N} |d - r(t_i)|^2; \tag{6.1}$$

$r(t_i)$ is the drift radius reconstructed from the measured drift time of the *i-th* track.

6.2 Tube resolution determination without external reference

To calculate the tube resolution directly according to equation 6.1, the track position d with respect to the wire must be known accurately. This is, for example, the case if d is measured independently by a high precision external reference tracker. If no such detector is available the distance d had to be determined from the MDT data itself. In this case, since the distance d calculated from the equation of the fitted track, depends on the resolution itsef, an iterative procedure is needed.

The following algorithm was used to derive the resolution function $\sigma(r)$.

1. Patterns belonging to a track with a defined number of hits are selected; default is 8.

2. One tube from the track is excluded, and a straight line is fitted to the remaining hits according to equation 5.11, using an estimated resolution $\sigma_n(r)$ with $n = 0$. A cut on the χ^2 can be applied.
3. The track is extrapolated to the excluded tube and the track distance r_{track} from the tube wire is calculated;
4. Calculation of the residual $\Delta(r_{track}) = r_{track} - r_{drift}$ and the fit extrapolation error, i.e. the error $\varepsilon(r_{track})$ in r_{track} for the excluded tube;
5. Execution of the operations from 1 to 4 until all events are processed;
6. Slice in r of the residual distribution, 1 mm wide, are fitted with a Gaussian with width σ_d. The average extrapolation error $\bar{\varepsilon}$ in the same slice is calculated as well;
7. A new estimate for the tube resolution is derived as

$$\sigma_{n+1}(r) = \sqrt{\sigma_d(r)^2 - \overline{\varepsilon}(r)^2}. \tag{6.2}$$

8. Iteration 1 to 7 until σ_{n+1} equals σ_n within few microns.

The 6.2 can be derived according to the following considerations. Let r_0 be the 'true' trajectory distance from the wire of the excluded tube (r_{track} is the distance found from the fitted track). Then

$$\sigma_d^2 =< (r_{drift} - r_{track})^2 >=< (r_{drift} - r_0 + r_0 - r_{track})^2 > \tag{6.3}$$

$$=< (r_{drift} - r_0)^2 > + < (r_{track} - r_0)^2 > \; + 2 < (r_{drift} - r_0) \cdot (r_{track} - r_0) > .$$

The last term vanishes since r_{drift} and r_{track} are statistically independent: r_{drift} is not used to fit the track used to calculate r_{track}. Hence

$$\sigma_d^2 =< (r_{drift} - r_0)^2 > + < (r_{track} - r_0)^2 >= \sigma^2 + \overline{\varepsilon}(r)^2, \tag{6.4}$$

that is the 6.2.

6.3 Test Beam resolution

The method described above has been used to measure the resolution on a Test Beam data sample (par. 4.2). It is a BILrot-type sample of about 10^5 events. The discriminator threshold is 40 mV.

Fig. 6.1 shows a typical distribution of the residual and of the extrapolation error: σ_d is measured by fitting a Gaussian to this distribution. The resolution converges after few (usually from 3 to 6 depending on the input resolution) iterations. The final resolution $\sigma(r)$ (eq. 6.2) is reported in fig. 6.2. The two contributions $\sigma_d(r)$

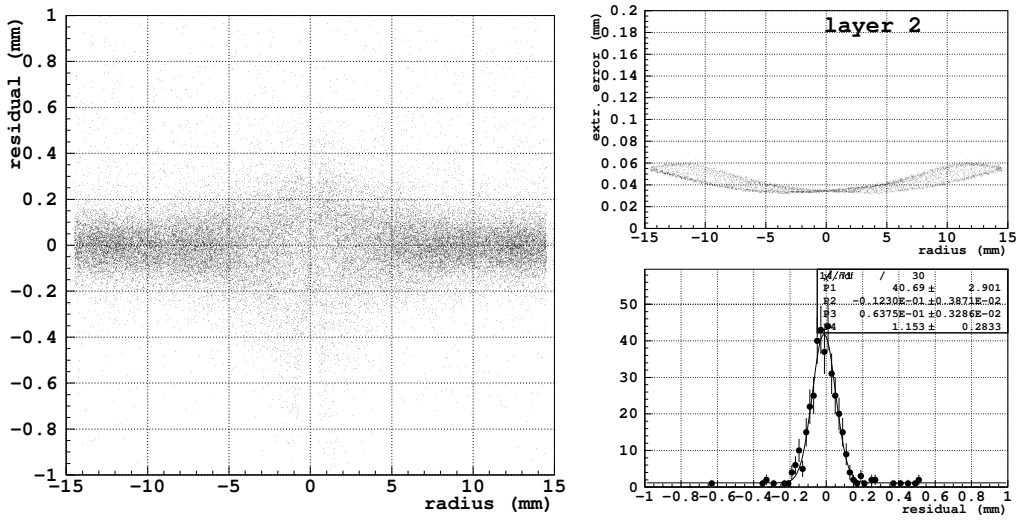

Figure 6.1: Residual (left) and extrapolation error (right top) distribution versus signed radius. The right bottom plot shows the residual for the range 10 $mm < r < 11$ mm.

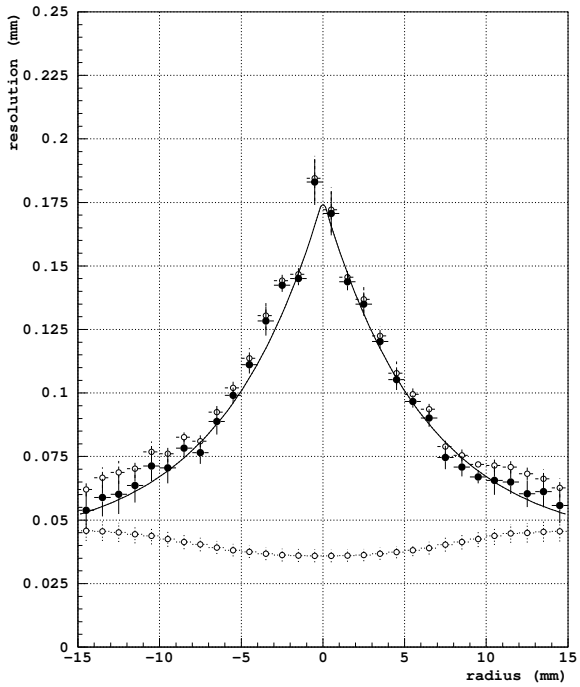

Figure 6.2: Tube resolution measured at the Teast Beam. The two contributes (see txt) to the final resolution are shown along with an exponential fit.

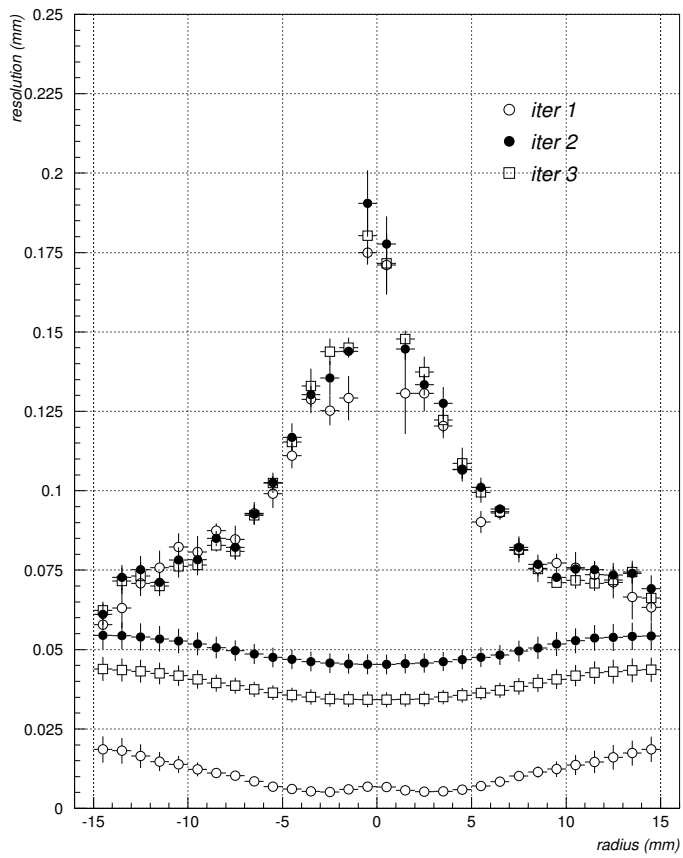

Figure 6.3: Variation of Residuals and extrapolation error with iteration.

and $\overline{\varepsilon}(r)$ are also shown separately. The measured value of about 180 μm close to the wire and 55 μm close to the tube wall ($\sim$ 70μm at $r = 1$ cm).

The dependence on the radius can be fitted with an exponential:

$$\sigma(r) = p_1 + p_2 \cdot e^{-\frac{r}{p_3}} \tag{6.5}$$

that is $p_1 + p_2$ at $r = 0$ and roughly equal to p_1 close to the tube wall. Fitted values for the distribution of fig. 6.2 are:

$$p_1 = 0.041 \pm 0.0067\ mm, \tag{6.6}$$

$$p_2 = 0.137 \pm 0.0055\ mm, \tag{6.7}$$

$$p_3 = 6.029 \pm 0.789.\ mm \tag{6.8}$$

From fig. 6.3 can be noticed that the convergence of the calculated resolution is mostly due to the convergence of the extrapolation. The extrapolation error

in fact is more sensitive to the resolution parametrization used at track fitting level with respect to the residual distribution. This is a consequence of the weak dependence of the autocalibration on the initial resolution function used (par. 5.3).

6.4 Simulation with GARFIELD

To simulate the MDT resolution, muon tracks of 170 GeV have been generated with GARFIELD (see par. 4.4) at several fixed distances d from the tube center. The drift of the ionization electrons is simulated taking into account diffusion and attachment in the gas ($Ar(93\%) : CO_2(7\%)$ at 3 bar). A Polya distribution (3.29) with parameter $\theta = 0.5$ was used to describe the gas amplification process.

The signal propagation along the anode wire and the properties of the front end electronics (ASD) were taken into account by folding the raw current signal $I(t)$ with the transfer functions of an MDT and the ASD amplifier-shaper circuit. The output of this trasformation is a voltage signal $V(t)$ as seen by the discriminator.

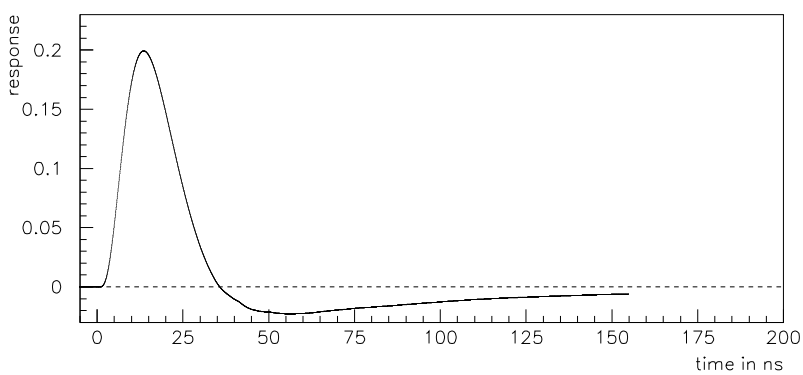

Figure 6.4: Transfer function for bipolar shaping with peaking time of 15 ns.

The transfer function $f(t)$ ($g(s)$ in the Laplace transform) for bipolar shaping is:

$$g(s) = \frac{n! s\tau}{(1+s\tau)^{n+2}} \rightarrow f(t) = (1 - \frac{t/\tau}{n+1})(t/\tau)^n \; e^{-t/\tau} \tag{6.9}$$

where n is the order of the transfer function, that is equal to 2 for the MDT electronics (there are 2 integration stages, Ch. 3). The peaking time of the function is defined as $\tau_p = \tau \cdot (n + 1 - \sqrt{n+1})$. For the MDT configuration $t_p = 15$ ns. The transfer function provided to GARFIELD is shown in fig. 6.4.

One also needs the ion mobility table (i.e. mobility vs elctric field) which was generated from the points of the fig. 3.6. The threshold of the Test Beam runs

(40 mV) has been chosen. Temperature aslo has been adjusted to match the one of the data sample considered for comparison. In a last step the time t_{th} at which a given threshold is crossed by the signal (for the first time) is calculated. After all tracks for a given distance d from the wire have been analyzed, the single tube resolution at the distance d, $\sigma(d)$ is obtained as

$$\sigma(d) = \sigma_{t_{th}} \cdot v_{drift}(d) \tag{6.10}$$

that is the product of the width $\sigma_{t_{th}}$ of the t_{th} distribution (Gaussian fit) and the electron drift velocity in at the radial distance d, $v_{drift}(d)$.

Fig. 6.5 shows the comparsion with data. Except for radii below 1 mm the agreement with the data from the Test Beam is within 10 μm.

6.5 Contributions to the resolution

In order to validate the Monte Carlo program described in 4.5 a sample of tracks has been generated according to the option 4.b of the simulation chain reported in 4.5. All tracks hit the chamber normally ($\theta = 0$) The resolution parametrs adopted are those reported in 6.6- 6.8 in order to reproduce the Test Beam conditions.

The parameters obtained from the fit to the resolution derived as for experimental data gives back the input resolution, fig. 6.6(right), this assures that no bias and

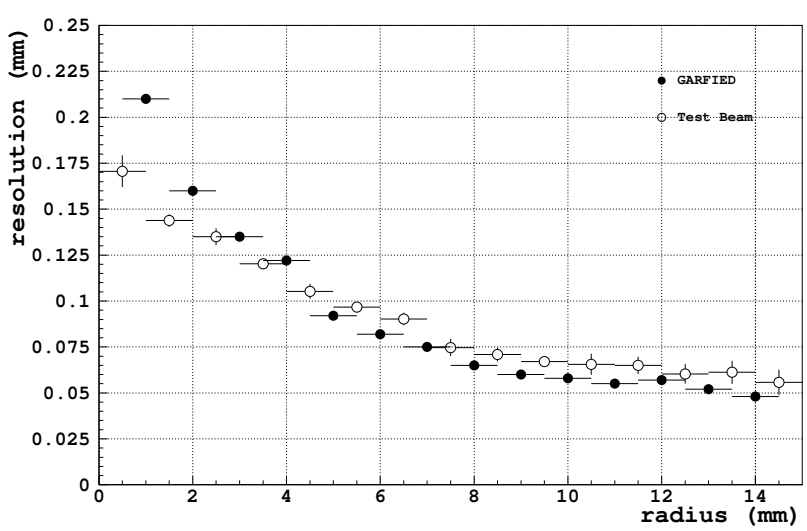

Figure 6.5: Resolution obtained with GARFIELD (full circle) and measured at the Teast Beam setup (empty circle).

systematics are presents. Fig. 6.6(left) shows that, as desirable, the chi-square distribution equals the chi square function for 8-2=6 degrees of freedom and that the chi-square probability is flat.

In fig. 6.7 can be seen as the extrapolation error distributions have a rahter narrow profile differently from the scatter plot of fig. 6.1. This a consequence of the angular spread as demonstrated from the distributions of fig. 6.8. This means that the resolution calculated using the 6.2 do not take into account the spread of the extrapolation error (but only an average value). As a consequence the resolution is overestimated as can be seen from the plots in 6.9 and 6.8(right).

Previous considerations suggest that a better way to determine the resolution is just to find the parametrization which makes the chi-square probability flat. Fig. 6.10 shows the resolution measured using a sample taken at Roma Tre with the scintillator trigger hodoscope. The results is worst with respect to the Test Beam sample. This difference can be explained by simulating the combined effect of the multiple scattering and of the trigger jitter, see 4.5. The propagation velocity inside the trigger plane was measured to be about 14 cm/ns and this value used as input to the simulation. Multiple scattering of muons with the momentum distribution and angular distribution of cosmic rays have been enabled.

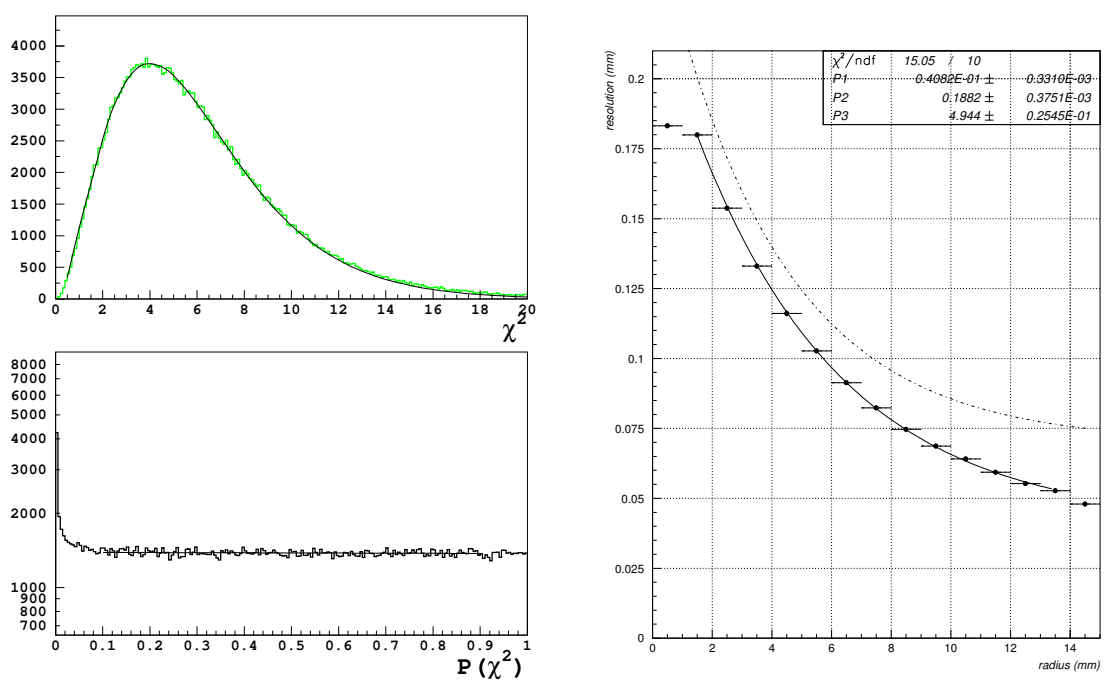

Figure 6.6: (left) Chi-square and $P(\chi^2)$ distributions. (right) Resolution calculated applying reconstruction on simulated data. The dotted curve represents the input resolution. Incidence angle: $\theta = 0$.

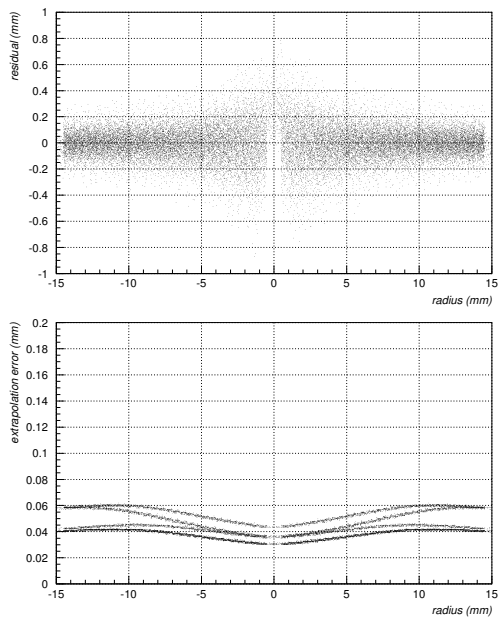

Figure 6.7: (top) Residual distribution. (bottom) Extrapolation error for different layers. Incidence angle: $\theta = 0$.

The result is reported in fig. 6.11: the multiple scattering contribution is almost flat (radius independent) as expected hence affects mostly the resolution at large radii while the effect of the trigger is more important close to the wire where the drift velocity is higher. Adding those two contributions to a Test Beam like resolution a resolution very similar to the measured one, fig. 6.10, is obtained.

Fitting the tracks with the algorithm decribed in par. 5.4 the resolution improves expecially for small radii, fig. 6.12, since global event by event variation in the raw time of the hits are reabsorbed in the definition of the event t_0.

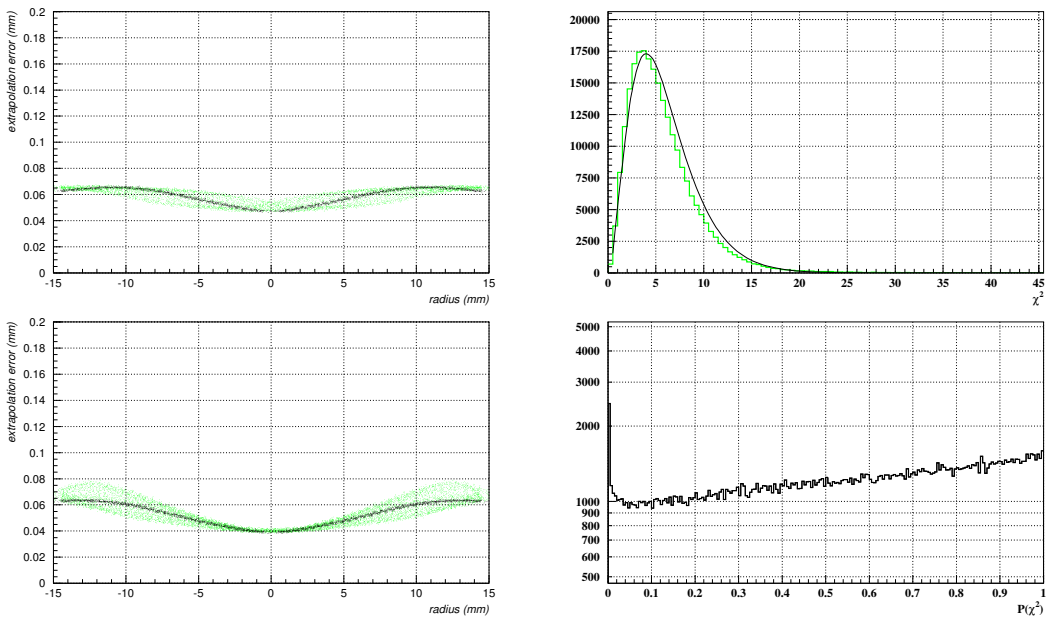

Figure 6.8: (left) Extrapolation error for two layers. The darker area corresponds to incidence angle $\theta = 0$. (right) Chi-square and $P(\chi^2)$ distribution (the curve is the Chi-square function with 6 d.o.f.). Incidence angle: $\theta = \pm 0.1$

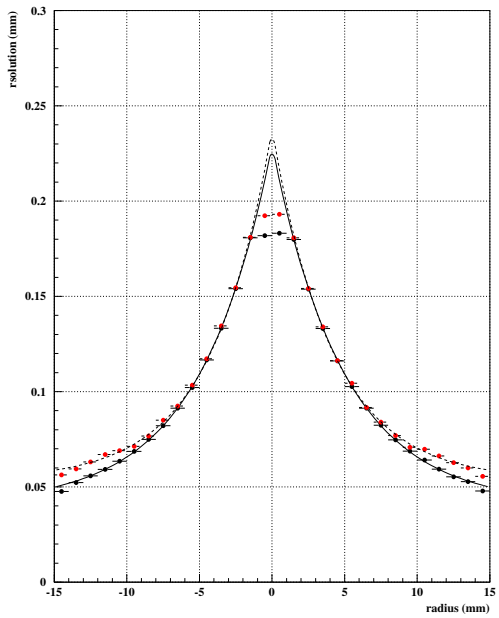

Figure 6.9: Comparison of the resolution between a sample generated without angular spread and a sample with a spread in the track slope a of ± 0.3.

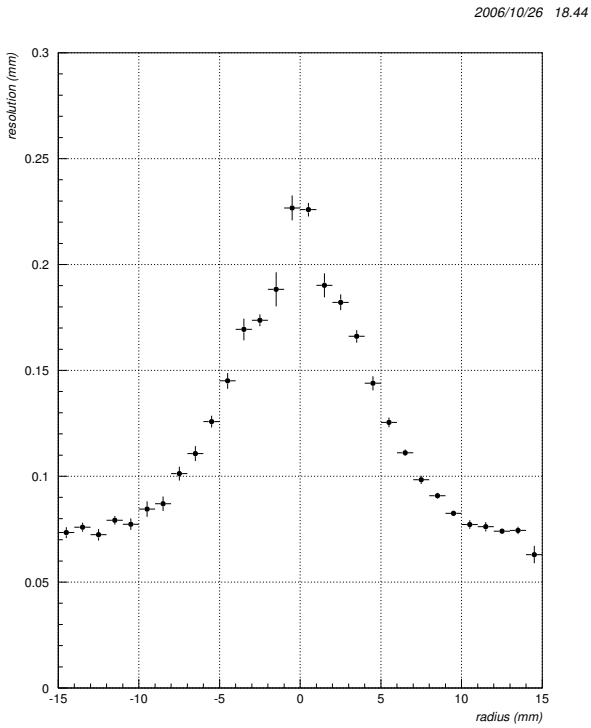

Figure 6.10: Resolution at the Roma Tre setup.

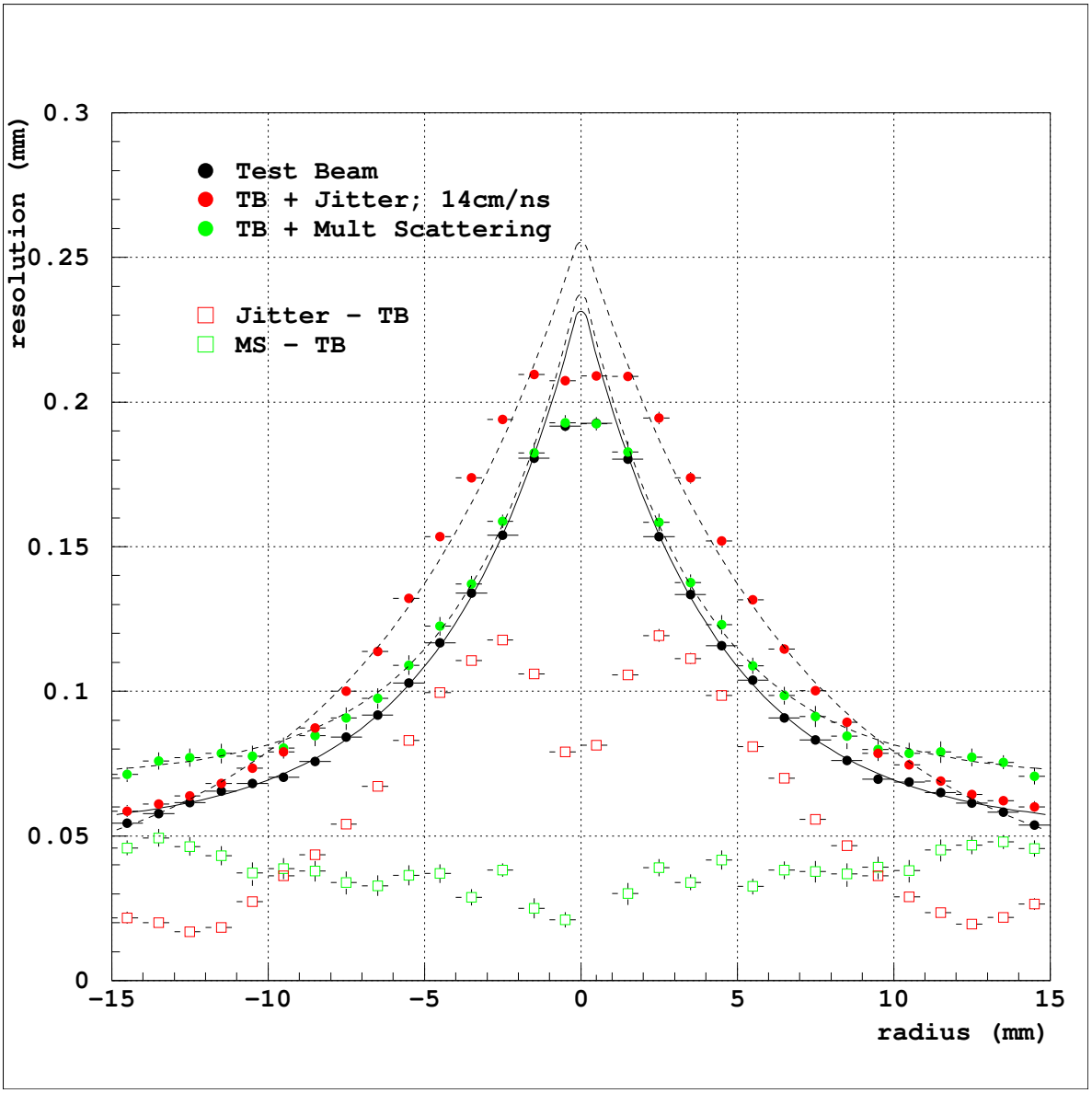

Figure 6.11: Contributes to the resolution.

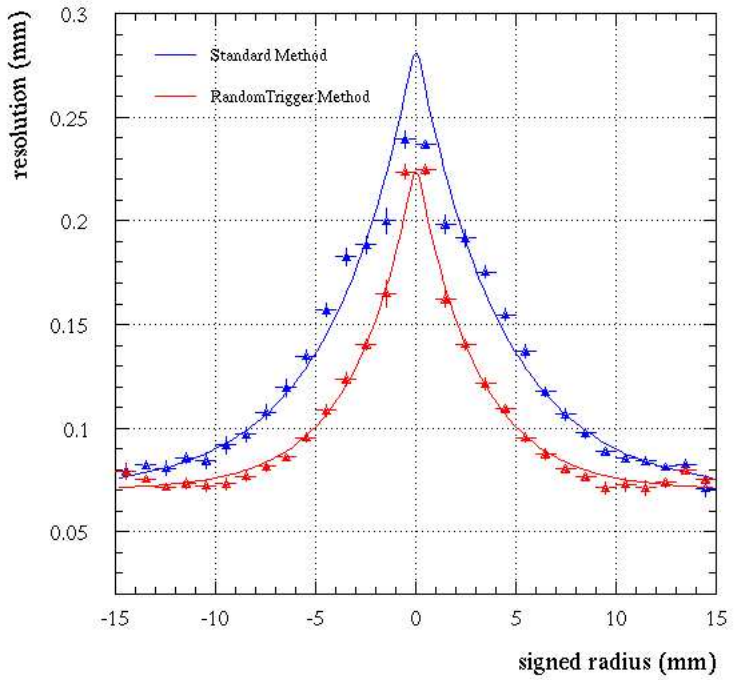

Figure 6.12: Comparison betwee the resolution calcualted with the standard track fitting (upper distribution) and with the Global Time Finding algorithm (par. 5.4).

Chapter 7

Background studies

Large radiation doses are expected for detectors at the LHC experiments. Compared, for example, to the previous experiments at the LEP, HERA and the B-factories, the increase in the background particle rates is up to four orders of magnitude. Hence a significant increase in radiation hardness is required which implies not only careful selection of materials but also the definition of precise procedures for chamber assembly and operation.

In the era of LHC and forecasting an upgrade for $SLHC$ (SuperLHC) it is crucial to test the detector robustness in the harsh background environment.

The expected background conditions in the $ATLAS$ hall have been described in the section 3.4: simulations give a maximum total count rate of about 500 Hz/cm^2 under nominal LHC operation that can be 10 times higher under $SLHC$ operation. This corresponds to an accumulated charge of about 5 $C/cm/wire$ in 10 years of $SLHC$ operation.

A degradation of wire chamber performances after extended operation in a high-rate environment is usually caused by the formation of deposits on the anode wire. These deposits can result from polymerization of the operating gas components or from contaminants in the mixture.
Considering also that, due to the complexity of the whole apparatus architecture, detector element replacement would be decidedly unconvinient, a study of the factors limiting their lifetime is particularly important.

Two small test Monitored Drift Tubes chambers have been built and equipped with the standard gas distribution system, high voltage distribution and front-end electronics to study their response under gamma irradiation accumulating a total charge of 4.8 C/cm/wire (which corresponds to about 10 years at $SLHC$ luminosity). A neutron irradiation test was also performed integrating 1.4×10^{12} neutrons/cm^2 (equivalent to about 30 years of $SLHC$ assuming the expected

neutron rate of 5 kHz/cm^2, 3.4).

An overview of different chamber aging mechanisms is reported in section 7.1. The gamma irradiation facility and the experimental setup are described in sections 7.2 and 7.3 respectively, while data taking and slow control are described in sections 7.5 and 7.6. The analysis of the drift time and collected charge spectra and tracking performance are discussed in sections 7.7 and 7.8. The result of electronic microscopy of the wires is summarized in section 7.9. It follows the description of the test performed at the neutron irradiation facility. The work presented here has been published in [61].

7.1 Wire chamber aging mechanisms

Aging effects observed in wire chambers [40, 41, 42] are normally due to deposits on either the anode or the cathode surface. Already thin coatings on the anode wire, which can be either electrically insulating or not, lead to a loss in gas gain. As an example, consider an MDT wire with an original diameter of $50\mu m$ which is increased by $2\mu m$ due to the deposition of a conducting film of material; by substituting the different radii into Diethorn's formula and using the Diethorn parameters for $Ar : CO_2$ (93 : 7), as specified in 3.2.3, one finds a corresponding gain reduction of 23 %.

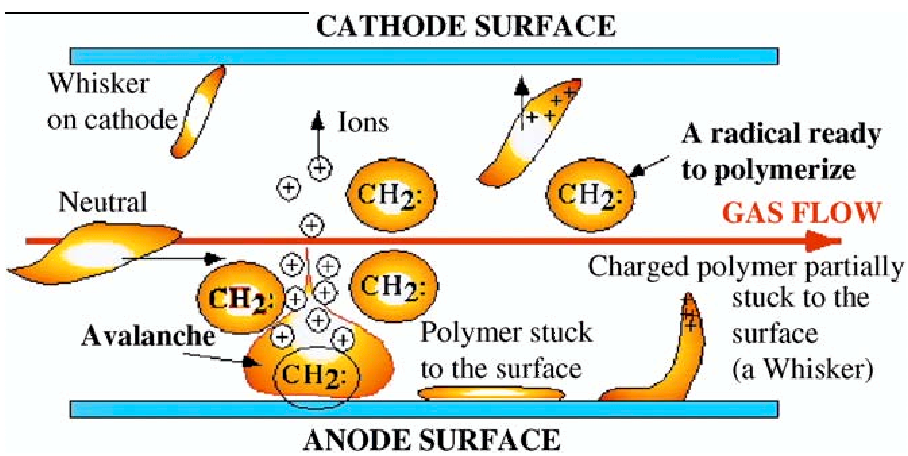

Figure 7.1: Schematic of process leading to wire chamber aging.

Deposits on the cathode have no direct impact on the gas gain; they can however be the cause for spontaneous discharges and self-sustained currents via a mechanism known as the Malter effect: if the cathode is coated by a thin film of insulating material, the neutralization of positively charged ions, produced either by a traversing particle or in the gas amplification process, is impeded. A positive

charge builds up at the boundary between the insulating layer and the operating gas of the drift tube; the consequence is an electric field perpendicular to the cathode surface which can be strong enough for electrons to be liberated from the cathode material by field emission. These electrons then drift to the anode wire where they undergo gas amplification, producing more ions which in turn move towards the cathode, contribute to the space charge and close the cycle. The result is a self-sustained current. Once the Malter effect manifests itself in a drift tube, its use for particle detection is very limited due to the large number of (fake) pulses and the degradation of the electric drift field caused by the large number of drifting ions.

Deposits, especially on the anode, can take the form of whiskers, droplets or a uniform coating; they can be both solid or liquid, brittle or viscous (fig. 7.1). One generally assumes that their formation is a polymerization process which involves either the molecules of the operating gas itself or a contaminant. In both cases the deposition of material on the wire surface competes with etching or ablation effects. Etching in this context is the process in which molecules are transferred from a solid phase (wire deposit) into the gas phase by a bombardment with electrons (from the gas amplification). Particular mixtures containing fluorine, e.g. in the form of CF_4, are known for their large potential for removing material from the anode wire of drift tubes; they are therefore sometimes deliberately used to prevent chamber ageing or as a cleaning gas. Aging effects can in some cases also be avoided by adding water or an alcohol to the gas mixture.

The mechanism by which these additives work is not yet fully understood. Since the ionization potential of most alcohols A is relatively low, one may speculate that charge transfer reactions $X^+ + A \rightarrow A^+ + X$ play a role by neutralizing a molecular ion X^+ in a more 'gentle' way than by the recombination process $X^+ + e^- \rightarrow X$ taking place at the cathode, with the result that the molecule is prevented from breaking up. Water on the other hand might produce radicals of the form HO·, which can saturate the polymerization process before chains become so long that they are no longer volatile and attach themselves to the cathode or, with greater harm, to the anode.

Aging from gas polymerization

Most drift detector gases containing hydrocarbons tend to polymerize under high irradia- tion. A hypothetical polymerization reaction, showing the involved processes and starting from methane, is

$$CH_4 + e^2 \rightarrow CH_3 \cdot + H \cdot + e^- \quad (1)$$
$$\mathrm{CH}_4 + e^- \rightarrow CH_2 : + H_2 + e^-$$
$$\mathrm{CH}_2 : + CH_2 : \rightarrow C2H4 + 2H2 \quad (2)$$
$$\mathrm{CH}_2 \cdot + C_2H_4 \rightarrow C_3H_7 \cdot \quad (3)$$
$$\mathrm{C}_3H_7 \cdot + C_2H_4 \rightarrow C_5H_{11} \cdot$$

$$\ldots$$
$$\mathrm{C}_n H_{2n+1} \cdot + H \cdot \rightarrow C_n H_{2n+2} \quad (4)$$
$$\mathrm{C}_n H_{2n+1} \cdot + C_m H_{2m+1} \cdot \rightarrow C_{n+m} H_{2(n+m)+2}$$

In (1) a methane molecule loses one or two of its hydrogen atoms due to the bombardment with electrons. The result is a radical with at least one unpaired electron, denoted by the "·" symbol, in the shell of the C-atom. Radicals are a very reactive species; they try to reach a stable, i.e. saturated, electron configuration by forming chemical bonds. The product of reaction (2) is the chemical compound ethylene, C_2H_4, in which two carbon atoms are connected by a double bond (C=C). Both free radicals and molecules with a double (or triple) bond are needed for the actual polymerization process (3).The unpaired electron of the radical and one of the electrons from the C=C double bond form a new single bond; the radical gets attached to the molecule which grows in size. The result of many such reactions is a hydrocarbon chain whose overall length is determined by the frequency with which one of the termination processes (4) occurs. Hydrocarbons above a certain size are normally non-volatile; if this size is reached in a drift detector, they will condense on the available surfaces which leads to the deposits responsible for ageing.

Results from different studies ([59, 60]) confirmed that this aspect is the main reason for not using hydrocarbon compounds as the operating gas for the ATLAS MDTs.

Aging from gas contaminants

Every drift detector contains non-metallic components which harbour the risk of polluting the operating gas. The main mechanisms by which contaminants are produced are

- Outgassing: Plastic materials often contain traces of non-polymerized monomers left from their production. Since these are not firmly bound to other molecules they can over time evaporate from the material. Outgassing can be particularly severe in glues, if they are not cured properly, and in plastics containing softeners.
- Dissociation and material breakdown under irradiation: Chemical substances that are very stable under normal conditions can rapidly deteriorate if they are exposed to ultraviolet or ionizing radiation. In the case of organic compounds, this will mainly lead to the outgassing of H_2, though a substantial amount of heavier and more deadly molecules can also be produced. Certain chemical groups increase the radiation resistance of a material. Among them are aromatics like the phenyl group $-C_6H_5$. These groups can absorb large excitation energies and hence prevent a molecule from dissociating; the yield for the production of radicals is low. Examples for plastic materials

suitable for use in a high radiation environment are polyimide (KaptonR) and polyether-ether-ketone, PEEK.

- Evaporation: Valves in a detector gas system are often greased to prevent them from getting stuck. Soft sealants are used to achieve gas tightness and oils may be present in bubblers to monitor the gas flow. In each of these cases molecules will evaporate from the surface of the liquid or (semi)solid material until the concentration in the gas phase equals the vapour pressure of the given substance.

- Improper cleaning: A variety of oils, lubricants and cooling fluids is used in the production and machining of both plastics and metals. They have to be thoroughly removed from the components of a drift detector before its assembly in order to avoid uncontrolled contamination of the operating gas.

From the above list it is evident that materials used in the construction of gaseous detecors to be operated under high rates need to be carefully chosen in order to guarantee an adequate lifetime. The mechanism by which contaminants cause ageing in a wire chamber is, as in the case of ageing due to the operating gas, the formation of deposits either on the anode or the cathode. Molecules with a large dipole moment are attracted to the anode wire by the inhomogeneous electric drift field. If they are heavy, they can stick to the wire surface and gradually build up an insulating or conducting layer of material. Once attached to the wire they are exposed to an intense bombardment with electrons from the gas amplification process. In many cases they will therefore polymerize and form heavily macro-molecules. If ageing is caused by a pollutant, it is not guaranteed that a higher gas flux will reduce the effect. On the contrary, the growth rate of a deposit will increase with the gas flow if the probability for impurities to be captured by the anode wire is high, since in this case a larger number of molecules is transported into the detector volume in a given time [30]. An element found as a deposit on the anode wire in numerous ageing studies is silicon (Si). Silicon belongs to the same group of the periodic table as carbon. Their chemical reactions are therefore similar. Silicon can polymerize - both with carbon and with oxygen. The result are macro-molecules either

```
   |         |         |                  |    |    |    |    |
— Si — O — Si — O — Si —      or      — Si — C — Si — C — Si —
   |         |         |                  |    |    |    |    |
```

as their backbone. A 3-dimensional cross-linking is also possible. The simplest, purely inorganic structure in this case is $(SiO_2)_n$, which has a crystalline consistency and is found in silica glass and sand.

Silicon atoms found in a drift chamber usually stem from silicone materials, which are either used in its construction or present in the gas system. Silicones are chemical sub- stances in which organic compounds are at-

tached to a $(SiO)_n$ chain. The most basic silicone is poly-dimethyl-siloxane $(Si(CH_3)_2O)_n$,

$$\begin{array}{ccccccccc} & CH_3 & & CH_3 & & CH_3 & & & \\ & | & & | & & | & & & \\ — O — & Si & - O - & Si & - O - & Si & — O — & & \\ & | & & | & & | & & & \\ & CH_3 & & CH_3 & & CH_3 & & & \end{array}$$

from which all others are derived by replacing some of the methyl groups. Silicones are common sealants, e.g. as RTV (room temperature vulcanization) resins; they are also used as $O-rings$ (silicone rubber), mould release agents and for lubrication.

7.2 The Calliope gamma facility

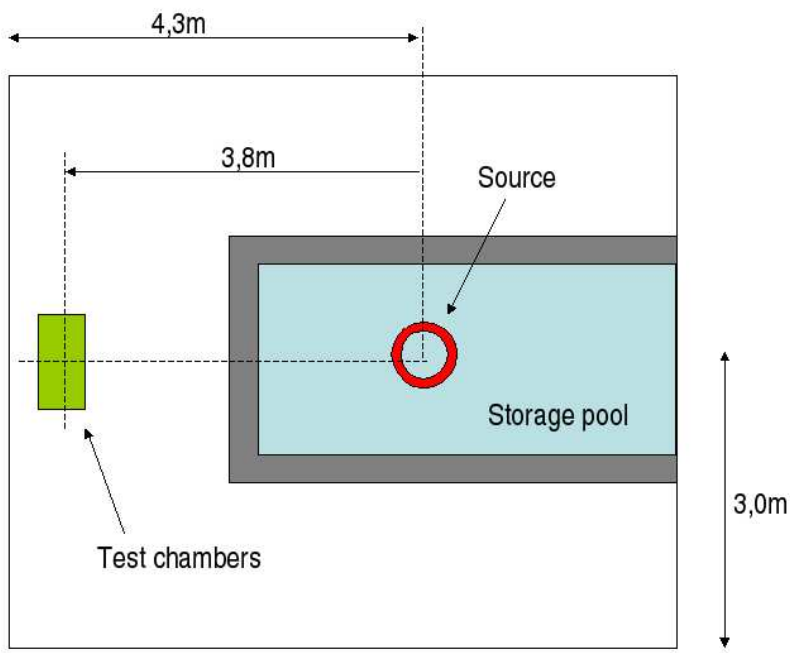

Figure 7.2: Schematic drawing of the Calliope facility.

The Calliope gamma facility at the ENEA Research Center near Rome [43] consists of a high intensity ^{60}Co source in a large volume shielded cell. The ^{60}Co isotope undergoes the beta decay $^{60}_{27}Co \rightarrow ^{60}_{27} Ni^* + e^- + \bar{\nu}_e$ with a half life $t_{1/2}$ of 5.24 years. The subsequent Nichel de-excitation produces two photons of 1.17 MeV and 1.32 MeV. These values fall in the middle of the photon energy spectrum 3.21. The beta electron is emitted with an energy up to 317 keV and travels less then 1 m in air.

The activity of the source is reported to be R'_γ =6.72×10^{14}(±5%) Bq at 1/1/2005. Hence, at the time of the test, about six months later, the activity used to be

$$R_\gamma = R'_\gamma \cdot e^{-\frac{\Delta T}{\tau}} = 6.3 \times 10^{14}\, Bq. \tag{7.1}$$

with $\Delta T \sim 0.5\, y$ and $\tau = t_{1/2}/ln2$ is the nuclide average lifetime. The detectors

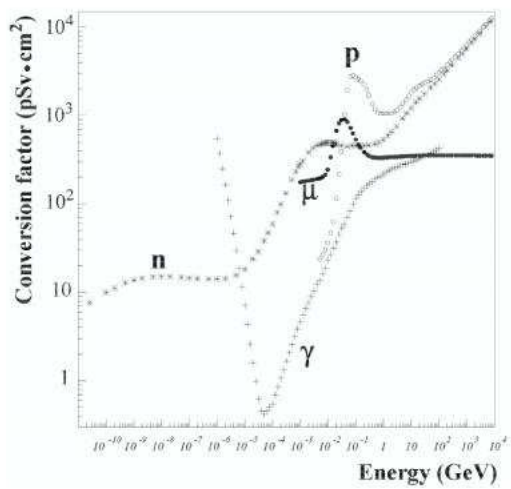

Figure 7.3: Conversion between energy and dose for different particles species.

under irradiation were placed at about 3.8 m from the center of the source (fig. 7.2). The photon flux Φ_γ at the detector surface can be evaluated (neglecting photons attenuation in air) as

$$\Phi_\gamma = 2 \times \frac{R_\gamma}{4\pi d^2} = 7.0 \times 10^8\, photons/cm^2 s \tag{7.2}$$

with R_γ from the 7.1, and $d = 380\, cm$.

As a check, the average absorbed dose rate in air at the detector location was measured. The value obtained is 15.0 Gy/h (10% uncertainty). The relation between the absorbed dose rate and the photon flux can be deduced from the fig. 7.3: the average photon energy, 1.25 MeV, corresponds to about 6 $pSv\, cm^2$. Since for the photon case Sv and Gy are equivalent the relation can be translated as: 1 Gy/s corresponds to $1.66 \cdot 10^{11}\ \gamma/cm^2 s$. This implies that 15.0 Gy/h corresponds to $6.9 \cdot 10^8\ \gamma/cm^2 s$, in good agreement with the value estimated from the source activity.

7.3 Experimental setup

7.3.1 The test detectors

A set of 48 identical drift tubes, 470 mm long, were built and tested following the standard *ATLAS* wiring and quality control procedure [44]. The two 6×4 drift tubes chambers (bundles) were built gluing together six tubes (placed one next to the other with a separation of 0.02 mm) to form each layer and then gluing the different layers one in top of the other. The wire pitch is expected to be 30.035 mm and the uncertainty on the wire position with respect to the pitch to be than 20 μm. The bundles were equipped with the *ATLAS* on chamber gas distribution system components. The gas inlet and outlet to each bundle were provided by two aluminum manifolds connected to the tubes by stainless steel capillaries of different length. Each capillary supplies gas to three tubes in the same layer connected in series with plastic rings. The gas mixture $Ar : CO_2$ (93 : 7) was supplied from a bottle of certified premixed gas. The pressure and the flux of the gas mixture were regulated and measured using a pressure controller and a mass flow meter, respectively. The gas tightness of MDTs in the bundles was estimated by the pressure drop rate either before and after the irradiation period. The gas leak of both bundles was found well below the *ATLAS*w standard limits (2×10^{-8} bar·l/s per tube). The gas flow during the test period was 3.5 l/h per chamber, corresponding to about 10 complete volume exchanges per day.
It is useful to introduce here a tube numbering scheme that will be used in the following. The tubes are numbered from 1 to 24 counting from left to right from the read-out side starting from the first layer which is the lower one (that is, the tube in the lower left corner of the test chamber is tube 1 and the one in the upper right corner is tube 24).

7.3.2 Front-end and DAQ electronics

The MDT electronics is described in 3.3 and 4.1.1. Each test chamber, consists of 24 tubes, hence is read out by a single *mezzanine* board. The information from the ADC has been recorded and used in the following analysis as a diagnostics for monitoring the chamber gas gain. The sensitivity of the full analog signal chain (pre-amplifier to shaper) for the expected signal range amounts to 12 mV/fC. The integration gate has been set to 25 ns and the discrimination threshold corresponds to the collection of the first 20 primary electrons (pe). From previous studies on this front-end electronics emerges that the sensitivity of this ADC at the working point, in terms of electrons collected at the anode wire, is about $1\ ADC_{ch}/0.85\ pe = 1\ ADC_{ch}/2.7\ fC$. Note that each pe produces an avalanche with a multiplication factor G equal to $2 \cdot 10^4$ at the *ATLAS* working point.

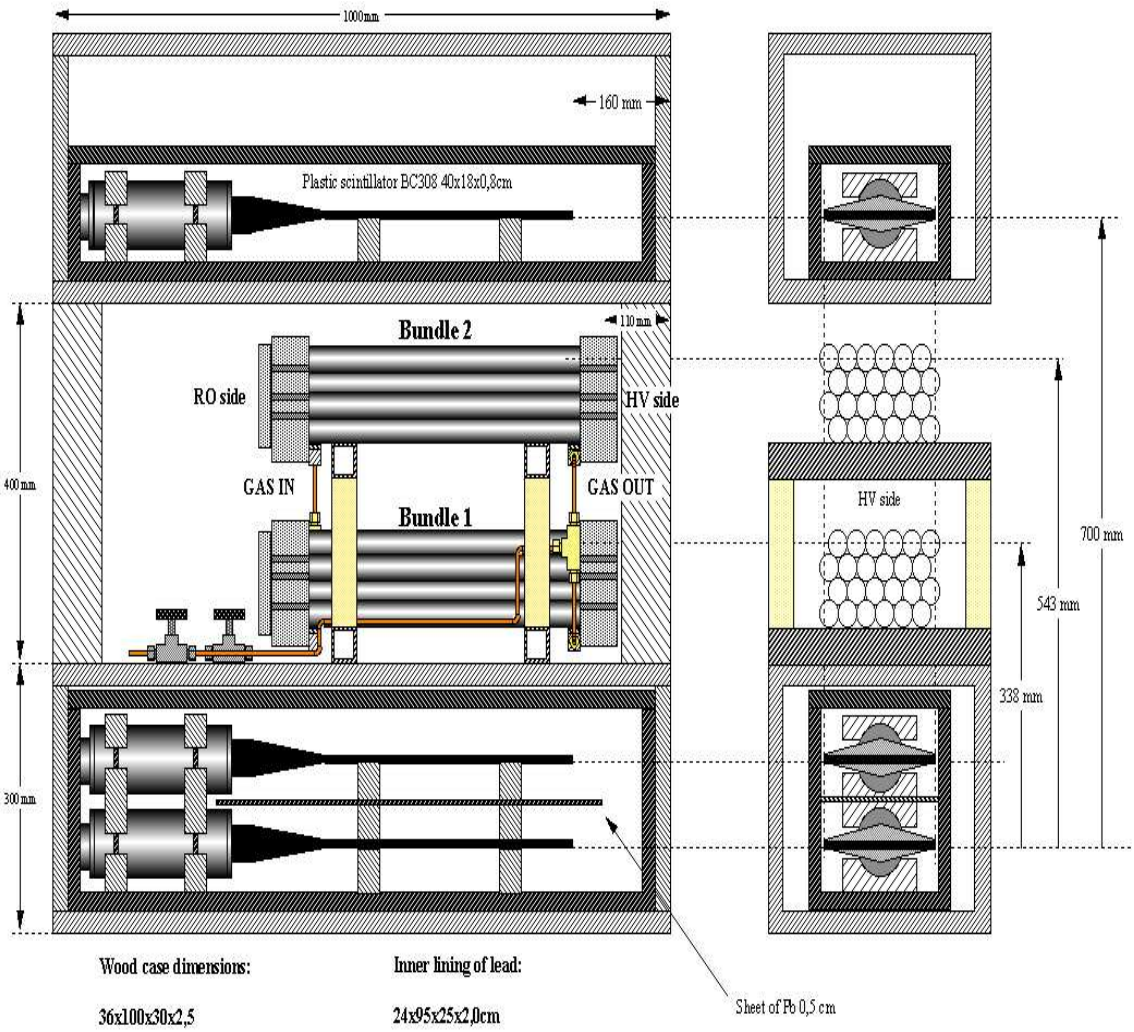

Figure 7.4: Side and front view of the setup showing the two bundles and the scintillator counters in the shielded boxes.

7.3.3 Trigger

A coincidence of three scintillator counters was used as a trigger for cosmic rays. The counters were placed into two boxes (two in the box below the test chambers and the other in the one above) and completely wrapped with a 2 cm thick layer of lead in order to prevent PMT damage during the irradiation. Fig. 7.3.1 shows the set up.

7.4 Choice of the working point

Since the aim of the test is to study MDT performance with increasing accumulated charge it's important to avoid gas gain drop related to space charge effects. This would reduced significantly the accumulated charge in a given irradiation time (par. 3.4.2). In the following is described a calculation to optimize the working point to accumulate the maximum charge during the irradiation campaign.

The maximun ion drift time t_{max} was already derived in 3.2.4. In the approximation $r_0 << b$:

$$t_{max} = t(b) = \frac{ln(b/a)}{2\,\mu V} b^2. \tag{7.3}$$

In the above formula the electric field

$$E(r) = \frac{V}{ln\frac{b}{a}} \cdot \frac{1}{r} \tag{7.4}$$

of the "undisturbed" tube is used. For high rates, the field will change and the maximum ion drift time has to be corrected as well. For the ion mobility the value 1.7 cm^2/Vs (at the atmospheric pressure) is assumed (see par. 3.2.2, fig. 3.6). The mobility scales linearly with the pressure p: $\mu = \mu(p_0) \times p_0/p$.

Assuming a uniform tube irradiation, it can be demonstrated the ion density ρ has the following expression:

$$\rho(r) = \rho = n_p \cdot G \cdot t_{max} \cdot \frac{1}{\pi b^2} \cdot \frac{R}{L}. \tag{7.5}$$

where n_p is the number of primary ion pairs, G the gas gain and R/L is the counting rate per wire length (see par. 3.4.1). It results that the ion density is independet of the radial distance r from the wire. The two photons emitted by the Calliope source mostly produce Compton electrons in the Al tube wall. The energy of these electrons ranges from zero to 883 keV (where there is a peak) and the average value is 550 keV. The average number of ion-electrons pairs produced by these Compton electrons into the gas volume can be estimated from the equation 3.45 at the atmospheric pressure ($\sim 1\ bar$), the result is $n_p \sim 300$.

In the general case of a non zero charge density, the potential $\Phi(r)$ can be calculated with the Poisson's equation

$$\Delta\Phi(r) = -\frac{\rho e}{\varepsilon_0} \tag{7.6}$$

and the boundary conditions $\Phi(a) = V$, $\Phi(b) = 0$. The solution over the active lenght L is:

$$\Phi(r) = \frac{V ln\frac{b}{r}}{ln\frac{b}{a}} + \frac{\rho e}{4\varepsilon_0} \cdot \left((b^2 - r^2) - \frac{(b^2 - a^2) ln\frac{b}{r}}{ln\frac{b}{a}} \right). \tag{7.7}$$

The electric field is then

$$E(r) = -\frac{d}{dr}\Phi(r) = \frac{V}{ln\frac{b}{a}} \cdot \frac{1}{r} + \frac{\rho e}{4\varepsilon_0}\left(2r - \frac{b^2 - r^2}{ln\frac{b}{a}}\frac{1}{r}\right). \tag{7.8}$$

As expected, in the absence of a space charge ($\rho = 0$) the second term vanishes and the equation 7.8 reduces to the first term that is the 7.4.

For gas gain estimation it is sufficient to use the field in the amplification region, this implies $r << b$ (par. 3.2.3) and

$$E(r) \simeq \frac{V - \delta V}{ln\frac{b}{a}} \cdot \frac{1}{r} \tag{7.9}$$

defining

$$\delta V = n_p \cdot G \cdot t_{max}\frac{e}{4\pi\varepsilon_0}\frac{R}{L}. \tag{7.10}$$

The electric field in the avalanche region behaves as if the effective potential was $V - \delta V$. It is important to notice that the t_{max} in the 7.10 is not given by the 7.3 which is valid for $\rho = 0$. Using the general expression 7.8 for the electric field in the Ramo's formula 3.31 the general expression for the maximum ion drift time is:

$$t_{max} = \frac{\varepsilon_0}{\mu\rho e} ln\left(1 + \frac{\rho e b^2 ln\frac{b}{a}}{2\varepsilon_0(V - \delta V)}\right). \tag{7.11}$$

The gas gain G can be estimated by the Diethorn formula 3.30 which depends on the potential V and can be written as follows:

$$G = exp\left(\frac{V ln2}{\Delta V ln\frac{b}{a}} \cdot ln\frac{V}{E_{min}\frac{\rho}{\rho_0}\, a\, ln\frac{b}{a}}\right). \tag{7.12}$$

The meaning of the parameters ΔV and E_{min} is explained in 3.2.3. The values used are the measurements reported there.

The orignal purpose was to calculate the actual gain at a given rate R/L. This cannot be simply achieved by replacing $V - \delta V$ to V in the 7.12 because δV itself depends on the gain. Hence the two equations 7.12 and 7.10 have been solved iteratively.

The sensitivity ε_γ to photons of about 1 MeV is nedeed: the value used here is 0.0087 (cfr. fig. 3.22(a)). The counting rate per wire length is then

$$\frac{R}{L} = \Phi_\gamma \times L \times \varepsilon_\gamma \sim 2 \times 10^7 \frac{Hz}{cm} \tag{7.13}$$

where L is the tube diameter (3 cm).

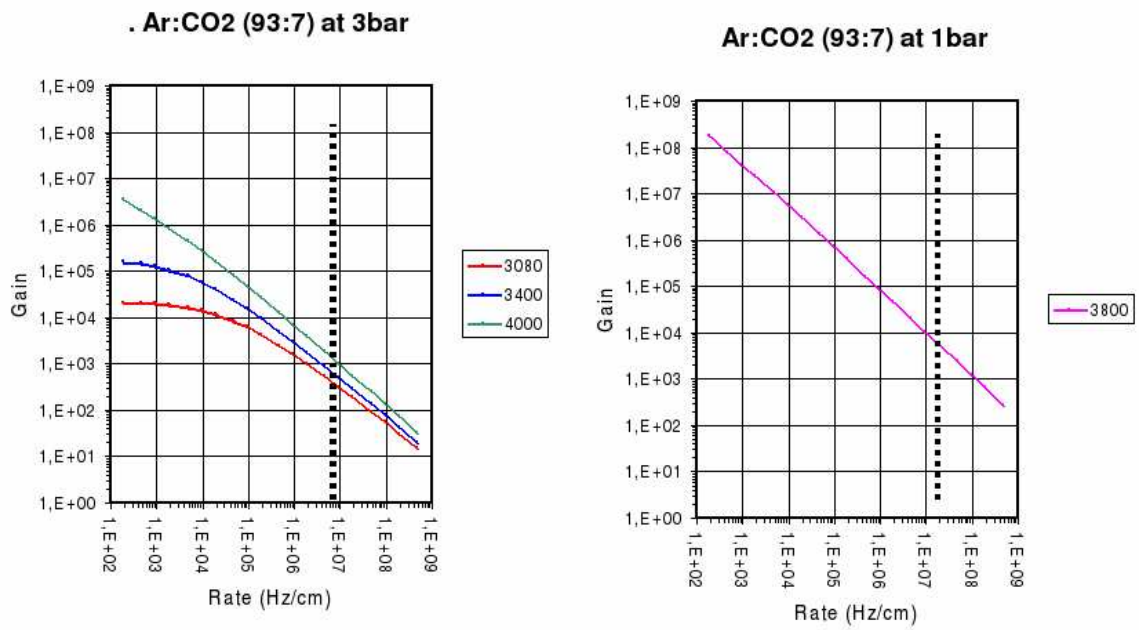

Figure 7.5: Gas gain with respect to the photon background rate. In the left plot the middle curve corresponds to 3400 V and the lower one to 3080 V. The vertical dotted line indicates the count rate at Calliope: $2 \times 10^7 Hz/cm$

The behaviour of the gas gain with increasing rate has been computed for the stantard gas at three different settings of the anode-cathode voltage: 3080 V, 3400 V and 4000 V. The results are shown in fig. 7.5. The gain is below the nominal value of 2×10^4 even at a voltage as high as 4000 V. To increase the gain is necessary to reduce the pressure as reported in the plot on the right where the pressure is 1.1 *bar* and the voltage 3800V.

The current induced on the wire can be estimated

$$I = \frac{R}{L} n_p \cdot G \cdot e \cdot L. \tag{7.14}$$

The current dependence on the tube settings and count rate is shown in fig. 7.6.

Rate (Hz/cm)	V(kV)	P (bar)	I (μA)	$I_{EXP}(\mu A)$
2.0 $\times 10^7$	3.8	1.1	220	180
2.0 $\times 10^7$	4.0	3.0	59	50
3.8 $\times 10^6$	4.0	3.0	49	41
3.8 $\times 10^6$	3.08	3.0	14	15

Table 7.1: Comparison between the measured current and the calculated value.

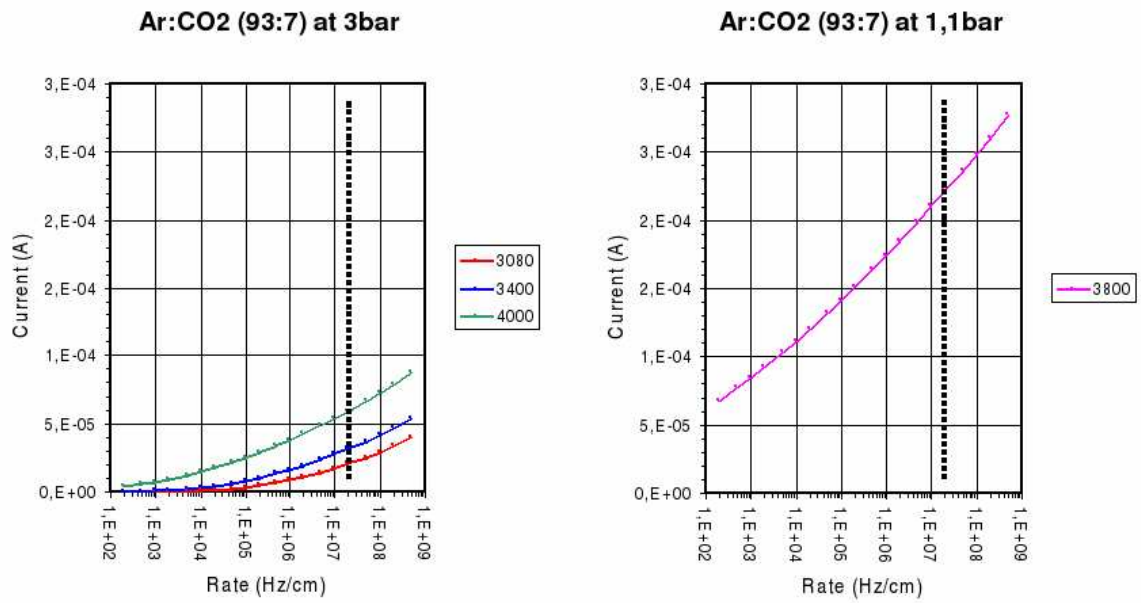

Figure 7.6: Iduced current with respect to the count rate for different tube operation settings. In the left plot the curve in the middle corresponds to 3400 V and the lower one to 3080 V. The vertical dotted line indicates the count rate at Calliope: 2×10^7 Hz/cm.

The current drawn by the chamber during the irradiation has been measured at different values of pressure and applied voltage and the photon flux[1]. From the values reported in tab. 7.1 the agreement between data and predicted values is rather good (10% level).

Operating the chamber at 3800 V and 1 bar gas pressure it is possible to operate in avalanche mode ($G \sim 0.5 \times 10^4$) even at a counting rate of the order of $10^7 Hz/cm$. With this configuration the current drawn is of about 200 μA which makes possible to accumulate the target value of 5 C/cm or so during the scheduled irradiation campaign (see next section).

7.5 Data samples

After assembly, the bundles have been tested with cosmic rays in the Roma Tre laboratory 4.1 The two test chambers were then moved to the Calliope plant to perform the aging test. Another test, consisting in two runs, was performed in the Roma Tre laboratory after the irradiation period. In the last run, the read-

[1]For a short period some radioactive elements have been removed from the source and the dose rate measured again.

run number		total events	accumulated charge	note
*Roma*3 sample	61	704×10^3	0 C/cm	
	168	401×10^3	4.8 C/cm	
	182	401×10^3	4.8 C/cm	changed read-out electronics
Calliope sample	68+69	78×10^3	0 C/cm	
	71	43×10^3	0.8 C/cm	
	74	43×10^3	1.3 C/cm	
	78	49×10^3	3.2 C/cm	
	79	300×10^3	4.8 C/cm	

Table 7.2: List of the runs used in the analysis.

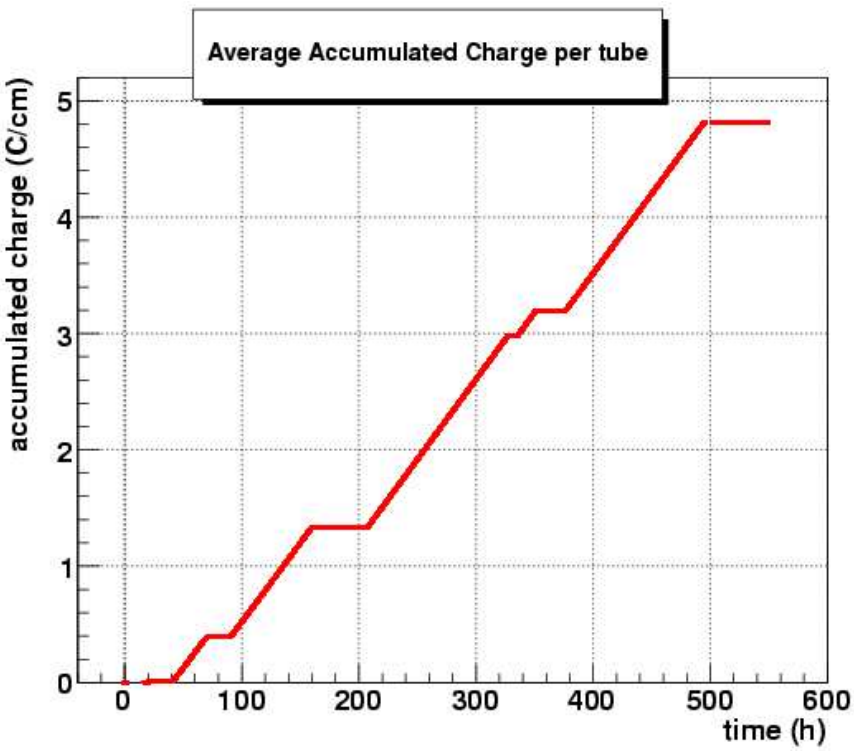

Figure 7.7: Accumulated charge during the irradiation campaign.

out electronics was changed. Before starting the irradiation campaign, a run with cosmic rays trigger was taken and used as reference. While the ^{60}Co source was switched on, the chambers were operated at 3800 V, 1.1 *bar* according to the considerations reported in the previous section. By rising the voltage and lowering the pressure, the current drawn by each tube could reach 180 μA resulting in an accumulated charge of 4.8 $C/cm/wire$ at the end of the whole irradiation period.

Periods of gamma irradiation were followed by data taking with the cosmic rays trigger (the source was turned off) with MDTs operated in the ATLAS standard conditions for performance monitoring. Five different runs are available for the analysis corresponding to an average accumulated charge per tube of 0.0, 0.8, 1.3, 3.2, 4.8 C/cm. From now on these data and the data acquired in the Roma Tre laboratory will be named *Calliope* and *Roma*3 samples respectively. Details of cosmic rays trigger runs are summarized in Table 7.2.

The increase of the accumulated charge is shown in fig. 7.7.

The periods in which the source was turned off for cosmic data taking are clearly visible.

7.6 Slow control

7.6.1 Environmental parameters

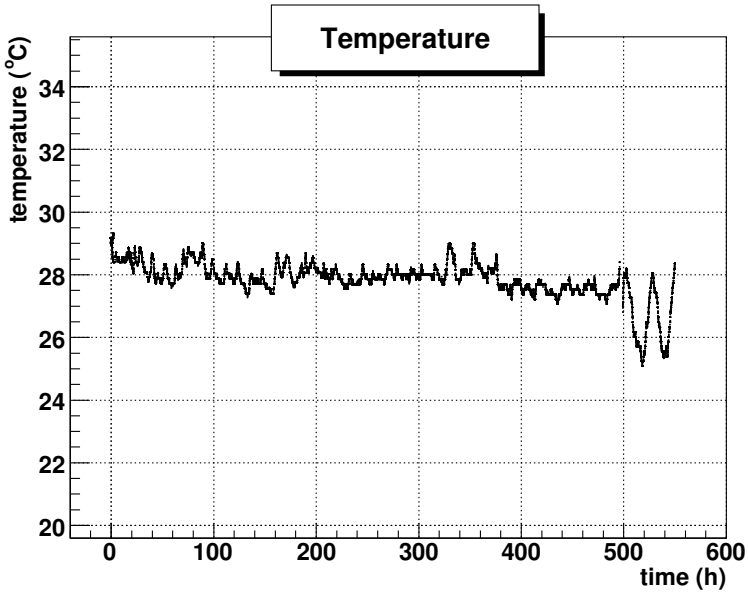

Figure 7.8: Temperature measured during the whole period.

During the test, gas temperature (T), flow and absolute pressure (P) were continuously recorded. The absolute values of T and P are known within ± 0.2 K and ± 3 $mbar$ respectively. Data were corrected offline for both temperature and atmospheric pressure variations [62]. The temperature during the whole period is shown in fig. 7.8.

Temperature instability in the last part is due to the fact that for the last cosmic run the setup was moved from the irradiation cell, in which the temperature was almost constant, to another room.

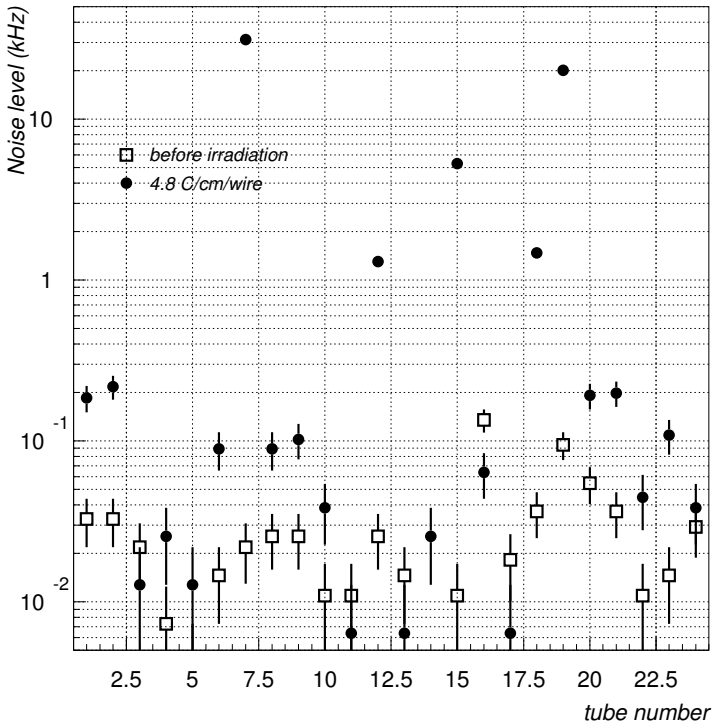

Figure 7.9: Noise level for the tubes of the first test chamber in the two runs of the *Roma*3 sample.

7.7 Drift parameters

In this section the analysis of single tube behavior is presented focusing on noise level, rise time distribution of the drift time spectra and collected charge. These quantities can give an insight on the status of the detector during irradiation and reveal aging effects (the rise time and the ADC spectra are the quantities which are the most sensitive to gain variation). The data analysis is based on the `CALIB` (Cap. 4.3) software package.

7.7.1 Drift time analysis

The noise level for all the tubes of the first test chamber is shown in fig. 7.9 for the two runs in the *Roma*3 sample. As can be seen the noise level is higher after

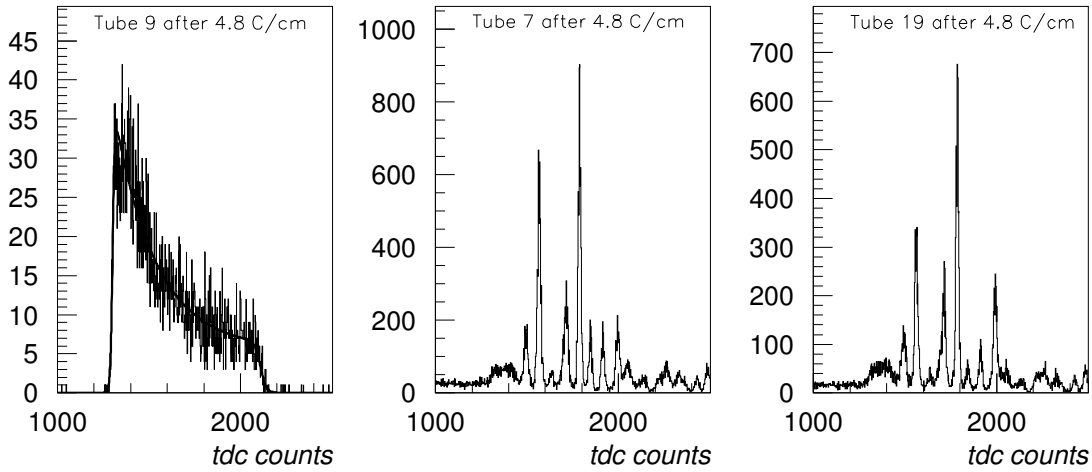

Figure 7.10: Drift time distribution for tubes 7 (center) and 19 (right) and for a good one (left) shown here for comparison.

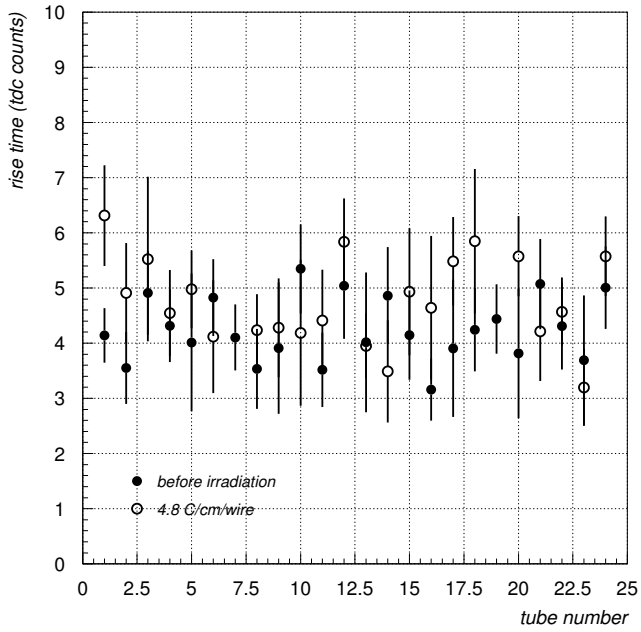

Figure 7.11: Rise time for the tubes of the first test chamber in the two runs of the *Roma3* sample.

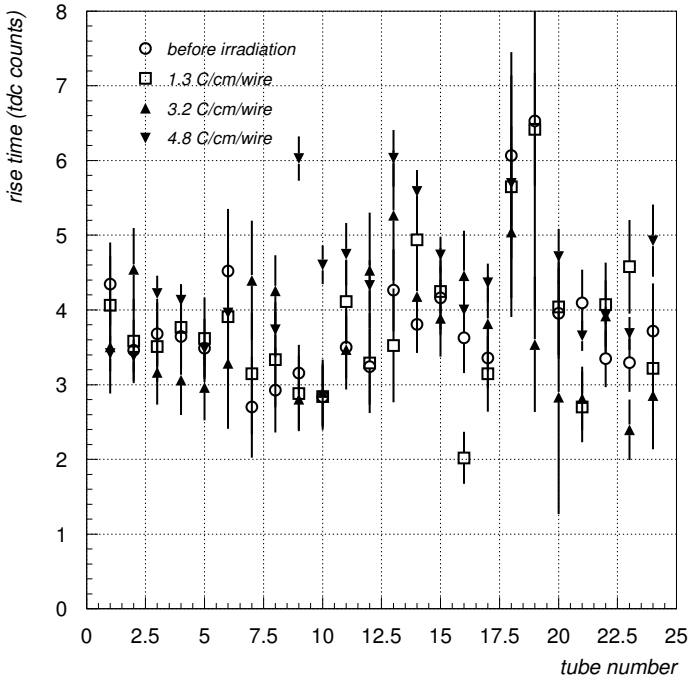

Figure 7.12: Rise time for the tubes of the first test chamber in the runs of the *Calliope* sample.

irradiation for all drift tubes.

As it has been experienced several times in the past, this difference can be easily explained with minor differences in the electronics connection and grounding as the setup has been mounted several times. For two tubes in particular (namely tubes 7 and 19), the noise level showed a major increase.

The drift time distribution for these tubes is shown in fig. 7.10 (center and right respectively) together with a good drift time distribution for another MDT shown for comparison (left part of fig. 7.10). As can be seen these tubes have a drift time distribution completely different and also a distorted charge distribution as will be shown in next section.

Another parameter of the drift time distribution that can give insight on tube aging is the rise time which is closely related to the space resolution. The rise time for all the tubes of the first test chamber is shown in fig. 7.11 for the two runs in the *Roma*3 sample. Tubes 7 and 19 are not included for the run after the irradiation period as a fit to their drift time distributions is meaningless. No clear effect of signal degradation can be found for the other tubes.

The same study on the rise rime stability has been performed on the same test chamber for the different runs in the *Calliope* sample and is shown in fig. 7.12.

The rise time shows to be constant as the accumulated charge increases.

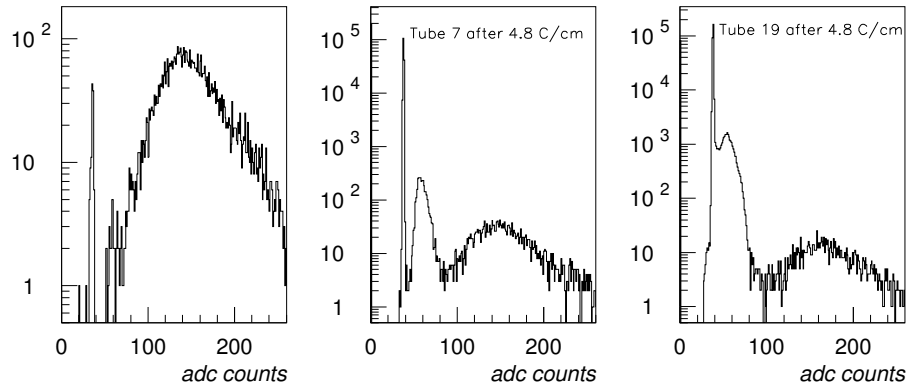

Figure 7.13: Collected charge distribution for tubes 7 (center) and 19 (right) and for a good one (left) shown here for comparison.

7.7.2 Collected charge analysis

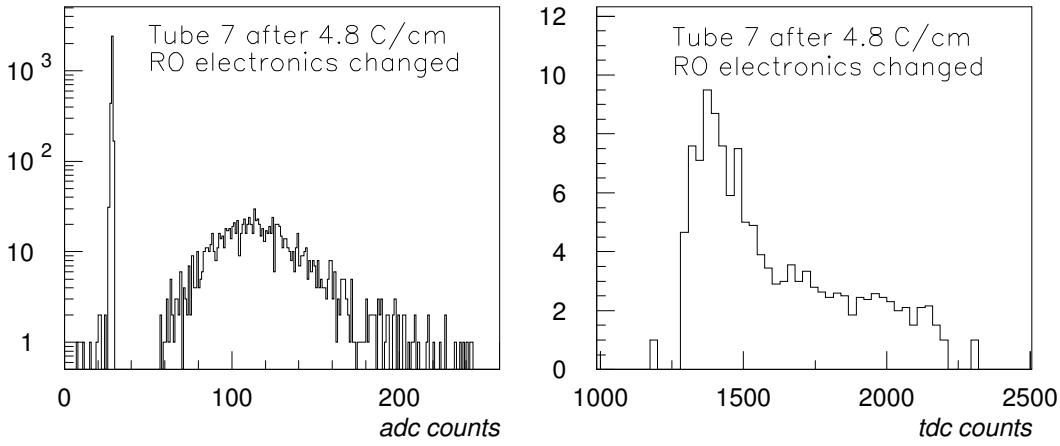

Figure 7.14: Collected charge distribution (left) and drift time spectra after applying the cuts on the ADC values (right) for tube 7 after changing the read-out electronics.

The measure of the collected charge (raw charge, par. 4.3) can be very useful to investigate variation in the tube gain and in the overall tube's response signal. The distribution of the collected charge is shown in Fig. 7.13 for a typical tube (left) and for the two tubes already highlighted in the previous section (center and right).

As can be seen the distribution for those tubes is rather distorted. In the last run of the *Roma*3 sample the read-out electronics was changed; this resulted in an improvement of the ADC response for these two tubes as shown in Fig. 7.14 (left) only for tube 7 as an example. The noise induced peak pedestal is still rather high. The drift time distribution obtained requiring an ADC value larger than 50 ADC counts (in order to suppress the noise induced peak pedestal) has the expected shape as shown in Fig. 7.14 (right).

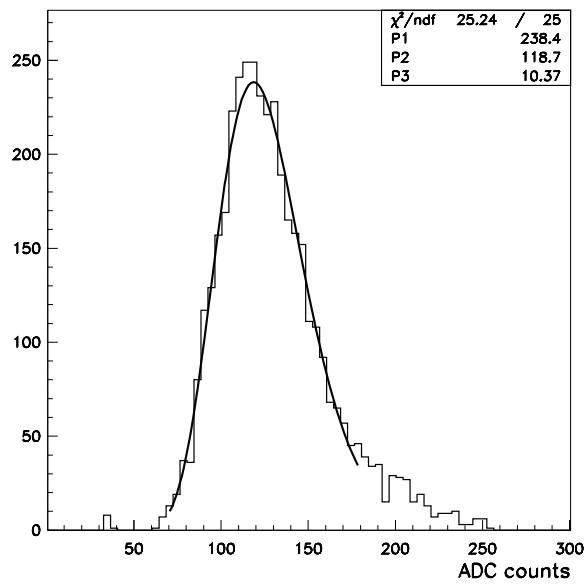

Figure 7.15: ADC spectrum fitted width the function 7.15.

For collected charge studies is necessary to fit the ADC distribution with a representative function where the mean value and width can be derived analytically. To fit the central region of the collected charge distribution, excluding the peak pedestal,

$$f(x) = p_1 e^{-\frac{(x-p_2)^2}{x p_3}}, \tag{7.15}$$

has been constructed which is a gaussian width a non-constant sigma, useful for quasi-symmetric distribution. The parameter p_2 is the value corresponding to the maximum of the distribution and the width can be described by the $FWHM$ given by

$$((p_3 ln2)^2 + 4p_2p_3 ln2)^{1/2}.$$

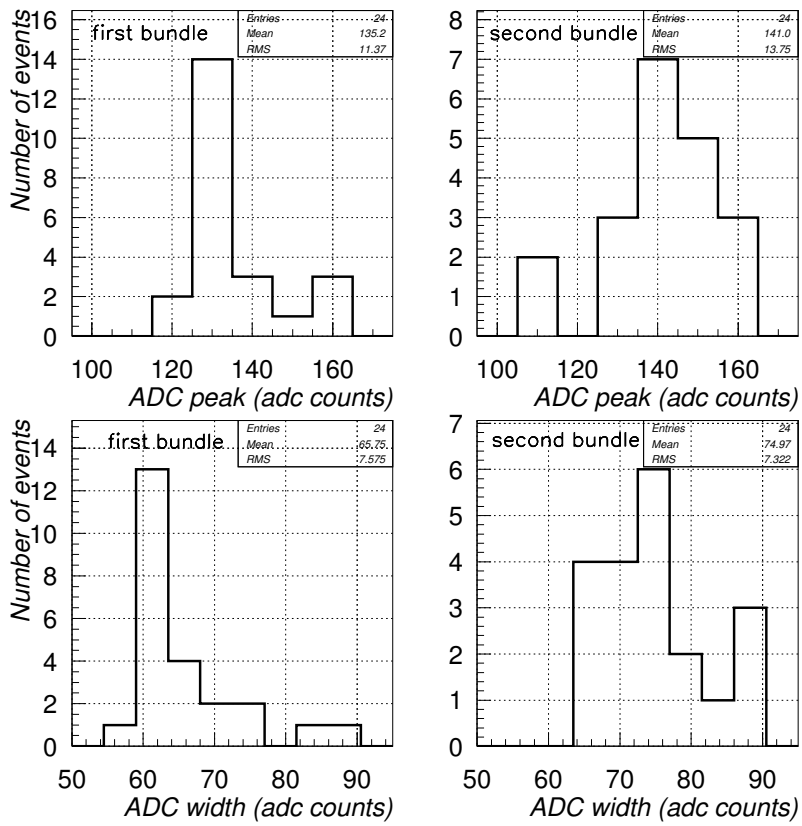

Figure 7.16: Distribution of the fit value of the ADC distribution peak value x_{max} and width $FWHM$ for the two test chambers before irradiation.

The gas gain is very sesitive to density variation, that is to say temperature and pressure, as the Diethorn formula states. From the 3.30, in the approximation $\Delta T << T$ and $\Delta P << P$:

$$G(T + \Delta T) = G(T) \cdot (1 + \Delta T/T)^{\alpha} \approx G(T)(1 + \alpha\ \Delta T/T) \tag{7.16}$$

$$G(P + \Delta P) = G(P) \cdot (1 + \Delta P/P)^{\alpha} \approx G(P)(1 - \alpha\ \Delta P/P) \tag{7.17}$$

where T is the absolute temperature expressed in Kelvin and $\alpha \approx 9.857$ for $Ar : CO_2$(93:7) at 3 bar. It was thus decided to correct the peak value x_{max} to take into account temperature and pressure variations in each run with temperature $T{=}T_0 + \Delta T$ and pressure $P{=}P_0 + \Delta P$, with respect to the reference temperature and pressure of the first run T_0 and P_0.

The corrected $x_{max}^{T_0,P_0}$ value has been obtained applying in turn a temperature and a pressure correction:

$$x_{max}^{T_0,P} = x_{max}^{T,P}\left(1 - 9.86\frac{\Delta T}{T_0}\right), \tag{7.18}$$

$$x_{max}^{T_0,P_0} = x_{max}^{T_0,P}\left(1 + 9.86\frac{\Delta P}{P_0}\right). \tag{7.19}$$

The distribution of the corrected value of x_{max} and $FWHM$ for all the tubes of the two bundles for the first run at the Calliope plant are shown as an example in Fig. 7.16. These values have a spread of about 10% as already reported in (Chap. 6).

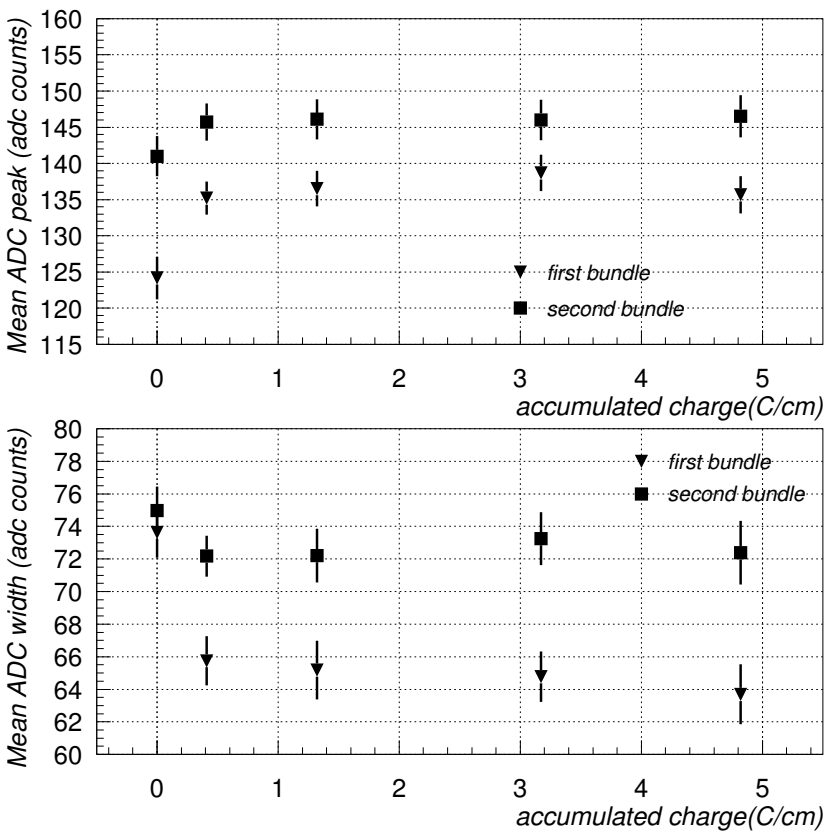

Figure 7.17: ADC distribution mean peak value x_{max} and mean width $FWHM$ (averaged on all the tubes of one test chamber) with respect to the accumulated charge for the two test chambers.

The mean value of the distributions in fig. 7.16 and of the analogous distributions for all the other runs are shown with respect to the accumulated charge in fig.

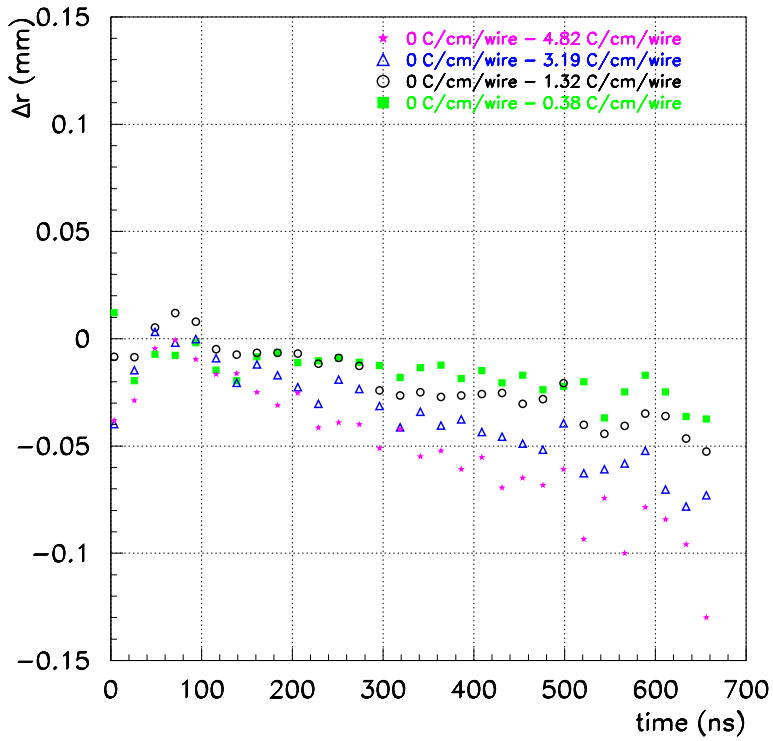

Figure 7.18: Comparison between the $r(t)s$ for the different runs with respect to reference data.

7.17. It can be seen that both values are almost constant.

7.8 Tracking analysis

7.8.1 Space-time relation

The dependence of $r(t)$ relations on accumulated charge has been investigated to understand MDTs tracking properties after intensive gamma irradiation. The *Calliope* data sample has been used to evaluate possible differences in the $r(t)$s as the accumulated charge is increasing. A $r(t)$ relation has been calculated for each single run. Because of their dependence on gas, temperature and composition, only data with temperature spread within 1.5 °C and pressure variation within few mbar have been analyzed. All $r(t)$s have been normalized to the same temperature of 28 °C, applying appropriate corrections as described in [47] and [53] and then compared with reference data taken before irradiation. Fig 7.18 shows the differences between the $r(t)$ computed for the reference run and the $r(t)$ computed for each other run.

A small increase of the difference between the $r(t)$s with increasing accumulated charge is visible. It is less than 100 μm for large radii even after the total accumulated charge of 4.8 C/cm/wire. Such a variation is corrected in the standard calibration of the $r(t)$ relations (calibrations have to be performed regularly to take into account environmental parameters variations that can give effect of the same size).

7.8.2 Tube efficiency

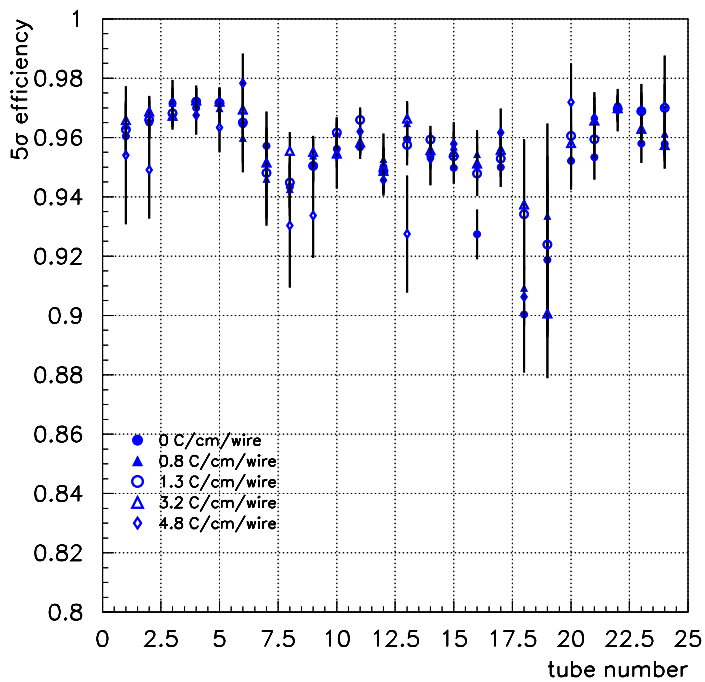

Figure 7.19: Efficiency for all the tubes of the first test chamber for the five cosmic runs.

Two definitions of efficiency can be given for drift tubes: *hit efficiency* is the probability to register a hit for a muon track crossing the tube, irrespective of the measured drift time, and *n-σ efficiency* is the probability that the drift radius r_{drift}, as reconstructed from the drift time, does not differ from r more than n times the single tube resolution. Both efficiencies have been computed with the `CALIB` package (Ch. 4);
Tracks with at least three hits on tubes different from the one under observation are selected; then a drift radius r_{drift} is extrapolated on that tube. If residual with respect to the track differs less than 5σ the hit is considered a "good hit": efficiency is then computed as the ratio between the number of good hits and

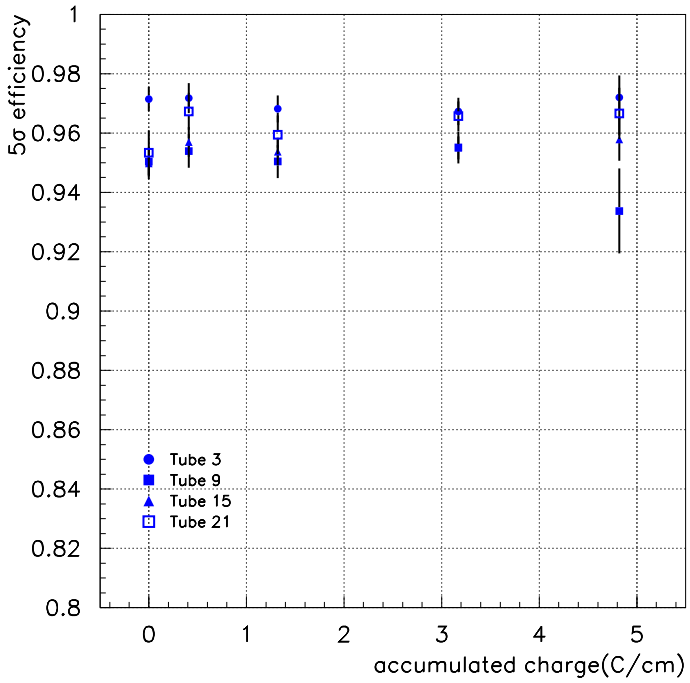

Figure 7.20: Efficiency for four central tubes (one for each layer) of the first test chamber versus accumulated charge.

the number of tracks that crossed the tube. An optimal calculation of the *n-σ efficiency* cannot be achieved with the present setup. The non perfect grounding caused a slightly high noise level in some tubes. This is a problem for the *n-σ efficiency* because of the 600 ns dead time fixed in the read-out electronics. Furthermore, for some angular configurations, the determination of the track parameters with only three drift circles suffers from an ambiguity that can affect the track extrapolation to the last tube. The best way to compute efficiency in the MDT chamber is to use the whole chamber, i.e. two multilayers, but this was not possible because the two bundles were not aligned. These effects are taken into account by normalizing the efficiency to the *hit efficiency*. The value of the efficiency for all the tubes of the first test chamber is shown in Fig. 7.19 for the five different cosmic runs. In the last run, after the last irradiation period, tubes 7 and 19 showed the behavior described in the previous sections and their *hit efficiency* suddenly drops to less than 0.5 and their efficiency is not shown in the figure.

As it is shown in Fig. 7.20 for some tubes of layer 3 as an example for all the other tubes, efficiency proved to be constant with respect to the accumulated charge.

The efficiency for tubes 7 and 19 has been controlled in the run of the *Roma*3 sample, in particular in the two runs after the irradiation campaign. After changing the read-out electronics the *hit efficiency* rises back to the initial value of 0.98±0.01 for tube 7 and to 0.95±0.02 for tube 19. This observation, in addition to the one in section 7.7.2 and to the wire analysis in the next section, suggests that a part of the read-out electronics suffered a damage during irradiation.

7.9 Wire analysis

After the two irradiation campaigns some anode wires of the two test chambers were removed in order to perform chemical and sufrace analysis. The aim of the wire examination was to reveal some pollution and to analyze their composition. Two techinques heve been used:
Scanning Electron Microscopy (SEM): Scanning Electron Microscopy or SEM makes it possible to resolve sub-micrometer details on the wire surface. This is done by moving a thin electron beam in a controlled way over the material under study and recording the number of electrons reflected. From the contrast of the SEM picture it is also possible to deduce whether a material is electrically conducting or not.
Energy Dispersive X-ray analysis (EDX): Energy Dispersive X-ray (EDX) analysis is a method usually combined with SEM. When hit by the scanning electron beam, atoms are left in an excited state with energy E_i; they return to their ground state E0 or a lower intermediate state E_j by emitting X-rays with a frequency proportional to the energy difference $E_i - E_j = E_{ij}$. Since the values of E_{ij} are characteristic for each chemical element, the chemical composition of a material can be identified by recording the X-ray spectrum; this is usually done with the help of a semi-conductor detector. EDX is sensitive to all elements except hydrogen; the volume of material probed is usually of the order $1\mu m^3$. With the instrument used for this thesis a volume of $0.5 \times 0.5 \times 0.5\,\mu m^3$ was analysed; material on the surface of another substance could be detected if its thickness exceeded $0.2\,\mu m$.

Four analyzed wires were taken from tubes of the test chamber n. 1, which was also irradiated with neutrons (7.11), one from each layer. In particular, the wires from MDT tubes n. 3, 9, 13 and 20 were extracted. The first two tubes accumulated a charge of 4.82 C/cm (5261 Gy), while tubes 13 and 20 accumulated a charge of 3.19 C/cm (3471 Gy) and 1.32 C/cm (1419 Gy) respectively. The other three wires were extracted from MDT tubes n. 3, 10 and 19 (the one that showed the worst response) from the test chamber n. 2. From previous aging tests ([54], [55] and [56]) it is known that pure $Ar - CO_2$ (93%:7%) doesn't show

any evidence of aging up to an accumulated charge of 1.2 C/cm. Nevertheless some aging effects can appear if the gas is polluted with sealing material used for valves or chemicals that enters the drift tube by outgasing of components that are in contact with the gas system (e.g. cleaning agent). Since the on-chamber gas distribution is serial-parallel (three tube series) the wires were chosen in order to have at least one tube for each position in the gas series. The wires were extracted from the tubes and analyzed. A detailed description of the employed technique to extract the anode wire is given in [56].
Each extracted wire was divided in three samples of 4 cm length each: one at 2 cm from the beginning of the wire (gas inlet side), one in the middle and one at 2 cm from the end of the wire (gas outlet side). Each sample was analyzed and no deposits on the wire surface has been observed. Three additional samples (reference wires) of 4 cm length each, taken directly from the same wire spool employed for the test chamber tubes, were analyzed for comparison.

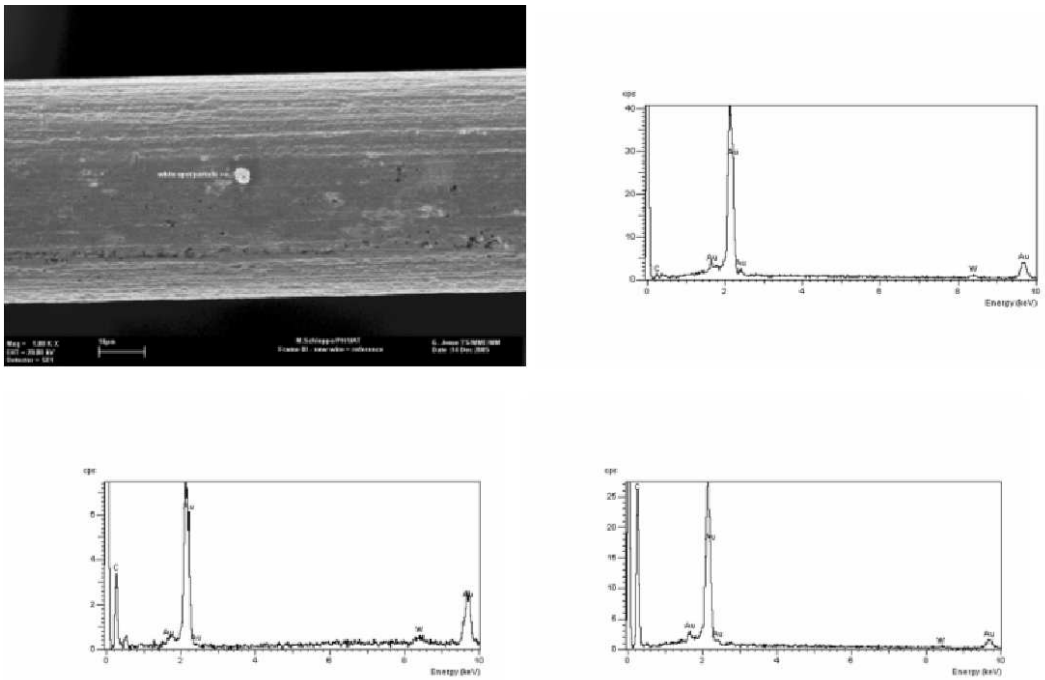

Figure 7.21: Micro-photo of the reference wire. EDX analysis related to the clean surface of the wire (top right), black spot (bottom left) and white particle (bottom right).

Fig. 7.21 shows a micro-photo and the analysis of one reference wire. The surface is everywhere clean besides some black spots and white particles, both with an important amount of Carbon. The surface of the irradiated wires appears similar to the reference one: mostly clean, with some regions with black stains (C-O-Si-Al-Ca) and other regions with white particles (Al-Cl-F). Fig. 7.22 shows two

micro-photos as examples of irradiated wires with black stains (left) and white particles (right).

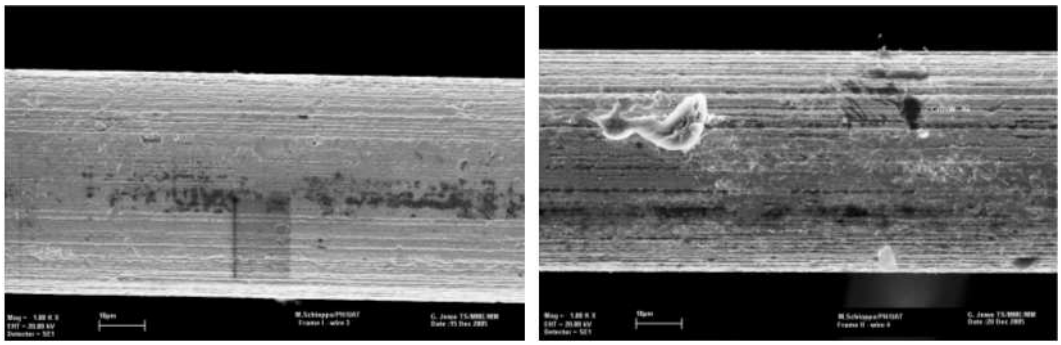

Figure 7.22: Micro-photo of the irradiated wire 20 (left) and wire 3 (right).

In conclusion the whole set of analyzed wires show the same pollution detected on the reference one.

7.10 Summary

A intensive photon irradiation test was performed on final MDT-like test chambers. After a full accumulated charge of 4.8 C/cm per tube, a good behavior of the chamber is observed.
The pressure drop rate before and after the irradiation campaign was measured and it turned out to be constant (1×10^{-8}bar·l/s, a value that fits with the ATLAS requirements). This implies a stable behavior of o-rings, end-plugs and all the different gas distribution elements.
Two tubes showed a distorted drift time spectra and a sudden drop in efficiency after 4.8 C/cm was accumulated. The hit efficiency improved by changing the read-out electronics, suggesting a damage to some electronic component. The SEM/EDX analysis shows no evidence of damages on the wires. It has to be underlined here that the ASD and the TDC chip have been tested under irradiation [57],[58] and proved to tolerate an irradiation equivalent to 10 years of LHC operation. However, in this test the irradiation was much higher than in earlier studies.
No significant gain drop is observed looking at the measured charge deposit and negligible variations of the drift properties result from drift time spectra and space-time relation studies for all the tubes of two bundles.
The single tube efficiency remains constant with increasing accumulated charge.
No evidences of deposits or damages on the surfaces of the wires resulted from chemical analysis.

7.11 Neutron irradiation test

Another test was performed by exposing a drift chamber to the neutron flux originated form a nuclear reactor. Neverthelss the detector sensitivity to neutrons is one oder of magnitude lower compared to photons, the neutron background can also affect critically the device performance and stability being the main source of radiation damage of the detector components i.e. bulk damage of the electronics.

7.11.1 Tapiro nuclear facility

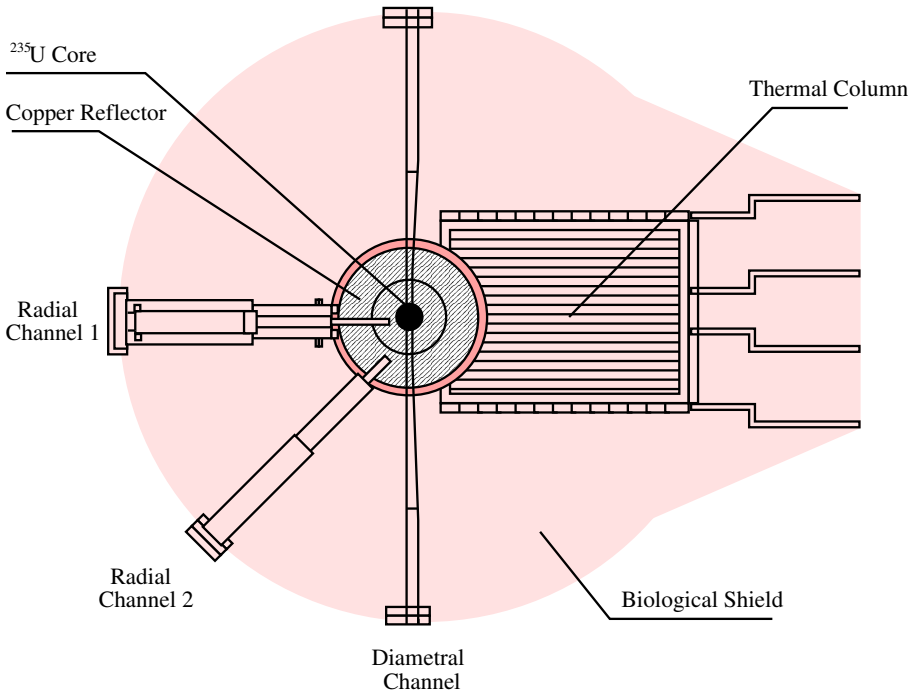

Figure 7.23: Schematic layout of TAPIRO reactor with a view of the experimental channels and of the thermal column cave.

The Tapiro nuclear reactor is a high-enriched ^{258}Uranium copper reflected fast neutron source at the ENEA research center. The reactor core has a cylindrical core with radius of 6.2 cm and a height of 10.87 cm. the fuel is a metal alloy (U 98.5%, Mo 1.5%) with a fully enriched ^{235}Uranium (93.5%). Its critical mass is 21.46 kg. The maximum neutron flux at the core center is 2.2×10^{12} neutrons/$cm^2 s$ at the nominal thermal power of 5 kW. The reactor is surrounded by borate concrete shievlding about 170 cm thick.

Several channels of different dimension and depth which penetrate the reactor shielding are present. They are used for locating apparatus to be irradiated (fig.

7.23). The largest cave available, the thermal column cave (fig. 7.23) the one used for the test, has dimensions: $110 \times 110 \times 160\, cm^3$.

The neutron energy spectrum in the thermal cave is shown in fig. 7.24 It is

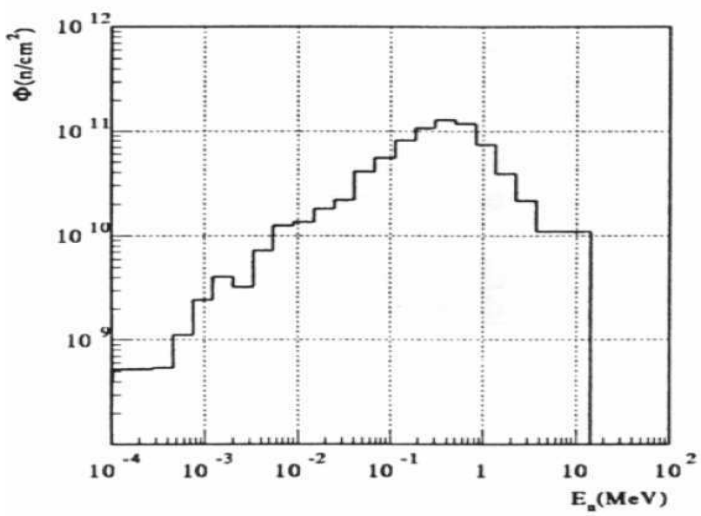

Figure 7.24: Neutron energy spectrum at the nuclear reactor source.

rhather consistent with the one expected in ATLAS i.e. fig. 3.22.

The neutron flux at the detector surface have been measured by means of an activation tecnique, utilising bare and cadmium-shielded gold foils. The values measured at the reactor thermal power of 200 W are: $2.23 \times 10^7\ Hz/cm^2$ at the surface which is upstream with respect to the source and $1.07 \times 10^7\ Hz/cm^2$ at the opposite side of the detector (uncertainties are at 10% level).

7.11.2 Trigger system and setup

The experimental setup is the same assembled for the test at the photon facility 7.2. One chamber only has been used because of the small volume of the experimental cavity. The bundle used had already being irradiated with photons without significant performance degradation. The trigger scintillators have been further shielded with Borum powder to suppress the neutron background.

The chamber has been irradiated for about 6-8 hours integrating from 1.68×10^{11} n$/cm^2 s$ to 1.48×10^{12} n$/cm^2 s$ by varying the reactor power between 100 W to 400 W. During the irradiation the trigger was switched off. Currents drawn by the tubes varies from 5 μA to 8 μA. To monitor the chamber response four cosmic ray data sample have been taken, during the campaign, while the reactor was off. A run was taken before starting the test to be used as reference.

7.11.3 Analysis

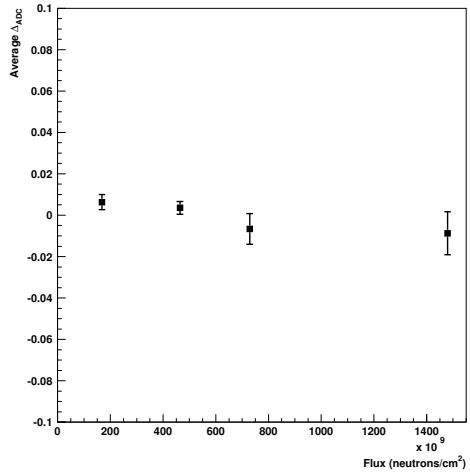

Figure 7.25: ADC peak mean relative variation with respect to the reference run for different neutrons integrated flux.

Three major tools were used to investigate the MDT response: *ADC* spectra, $r(t)$ relation and efficiency (see previous sections). In fig. 7.25 the mean relative variation of the *ADC* with respect to the neutron integrated flux. Deviation from the reference value are whitin 2 %. The $r(t)$ relation was computed for each of

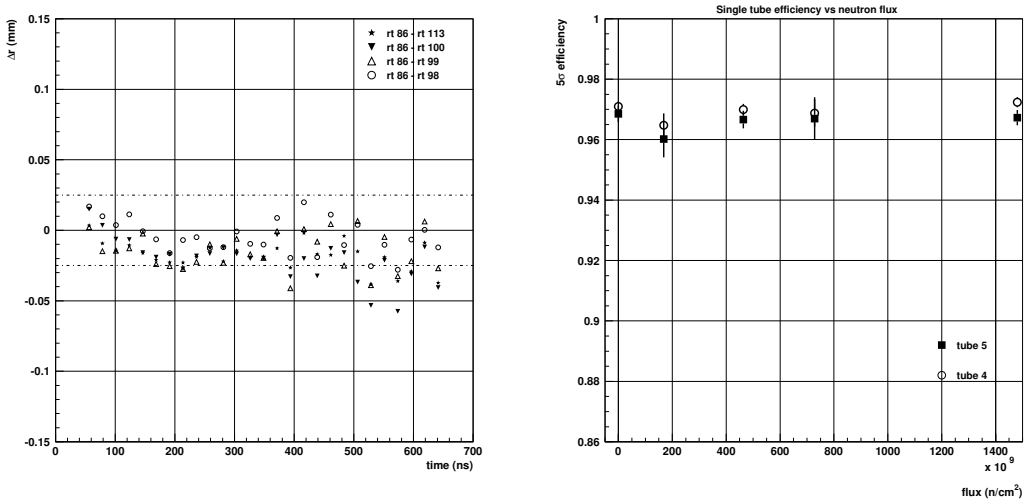

Figure 7.26: *Left* R(t) differences with respect to the reference for different runs. *Right*. Five sigma efficiency for the various runs (for two tubes only).

the four mentioned runs and compared to the $r(t)$ obtained from the reference run 7.26: differences are whithin $\pm 25\,\mu m$. Results from efficiency measurements are reported in fig. 7.26: differences seems not to be significant.

The results of the wire analysis are described in 7.9.

The Muon Spectrometer of the ATLAS detector, which is currently under construction at the CERN laboratory, relies on Monitored Drift Tubes (MDTs) for precise muon track reconstruction. In this thesis are reported results achieved on the study of the MDT response and calibration.

An accurate knowledge of the MDT calibration constants and a longterm response uniformity and stability are mandatory to fully exploit the high mechanical precision of the detector and the good spatial resolution of the drift tubes.

Measurements were carried out using different experimental setups, developing and assembling ad-hoc detector and/or trigger devices in some cases. Some analysis alghoritms, to be used for calibration optimization and improvement and which can be implemented in the official software packages, have been developed and tested with both simulated and experimental data.

A dedicated algorithm for the simulation of the detector response has been also implemented for alghoritm validation and interpretation of some experimental results.

A study of the systematic errors in the calibration procedure has been carried out analysing test beam data samples. In particular, the variuos sources of uncertainties and the most critical factors affecting the determination of the MDT calibration constants (the t_0 and the space-to-time $r(t)$ relation) have been put in evidence. It results, for expample, that the $r(t)$ relation is more sensitive to the sample size and angular spread of the tracks and less to the $t0$ determination. A set of parameters tuned to speed up the calibration procedures is also provided. A modified version of the standard procedure, which can also be used for the measurement of the position of the track in the wire direction in regions of the spectrometer where the information on the secoond coordinate is missing is presented as well. A section is dedicated to the description of the resolution determination algorithm and the possible optimizations quantifying the effects of the multiple scattering and of the trigger signal delays.

A degradation of the wire chamber performance after extended operation in a high-rate environment is the main factor limiting the detector lifetime. Two scaled-down MDT chambers have been build and equipped with the standard gas distribution system, high voltage distribution and front-end electronics to study their response under photon irradiation accumulating a total charge of 4.8 C/cm/wire corresponding to about 10 years of LHC operation at the highest luminosity. A neutron irradiation test was also performed. No significant drop in gain was observed neither significant variations variations in the drift properties. The visual and spectroscopic analysis of the anode wires confirmed these results.

Bibliography

[1] F.Halzen,A.D.Martin, *Quarks and leptons: an introductory course in modern particle physics*, Wiley (1984).

[2] L.B.Okun; *Leptoni e quark*, Mir (1986).

[3] F.Mandl, G.Shaw, *Quantum Field Theory*, Wiley (1984).

[4] LEP Collaboration, LEP Electroweak Working Group and SLD Heavy Flavor and Electroweak Groups, *A combination of preliminary electroweak measurements and constraints on the standard model.*, hep-ex/0112021 , (2001).

[5] The LEP working group for Higgs boson searches, *Search for the Standard Model Higgs Boson at LEP*, CERN-EP/2001-055 (July 11, 2001)

[6] S.P.Martin, *A Supersymmetry primer*, CERN/90-10 ECFA/90-133, (1999).

[7] D.Denegri, *Aachen LHC workshop*, hep-ph/9709356 , (1990).

[8] Z.Kunszt, S.Moretti e W.J.Stirling, *Higgs production at LHC*, Z.Phys. C74, (1997) 479.

[9] A.Djouadi, D.Graudenz, M.Spira e P.M.Zerwas, *Higgs boson production at the LHC*, Nucl.Phys. B453, (1995)17.

[10] ATLAS Collaboration; *ATLAS detector and physics performance Technical Design Report*, CERN-LHCC-99-14/15 (1999).

[11] B.Mellado; *Prospects of the Higgs physics at the LHC*, ATLAS internal note, ATL-CONF-2002-004 (2002).

[12] The LHC Study Group; *The LHC conceptual design report*, The Yellow Book, CERN/AC/95-05 (LHC).

[13] ATLAS Collaboration; *ATLAS Technical Proposal for a General Purpose p-p Experiment at the Large Hadron Collider at CERN*, CERN/LHCC/94-43,LHCC/P2 (1994).

[14] ATLAS collaboration; *Inner Detector Technical Design Report*, Volume 1, CERN/LHCC/97-16 (1997).

[15] ATLAS collaboration; *Liquid Argon Calorimeter, Technical Design Report*, CERN/LHCC/96-41 (1996).

[16] ATLAS collaboration; *Tile Calorimeter Technical Design Report*, CERN/LHCC/96-42 (1996).

[17] ATLAS Collaboration; *ATLAS detector and physics performance Technical Design Report*, CERN-LHCC-99-14/15 (1999).

[18] ATLAS Muon Collaboration, *ATLAS Muon Spectrometer Tecnical Design Report*, CERN/LHCC/97-22, ATLAS TDR-10 (1997).

[19] W.R. Leo, *Techniques for Nuclear and Particle Physics Experiments*, Spinger-Verlag, New York (1994).

[20] J.E. Moyal, *Theory of ionization fluctuations*, Phil. Mag. 46 (1955)

[21] F.Sauli, *Principles of operations of multiwire proportional and drift chambers*, CERN 77-09, May 1977.

[22] W.Blum, L.Rolandi, *Particle Detection with Drift Chambers*, Springer-Verlag (1993).

[23] L.G.Huxley and R.W.Crompton, *The Diffusion and Drift of Electrons in Gases*, Wiley, New York (1974).

[24] K. Kleinknecht, *Detectors for particle radiation*, Cambridge Univ. Press 1998.

[25] M. Aleksa, W. Riegler, *Non-linear MDT drift Gases like* Ar/CO_2, Atlas internal note, ATL-MUON-98-268.

[26] G. D. Alkhazov, *Statistics of elctron avalanches and ultimate resolution of proportional counters*, NIM 89, 155 (1970).

[27] C.Posch, E.Hazen, J.Oliver, *MDT-ASD, CMOS front-end for ATLAS MDT*, ATLAS Internal Note, ATL-MUON-2002-003

[28] Y.Arai, *AMT-1 and 2 (ATLAS Muon TDC version 1 and 2) User's manual*, *http://atlas.kek.jp/ arai*

[29] P.Branchini, F.Petrucci, *A platform-independent software for MDT front-end read-out with the CSM0*, ATLAS Internal Note, ATL-MUON-2002-001

[30] S. Baranov *et. al.*, *Estimation of Radiation Background, Impact on Detectors, Activation and Shielding Optimization in ATLAS*, ATL-GEN-2005-001.

[31] P.Branchini, F.Ceradini, M.Iodice, D.Orestano, F.Petrucci, E.Spiriti; *The cosmic ray hodoscope for the MDT chamber test site in Roma Tre*, ATLAS Internal Note, ATL-MUON-2001-007

[32] C.Bacci et al.;
Design of a cosmic test site for QAQC of MDT chambers, ATLAS Internal Note, ATL-MUON-98-241

[33] B.Ball, J.Chapman, J.Gregory, J Mann, J.Hollar;
CSM Users Manual, *http://atlas.physics.lsa.umich.edu/docushare*

[34] E.Hazen;
ATLAS CSM 18-channel Adapter, *http://bmc.bu.edu/bmc/CSM_adapter*

[35] P.Bagnaia, A.Baroncelli, M.Iodice, D.Orestano, L.Pontecorvo;
Calib: a package for MDT calibration studies - User Manual, ATLAS Internal Note, ATL-COM-MUON-2002-004.

[36] Saclay Muon Group;
Atlas Muon DataBase, *http://atlas.web.cern.ch/Atlas/GROUPS/MUON /AMDB_SIMREC/amdb_simrec.html*.

[37] R.Veenhof, *GARFIELD - Simulation of gazeous detectors*, Cern Program Library W5050.

[38] Igor Smirnov, *HEED, program to compute energy loss of particles in gases*, Version 1.01, CERN Program Library.

[39] S. Biagi, *MAGBOLTZ, program to compute gas transport parameters*, Version 1.10, CERN Program Library.

[40] J.A.Kadyk, Wire chamber aging, Nucl. Instr. and Meth. A 300 (1991) 436-479

[41] J.Va'vra, Review of wire chamber aging, Nucl. Instr. and Meth. A 252 (1986) 547-563

[42] Proceedings of the Workshop on Radiation Damage to Wire Chambers, LBL-21170, (1986);
Proceedings of the International workshop on Aging Phenomena in Gaseous Detectors, Nucl. Instr. and Methods A515, (2003);
M.Titov et al, hep-ex/0204005, IEEE Trans.Nucl.Sci. NS49(4),1609 (2002);
J. Va'vra, Nucl. Instr. and Methods A515, 1 (2003).

[43] S.Baccaro et al., Gamma and neutron irradiation facility at ENEA-Casaccia Center, Report CERN-CMS/TN, 95-192 (RADH) 1995.
A.Tata et al., Radiation technology facilities operating at the Italian ENEA-Casaccia research center, ENEA RT/INN/98/1, CERN libraries, Geneva SCAN-9809001.

[44] A.Aprile et al., Production and test of monitored drift tubes for the muon spectrometer of the ATLAS experiment, IEEE Transactions on Nuclear Science, 49-3 (2002) 1077.
C.Bini et al., Nucl. Instr. and Meth. in Phys. Res. A461 (2001) 65.
P.Bagnaia et al., Nucl. Instr. and Meth. in Phys. Res. A546 (2005) 481

[45] J.E.Huth, J.Oliver, E.S.Hazen, C.Posch, J.T.Shank, Development of an octal CMOS ASD for the ATLAS Muon detector, Proceedings of the 5th Conference on Electronics for LHC Experiments, Snowmass, CO, 20-24 September 1999, p.436;

C.Posch, E.Hazen, and J.Oliver, MDT-ASD: CMOS front-end for ATLAS MDT chambers, ATL-MUON-2002-003; 7.6.2001, http://weblib.cern.ch/Home/ATLAS_Collection/ATLAS_Notes/Muon/

[46] Y.Arai, Nucl. Instr. and Meth. in Phys. Res. A453 (2000) 365; Y.Arai, Y.Kurumisawa and T.Emura, Development and a SEU Test of a TDC LSI for the ATLAS Muon Detector, Proceedings of the 7th Workshop on Electronics for LHC Experiments, Stockholm, Sweden, 10-14 September 2001, p.185.

[47] A.Baroncelli et al., Nucl. Instr. and Meth. in Phys. Res. A557 (2006) 421-435

[48] G.Scherberger et al, High rate performance of drift tubes, Nucl. Instr. and Meth. in Phys. Research A 424 (1999) 495-511.

[49] P.Bagnaia et al., CALIB: a Package for MDT Calibration Studies, ATL-COM-MUON-2002-004, 28.1.2002, http://weblib.cern.ch/Home/ATLAS_Collection/ATLAS_Notes/Muon/

[50] G.Avolio et al., Nucl. Instr. and Meth. in Phys. Res. A523 (2004) 309

[51] W. Blum, L.Rolandi, Particle Detection with Drift Chambers, Springer, Berlin, 1994.

[52] P.Branchini et al., Study of the drift properties of high pressure drift tubes for the ATLAS muon spectrometer, IEEE NS Symposium Conference Record, 1 (2004) 427

[53] A.Aleksa, W.Riegler, Non-linear MDT drift gases like Ar-CO_2, ATL-MUON-98-268, 14.12.1998, http://weblib.cern.ch/Home/ATLAS_Collection/ATLAS_Notes/Muon/.

[54] S. Kirche et al., Parameter of MDT Ageing and Reanimation, ATL-MUON-2001-012, http://weblib.cern.ch/Home/ATLAS_Collection/ATLAS_Notes/Muon/.

[55] S.Zimmerman et al., MDT ageing studies - Results of the studies conducted at the Gamma Irradiation Facility GIF between autumn 2001 and summer 2003, ATL-MUON-2004-019, http://weblib.cern.ch/Home/ATLAS_Collection/ATLAS_Notes/Muon/.

[56] C. Adorisio et al., Results from the 2004 ATLAS MDT ageing test in X5/GIF (Gamma Irradiation Facility) area, ATL-COM-MUON-2005-016, http://weblib.cern.ch/Home/ATLAS_Collection/ATLAS_Notes/Muon/.

[57] C.Posch, E.Hazen, Total ionizing dose radiation hardness of the ATLAS MDT ASD and the HP-Agilent 0.5 micron CMOS process, ATL-ELEC-2002-001, http://weblib.cern.ch/Home/ATLAS_Collection/ATLAS_Notes/Muon/.

[58] Y.Arai, M.Fukuda, T.Emura, Performance and irradiation tests of the 0.3 μm CMOS TDC for the ATLAS MDT, CERN-OPEN-2000-102, `http://weblib.cern.ch/Home/ATLAS_Collection/ATLAS_Notes/Muon/`.

[59] M. Deile, J. Dubbert, M. Faessler, C. Gruhn, N.P. Hessey, A. Staude, *Test Beam Studies of the Gas Mixtures for Drift Tubes*, ATLAS Internal Note, MUON-NO-122, 1996.

[60] M. Kollefrath *et al*, *Aging Studies for the Atlas Monitored Drift Tubes*, Nucl. Instr. and Meth. A 419 (1998), 351-356.

[61] G. Avolio, S Di Luise. *et al*, *Monitored Drift Tubes aging under intensive gamma irradiation*, Nucl. Instr. and Meth. A 568 264 (2006).

[62] A. Baroncelli em et al, *Study of temperature and gas composition effects in rt relations of ATLAS MDT BIL Chambers*, ATASl Internal Note ATL-COM-MUON-2004-0011.